CHALMERS

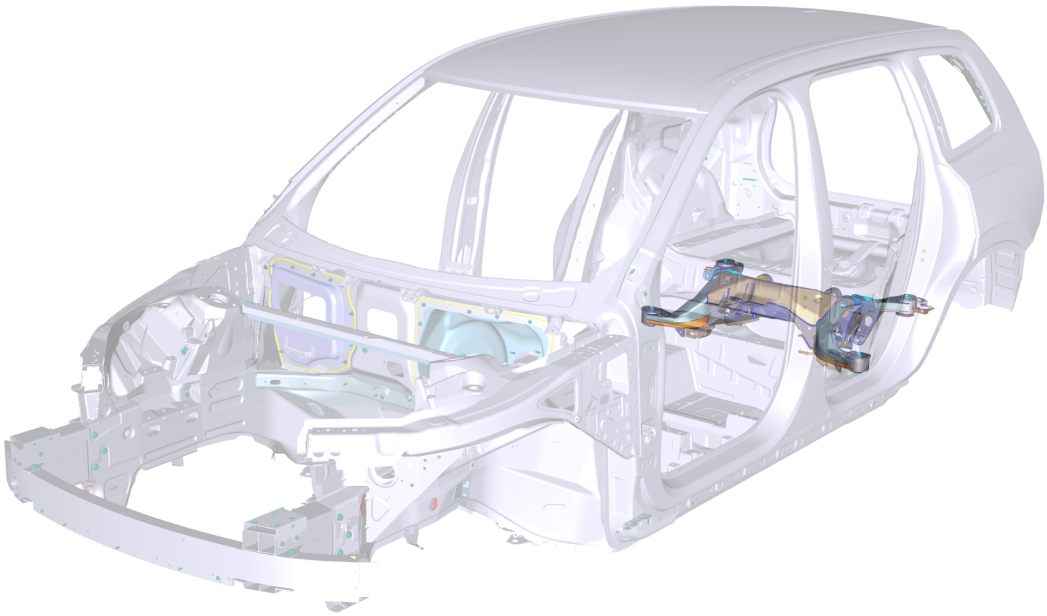

Variability of nominally identical components and their influence in an assembly

Application to a Volvo XC90

Master's thesis in Applied Mechanics

GESA DORENDORF

Department of Applied Mechanics
CHALMERS UNIVERSITY OF TECHNOLOGY
Göteborg, Sweden 2017

MASTER'S THESIS IN APPLIED MECHANICS

Variability of nominally identical components and their influence in an assembly

Application to a Volvo XC90

GESA DORENDORF

Department of Applied Mechanics
Division of Dynamics
CHALMERS UNIVERSITY OF TECHNOLOGY

Göteborg, Sweden 2017

Variability of nominally identical components and their influence in an assembly
Application to a Volvo XC90
GESA DORENDORF

Master's thesis 2017:20
ISSN 1652-8557
Department of Applied Mechanics
Division of Dynamics
Chalmers University of Technology
SE-412 96 Göteborg
Sweden
Telephone: +46 (0)31-772 1000

Cover:
Assembly of a Volvo XC90 (2015) body in white and rear subframe.

Chalmers Reproservice
Göteborg, Sweden 2017

Variability of nominally identical components and their influence in an assembly
Application to a Volvo XC90
Master's thesis in Applied Mechanics
GESA DORENDORF
Department of Applied Mechanics
Division of Dynamics
Chalmers University of Technology

Abstract

Mechanical engineering is important in many engineering industries, for instance the automotive industry. It allows the developement of improved and more complex products. The automotive industry possesses one of the biggest markets worldwide and is affected by a high level of competition. Thousands of nominally identical cars are manufactured everyday. Due to production tolerances, variable properties as well as other uncertainties, a spread of properties is observed for nominally identical products. To performe time and cost efficient analyses of engineering products, computer aided engineering (CAE) is increasingly used. The finite element (FE) method allows fast analyses and modifications of large, complex structures, prior to manufacturing the product. A central issue with FE simulations is the verification of the model, i.e. that the FE model predicts the real model behavior with proper accuracy. Thus, for the verification process, a data set apart from the FE model is required, which is usually obtained by an experimental modal analysis (EMA).

The EMA of nominally identical components can help to identify uncertainties and variations in these components. These uncertainties and variations can be used to improve the accuracy of corresponding FE models due to implementation of variations. Otherwise, they indicate also an issue for FE models because EMAs are not performed for all components and thus the upper and lower boundaries of the uncertainties and variations are not completely known. This thesis comprises studies in this field of interest, i.e. the quantification of the variability influence of nominally identical components in an assembly. Two rear subframes of a Volvo XC90 (2015) car are assembled to the same body in white (BIW) and analyzed experimentally as well as with CAE.

The FE models are validated for a defined frequency range. A sensor placement for the BIW is evaluated based on the method of effective independence. Furthermore, an experimental test setup is developed. An FE model updating with respect to a data set of vibration measurements is performed for one rear subframe. This includes the updating of stiffness and thickness parameters in the FE model by minimzing a frequency based deviation metric using equalized damping. During the calibration procedure, the bootstrapping method is used to estimate statistical informations, i.e. uncertainties of the calibration parameters. With the use of an additional calibrated rear subframe, the spread in properties for the nominally identical rear subframes is analyzed.

Furthermore, an assembly of the BIW and the two subframes is analyzed numerically as well as experimentally. The FE simulation uses a substructuring approach using the component mode synthesis method, i.e. the Craig-Bampton method. In the EMA, the subframes are mounted as suggested by the Volvo Car Corporation, and the dynamic responses of the two assemblies are analyzed with the main focus on the response measured on the BIW. Results of the FE analysis are compared with results of the EMA and thus differences between the two assemblies of a BIW and two nominally identical rear subframes analyzed.

The studies denote the rubber bushing stiffnesses in the interface of the subframes to the BIW as the parameters which cause the largest differences between the two assemblies. Other properties such as plate thicknesses and Young's moduli of steel parts are found to cause less differences. Further, differences are related to the fixed-interface modes of the individual subframes.

Keywords: Experimental modal analysis, model updating, structural dynamics, component mode synthesis, Craig-Bampton, uncertainty quantification, effects in assemblies, system identification, automotive industry

Preface

The work in this thesis was performed in 20 weeks, from January to June in 2017. It is a cooperation between Chalmers University of Technology and the Volvo Car Corporation (VCC) in Göteborg. Furthermore, the analyses carried out in this thesis are related to a PhD project dealing with uncertainties and variability in structural dynamics. In this thesis results obtained from said PhD project have been used in combination with new results obtained in this work.

Acknowledgements

I would first of all like to thank my supervisor Mladen Gibanica and examiner Thomas Abrahamsson, who have always time for discussions and support, come up with new ideas but also provided me with the possibility to try out and find my own ideas. They have always been encouraging and motivating, and enable me great possibilities.

Further, I would like to thank all the people in the VCC Noise and Vibration Center, who have always been willing to help and support me as well, especially with simulation tasks.

Lastly, I want to thank Jörg Schwieger, a friend of mine, who took the time to read my work and supplied me with a lot of tips and hints to improve this thesis.

Nomenclature

Abbrevations

A_{112}	Assembly of BIW and rear subframe 112
A_{220}	Assembly of BIW and rear subframe 220
AutoMAC	Model assurance criterion for two vectors
BIB	Body in blue
BIG	Body in grey
BIW	Body in white
CAE	Computer aided engineering
CB	Craig-Bampton
CMS	Component-mode-synthesis
COV	Coefficient of variation
DoF	Degree of freedom
DoF_c	Candidate set of DoFs
DoF_f	Final set of DoFs
EfI	Method of effective independence
EMA	Experimental model analysis
EoM	Equation of motion
EvP	Eigenvalue problem
FE	Finite element
FE_{265}	Calibrated FE model up to 265 Hz
FE_{nom}	Nominal FE model
FEA	Finite element analysis
FIM	Fisher information matrix
FRF	Frequency response function
LHS	Left hand side
MAC	Model assurance criterion
MDOF	Multiple degrees of freedom
NRMSE	Fit with respect to the normalized root mean square error
RHS	Right hand side
SUMAC	Substructure model assurance criterion
VCC	Volvo Car Corporation

Symbols

$\boldsymbol{\delta}$	Deviation metric
$\boldsymbol{\eta}$	Vector of generalized coordinates
$\boldsymbol{\Lambda}$	Diagonal matrix of eigenvalues
$\boldsymbol{\lambda}_i$	Eigenvalue i
$\boldsymbol{\omega}_i$	Eigenfrequency i

$\boldsymbol{\Phi}$	Eigenvector matrix
$\boldsymbol{\phi}_{\mathrm{i}}$	Eigenvector i
$\boldsymbol{\Psi}_{\mathrm{C}}$	Static condensation matrix
$\boldsymbol{A}$	State matrix
$\boldsymbol{B}$	Input matrix
$\boldsymbol{C}$	Output matrix
$\boldsymbol{D}$	Feedthrough matrix
$\boldsymbol{f}$	Force vector
$\boldsymbol{g}_{\mathrm{b}}$	Interface forces
$\boldsymbol{H}$	Frequency response function matrix
$\boldsymbol{K}$	Stiffness matrix
$\boldsymbol{L}$	Localization matrix
$\boldsymbol{M}$	Mass matrix
$\boldsymbol{P}$	Transformation matrix relating the output to the measurement type
$\boldsymbol{q}$	Displacement vector
$\boldsymbol{R}$	Transformation matrix in the CMS
$\boldsymbol{S}$	Coupling DoFs matrix
$\boldsymbol{T}$	Transformation matrix
$\boldsymbol{u}_{\mathrm{b}}$	Interface displacements
$\boldsymbol{u}$	Input vector
$\boldsymbol{V}$	Damping matrix
$\boldsymbol{Z}$	Impedance matrix
$\boldsymbol{z}$	State vector
$\mathscr{L}$	Laplace transform

Superscripts

(s)	Substructure s
FE	FE data
X	Experimental data

Subscripts

m	Modal domain
ml	Mass loaded

Contents

1 Introduction

This Chapter presents the background, purpose, limitations and outline of this thesis. The work is a cooperation between the Chalmers University of Technology and Volvo Car Corporation (VCC) Noise and Vibrations Center and part of a project to deal with uncertainties and their influence in structural components.

1.1 Background

Engineering industries, such as the automotive or the aerospace industry, manufacture thousands of nominally identical components everyday. Production tolerances, variable properties and other uncertainties causes differences between these nominally identical components. Computer aided engineering (CAE) is used with increasing importance to treat large and complex structures. The finite element (FE) method is one part of it and enables analyses prior to manufacturing the product. To analyze large and complex structures, FE models are often treated as substructures [KRV08]. This means that a large structure is divided into smaller domains where each domain is analyzed separately. Afterwards, dynamic properties of the small substructures are coupled to described the behavior of the complete structure. A well known method denotes the component-mode-synthesis (CMS) [KRV08].

A central problem in CAE is FE model validation. Large quantities of components are produced, which are nominally identical, but show differences in their dynamic properties in vibration tests. Hence, a calibration and validation of an FE model against only one set of properties does not guarantee the properties of a second component. Therfore, it is required to quantify possible variations between nominally identical components and take them into account in a validation procedure. Herein, the EMA is usually used to obtain reference data for FE model validation [Ewi00].

Beyond the quantification of uncertainties in nominally identical components, it is important to evaluate their effect in an assembly. Products, such as the Volvo XC90, are built up of hundreds of different components. Thus, it is of high interest to analyze the propagation of differences of a subcomponent in an assmbly with another component.

1.2 Purpose

The aim of this thesis is to analyze the influence of variations of nominally identical components in an assembly. This includes the identification of possible sources for uncertainties of nominally identical componets in a coupled configuration. Overall, frequencies are considered between 30 Hz and 300 Hz. Additionally, special focus is set on the frequencies of the global mode shapes of the BIW, i.e. 30 Hz to 65 Hz, and on frequencies between 30 Hz and 170 Hz in the assembled configuration.

The studies are performed on two nominally identical rear subframes of a Volvo XC90 (2015) in an assembly with a body in white (BIW), which is the main car body. Herein, the dynamic response of said components is analyzed in an individual as well as coupled setup. Two types of studies, i.e. EMAs and FEAs, are considered to fulfill the aim of the thesis.

The EMA includes the developement of a sensor placement on the BIW with respect to the method of effective independence (EfI) [Kam10]. Furthermore, mathematical models on first order form are established for the measured raw data with the N4SID method [MAL96]. The FEA contains a model calibration of one rear subframe with a frequency based deviation metric and damping equalization [AK15]. The CMS [KRV08] is used to couple the FE models of the BIW and rear subframes.

All used models, i.e. the FE models of the BIW and rear subframe as well as the test specimen for the vibration analysis, were provided by VCC. The test equipment, such as accelerometers, actuator and the measurement hardware are provided by Chalmers.

1.3 Limitations

The work in this thesis only considers studies on the provided models by VCC. A modification or calibration of FE models is only performed for one rear subframe. All other models as well as provided measurement data from [GA17] are assumed to be sufficient. An exception forms the BIW, where brackets that are significantly affected by local mode shapes are removed in both models, the FE model and the corresponding test specimen.

1.4 Outline

The theoretical background of the performed analyses in this thesis are presented in Chapter 2. First, the general equations and relations of a structural dynamic system are presented in Section 2.1. Section 2.2 to 2.5 explain the more specific relations reffering to the accomplished analyses. Section 2.2 described the required knowledge for the pretest planning of the performed experiments. Section 2.3 presents the theory of correlation analyses between experiments and simulations. Section 2.4 gives an overview about the physics of model updating and Section 2.5 the dynamic substructure synthesis.

Chapter 3 summarizes the methodology of the EMA and CAE simulation. It provides informations about the used software in Section 3.1 and the different types of models in Section 3.2 to 3.4. The details of the EMA are presented in Section 3.3. Furthermore, the calibration of the rear subframe is summarized in Section 3.5.

The results of the considered analyses are shown in Chapter 4. They are divided into three groups of results. First, the individual results of the BIW in Section 4.1, second the calibration results of the rear subframe in Section 4.2 and last, in Section 4.3, the results of the assembly of the BIW and rear subframe. The latter includes the results related to the main goal of this thesis.

Chapter 5 discusses the findings of Chapter 4. It starts in Section 5.1 with remarks about the models and test setup. In Section 5.2 aspects of the calibration are discussed. Section 5.3 discusses the differences of the assemblies.

Chapter 6 concludes the performed work and give proposals for future studies.

2 Theory

2.1 General definition of structural dynamic systems

The behavior of a multiple-degree-of-freedom (MDOF) system is defined by the equations of motion (EoMs). EoMs can occur in second order as well as in first order form. EoMs are often obtained by the use of Newton's second law or Lagrange's equations [CK06] and denote the mathematical model of a structural dynamic system.

2.1.1 Second order form

For an MDOF system, the EoMs are defined as [CK06]

$$\boldsymbol{M}\ \ddot{\boldsymbol{q}}(t) + \boldsymbol{V}\ \dot{\boldsymbol{q}}(t) + \boldsymbol{K}\ \boldsymbol{q}(t) = \boldsymbol{f}(t) \tag{2.1}$$

where $\boldsymbol{M}$, $\boldsymbol{V}$ and $\boldsymbol{K} \in \mathbb{R}^{n\times n}$ denote the symmetric mass, viscous damping and stiffness matrix, respectively. The vector $\boldsymbol{q} \in \mathbb{R}^{n\times 1}$ defines the general displacement vector, and its dots represent the corresponding first and second time derivative. The vector $\boldsymbol{f}(\mathrm{t}) \in \mathbb{R}^{n\times 1}$ describes the external loading of the system. Here n denotes the number of degrees of freedom (DoF). From the EoMs in Equation 2.1, the transfer functions matrix of the system, $\boldsymbol{H}(\omega) \in \mathbb{R}^{n\times n}$, which defines the response in the frequency domain, can be obtained by a Laplace transform [CK06]. The Laplace transform $\mathscr{L}$ is defined as

$$\boldsymbol{\Gamma}(t) \triangleq \mathscr{L}[\boldsymbol{\gamma}(t)] = \int_0^\infty e^{-st}\boldsymbol{\gamma}(t)\mathrm{dt} \tag{2.2}$$

where $\boldsymbol{\gamma}(t)$ is a vector in the time domain, for instance the displacement or external load vector of a dynamic system. In the frequency domain the EoMs are defined as

$$\boldsymbol{Z}(j\omega)\boldsymbol{Q}(j\omega) = \boldsymbol{F}(j\omega) \tag{2.3}$$

$$\boldsymbol{Z}(j\omega) = (-\omega^2\boldsymbol{M} + j\omega\boldsymbol{V} + \boldsymbol{K}) \tag{2.4}$$

where $\boldsymbol{Z}(j\omega)$ is the dynamic stiffness of a system, also known as the impedance function, and j with $j^2 = -1$ the imaginary number. $\boldsymbol{Q}(j\omega)$ and $\boldsymbol{F}(j\omega)$ denote the Laplace transform of the displacement vector $\boldsymbol{q}(t)$ and load vector $\boldsymbol{f}(t)$, respectively. The transfer function $\boldsymbol{H}(j\omega)$ is finally obtained by

$$\boldsymbol{H}(j\omega) = \boldsymbol{Z}(j\omega)^{-1}. \tag{2.5}$$

2.1.2 First order form

To obtain the first order form of Equation 2.1, a state-vector $\boldsymbol{z}=[\boldsymbol{q}\ \dot{\boldsymbol{q}}]^T$ is defined. Furthermore, the external load vector $\boldsymbol{f}(\mathrm{t})$ can be expressed in terms of the input vector $\boldsymbol{u} \in \mathbb{R}^{n_u\times 1}$ and the rectangular transformation matrix $\boldsymbol{U}$, where n_u is the number of inputs [Abr12]

$$\boldsymbol{f}(t) = \boldsymbol{U}\ \boldsymbol{u}(t). \tag{2.6}$$

Enlarging Equation 2.1 with a dummy equation $\boldsymbol{I}\dot{\boldsymbol{q}} - \boldsymbol{I}\dot{\boldsymbol{q}} = 0$ leads to

$$\begin{bmatrix}\boldsymbol{V} & \boldsymbol{M}\\ \boldsymbol{I} & \boldsymbol{0}\end{bmatrix} + \begin{bmatrix}\boldsymbol{K} & \boldsymbol{0}\\ \boldsymbol{0} & -\boldsymbol{I}\end{bmatrix} = \begin{bmatrix}\boldsymbol{f}(t)\\ \boldsymbol{0}\end{bmatrix} \tag{2.7}$$

which can be rewritten by incorporating the state-vector $\boldsymbol{z}=[\boldsymbol{q}\ \dot{\boldsymbol{q}}]^T$ and Equation 2.6 as

$$\dot{\boldsymbol{z}}(t) = -\begin{bmatrix} \boldsymbol{0} & -\boldsymbol{I} \\ \boldsymbol{M}^{-1}\boldsymbol{K} & \boldsymbol{M}^{-1}\boldsymbol{V} \end{bmatrix}^{-1} \begin{bmatrix} \boldsymbol{K} & \boldsymbol{0} \\ \boldsymbol{0} & -\boldsymbol{I} \end{bmatrix} \boldsymbol{z}(t) + \begin{bmatrix} \boldsymbol{V} & \boldsymbol{M} \\ \boldsymbol{I} & \boldsymbol{0} \end{bmatrix}^{-1} \begin{bmatrix} \boldsymbol{U}\boldsymbol{u}(t) \\ \boldsymbol{0} \end{bmatrix} \tag{2.8}$$

$$= \underbrace{-\begin{bmatrix} \boldsymbol{0} & -\boldsymbol{I} \\ \boldsymbol{M}^{-1}\boldsymbol{K} & \boldsymbol{M}^{-1}\boldsymbol{V} \end{bmatrix}}_{\boldsymbol{A}} \boldsymbol{z}(t) + \underbrace{\begin{bmatrix} \boldsymbol{0} \\ \boldsymbol{M}^{-1}\boldsymbol{U} \end{bmatrix}}_{\boldsymbol{B}} \boldsymbol{u}(t). \tag{2.9}$$

Similar to Equation 2.6, it is possible to transform the outputs of a system, $\boldsymbol{y}$(t), as [Abr12]

$$\boldsymbol{y}_d = \underbrace{\begin{bmatrix} \boldsymbol{P}_d & \boldsymbol{0} \end{bmatrix}}_{\boldsymbol{C}_d} \boldsymbol{z}(t) \qquad\qquad \boldsymbol{y}_v = \underbrace{\begin{bmatrix} \boldsymbol{0} & \boldsymbol{P}_v \end{bmatrix}}_{\boldsymbol{C}_v} \boldsymbol{z}(t) \tag{2.10}$$

where the subscribts d and v denote displacement and velocity, respectively. If the output $\boldsymbol{y}$(t) is measured in form of accelerations, which is the case in this thesis, this transform results in

$$\boldsymbol{y}_a = \begin{bmatrix} \boldsymbol{0} & \boldsymbol{P}_a \end{bmatrix} \dot{\boldsymbol{z}}(t) = \begin{bmatrix} \boldsymbol{0} & \boldsymbol{P}_a \end{bmatrix} \Big(\boldsymbol{A}\ \boldsymbol{z}(t) + \boldsymbol{B}\ \boldsymbol{u}(t) \Big) \tag{2.11}$$

$$= \underbrace{\begin{bmatrix} \boldsymbol{0} & \boldsymbol{P}_a \end{bmatrix} \boldsymbol{A}}_{\boldsymbol{C}_a} \boldsymbol{z}(t) + \underbrace{\begin{bmatrix} \boldsymbol{0} & \boldsymbol{P}_a \end{bmatrix} \boldsymbol{B}}_{\boldsymbol{D}} \boldsymbol{u}(t). \tag{2.12}$$

From Equation 2.10 and 2.12 it can be seen, that the state-matrix $\boldsymbol{C}$ is dependent on the type of output and the state-matrix $\boldsymbol{D}$ can be non-zero only if the output is measured in accelerations. Generally, it can be stated that the $\boldsymbol{C}$ matrix includes the corresponding eigenvectors of the dynamic system, which appear in the transformation matrices $\boldsymbol{P}_d$, $\boldsymbol{P}_v$ and $\boldsymbol{P}_a$. Thus, the first order form of the general EoMs is defined as

$$\dot{\boldsymbol{z}}(t) = \boldsymbol{A}\ \boldsymbol{z}(t) + \boldsymbol{B}\ \boldsymbol{u}(t) \tag{2.13}$$

$$\boldsymbol{y}(t) = \boldsymbol{C}\ \boldsymbol{z}(t) + \boldsymbol{D}\ \boldsymbol{u}(t) \tag{2.14}$$

where $\boldsymbol{A} \in \mathbb{R}^{n_z \times n_z}$, $\boldsymbol{B} \in \mathbb{R}^{n_z \times n_u}$, $\boldsymbol{C} \in \mathbb{R}^{n_y \times n_z}$ and $\boldsymbol{D} \in \mathbb{R}^{n_y \times n_u}$. The sizes of the matrices defined by n_z, n_u and n_y are equal to the number of states, inputs and outputs, respectively. The state-space matrices are summarized in Equation 2.15

$$\boldsymbol{A} = -\begin{bmatrix} \boldsymbol{0} & -\boldsymbol{I} \\ \boldsymbol{M}^{-1}\boldsymbol{K} & \boldsymbol{M}^{-1}\boldsymbol{V} \end{bmatrix} \qquad \boldsymbol{B} = \begin{bmatrix} \boldsymbol{0} \\ \boldsymbol{M}^{-1}\boldsymbol{U} \end{bmatrix} \qquad \boldsymbol{C} = \begin{cases} [\boldsymbol{P}_d & \boldsymbol{0}] \\ [\boldsymbol{0} & \boldsymbol{P}_v] \\ [\boldsymbol{0} & \boldsymbol{P}_a]\boldsymbol{A} \end{cases} \qquad \boldsymbol{D} = \begin{cases} [\boldsymbol{0} & \boldsymbol{0}] \\ [\boldsymbol{0} & \boldsymbol{0}] \\ [\boldsymbol{0} & \boldsymbol{P}_a]\boldsymbol{B} \end{cases}. \tag{2.15}$$

In terms of the $\boldsymbol{C}$ and $\boldsymbol{D}$ matrices only one of the cases are valid, dependent on the type of measurement. The upper case of $\boldsymbol{C}$ and $\boldsymbol{D}$ if displacements are measured, the second case if velocities and the third case if accelerations are maesured. Equivalent to Equation 2.5, the transfer function matrix $\boldsymbol{H}(j\omega)$ can also be expressed in terms of the state-space matrices

$$\boldsymbol{H}(j\omega) = \boldsymbol{C}((j\omega)\boldsymbol{I} - \boldsymbol{A})^{-1}\boldsymbol{B} + \boldsymbol{D}. \tag{2.16}$$

2.1.3 Generalized eigenvalue problem

The generalized eigenvalue problem (EvP) of the undamped EoMs is defined as [CK06]

$$(\boldsymbol{K} - \omega_i^2 \boldsymbol{M})\boldsymbol{\phi}_i = \boldsymbol{0} \qquad\qquad i = 1, 2...n \tag{2.17}$$

where ω_i denotes the natural eigenfrequency and $\boldsymbol{\phi}_i$ the corresponding eigenvector of the i:th mode. The eigenfrequencies can be calculated by solving

$$\det(\boldsymbol{K} - \omega_i^2 \boldsymbol{M}) = \boldsymbol{0} \qquad\qquad i = 1, 2...n. \tag{2.18}$$

The EvP can be considered in different domains or for different approaches. In this thesis, the modal domain and the state-space approach are considered.

Transformation to the modal domain

The transformation to the modal domain is defined as [CK06]

$$\boldsymbol{q}(t) = \boldsymbol{\Phi}\boldsymbol{\eta}(t) \tag{2.19}$$

where $\boldsymbol{\eta}$ denotes the generalized (modal) coordinates and $\boldsymbol{\Phi}$ a matrix including the eigenvectors $\boldsymbol{\phi}_i$ as shown in Equation 2.23. Inserting Equation 2.19 in the EoMs (Equation 2.1) and multiplying each term from the left with $\boldsymbol{\Phi}^T$ leads to the uncoupled EoMs in generalized coordinates

$$\boldsymbol{\Phi}^T \boldsymbol{M} \boldsymbol{\Phi}\ \ddot{\boldsymbol{\eta}}(t) + \boldsymbol{\Phi}^T \boldsymbol{V} \boldsymbol{\Phi}\ \dot{\boldsymbol{\eta}}(t) + \boldsymbol{\Phi}^T \boldsymbol{K} \boldsymbol{\Phi}\ \boldsymbol{\eta}(t) = \boldsymbol{\Phi}^T \boldsymbol{f}(t). \tag{2.20}$$

The orthogonality of the eigenvectors ($\omega_r \neq \omega_s$, i.e. $\Phi_r^T \boldsymbol{M} \Phi_s$=0, $\Phi_r^T \boldsymbol{V} \Phi_s$=0 and $\Phi_r^T \boldsymbol{K} \Phi_s$=0) uncouples the EoMs, [CK06]. With the definitions

$$\boldsymbol{M}_m = \boldsymbol{\Phi}^T \boldsymbol{M} \boldsymbol{\Phi} \qquad \boldsymbol{V}_m = \boldsymbol{\Phi}^T \boldsymbol{V} \boldsymbol{\Phi} \qquad \boldsymbol{K}_m = \boldsymbol{\Phi}^T \boldsymbol{K} \boldsymbol{\Phi} = \boldsymbol{\Lambda} \qquad \boldsymbol{f}_m = \boldsymbol{\Phi}^T \boldsymbol{f} \tag{2.21}$$

where the subscript m denotes the modal domain. The uncoupled EoMs can be expressed in generalized coordinates as

$$\boldsymbol{M}_m\ \ddot{\boldsymbol{\eta}}(t) + \boldsymbol{V}_m\ \dot{\boldsymbol{\eta}}(t) + \boldsymbol{K}_m\ \boldsymbol{\eta}(t) = \boldsymbol{f}_m(t) \tag{2.22}$$

where $\boldsymbol{\Phi}$ and $\boldsymbol{\Lambda}$ are defined as

$$\boldsymbol{\Phi} = \begin{bmatrix} \boldsymbol{\phi}_1 & \boldsymbol{\phi}_2 & \cdots & \boldsymbol{\phi}_n \end{bmatrix} \qquad\qquad \boldsymbol{\Lambda} = \begin{bmatrix} \omega_1^2 & \boldsymbol{0} & \boldsymbol{0} \\ \boldsymbol{0} & \ddots & \boldsymbol{0} \\ \boldsymbol{0} & \boldsymbol{0} & \omega_n^2 \end{bmatrix}. \tag{2.23}$$

Thus, the generalized EvP in the modal domain is defined as

$$(\boldsymbol{K}_m - \boldsymbol{\Lambda} \boldsymbol{M}_m) \boldsymbol{\Phi} = \boldsymbol{0} \tag{2.24}$$

which means that model truncation is included, if $\boldsymbol{\Phi}$ contains a reduced amount of modes as column vectors.

Eigenvalue problem of the state-space approach

The EvP state space form results in

$$\dot{\boldsymbol{z}}(t) = \boldsymbol{A}\boldsymbol{z}(t). \tag{2.25}$$

Equation 2.25 defines a homogenous linear time-invariant system with the general solution on the form $\boldsymbol{z}(t) = e^{\lambda t}\boldsymbol{\theta}$ [Mei97]. Thus, Equation 2.25 holds

$$\boldsymbol{A}\boldsymbol{\theta}_i = \boldsymbol{\lambda}_i \boldsymbol{\theta}_i \qquad\qquad i = 1, 2...n \tag{2.26}$$

which is similar to the standard EvP $\boldsymbol{X}\boldsymbol{z}$=$\lambda\boldsymbol{z}$. The eigenvalues of the state-space approach occur either as real eigenvalues or in complex conjugated pairs [CK06]. Complex conjugated pairs of eigenvalues lead to complex conjugated eigenvectors. The solution of the state-space EvP is defined as

$$(\boldsymbol{A} - \lambda_i \boldsymbol{I})\boldsymbol{\theta}_i = \boldsymbol{0}. \tag{2.27}$$

All eigenvectors $\boldsymbol{\theta}_i$ and eigenvalues λ_i can be collected in matrix form similar to Equation 2.23.

2.2 Pretest planning

2.2.1 The method of effective independence

The EfI introduced in [Kam10] is an sub-optimal technique for sensor placement. The contribution of each sensor, defined in a so called candidate sensor set, to the determinant of the Fisher information matrix (FIM), denoted as $\mathscr{F}$, is evaluated. Thereafter, the sensors are ranked in ascending order. The sensor with the lowest contribution, i.e. the lowest ranked sensor, is eliminated and the new (reduced) candidate sensor set is re-ranked. The procedure is repeated until the target amount of sensors is reached. The FIM is the inverse of the covariance matrix $\boldsymbol{P}$, which is defined as

$$\boldsymbol{P} = \mathscr{E}[(\boldsymbol{q} - \widehat{\boldsymbol{q}})(\boldsymbol{q} - \widehat{\boldsymbol{q}})^T] = \mathscr{F}^{-1}. \tag{2.28}$$

$\mathscr{F}$ is defined as

$$\mathscr{F} = \boldsymbol{\Phi}_s^T \boldsymbol{W} \boldsymbol{\Phi}_s \tag{2.29}$$

where $\boldsymbol{\Phi}_s$ is the truncated eigenvector (modal) matrix, including only the partitions related to the candidate sensor set. $\boldsymbol{W}$ defines a weighting matrix, which is in this thesis an identity matrix. In Equation 2.28, $\mathscr{E}$ is the expectation operator and $\boldsymbol{q}$ the displacement vector with its updated solution denoted by an superscript hat ($\widehat{\bullet}$). Minimzing the covariance in Equation 2.28 maximizes the FIM. Hence, the EfI method maximizes the (determinant of) FIM. In [Kam10], each sensor contribution of the effective independence vector EfI_i, is defined as

$$\text{EfI}_i = \frac{\det(\mathscr{F}) - \det(\mathscr{F}_i)}{\det(\mathscr{F})}. \tag{2.30}$$

The equation is bounded by $0 \leq \text{EfI}_i \leq 1$, where 1 denotes a high contribution to the linear independence and 0 denotes no contribution and hence a poorly located sensor. In Equation 2.30, $\mathscr{F}_i$ denotes the FIM when the i:th sensor is rejected in the truncated modal matrix $\boldsymbol{\Phi}_s$.

2.3 Correlation analysis

A correlation anlysis is used to compare two models and estimate the fit between the results. The two different models can be of any type, for instance two FE models, two experimental models or a combination of both. In this thesis, the modal assurance criterion (MAC) as well as two special cases, the auto modal assurance criterion (AutoMAC) and the substructure modal assurance criterion (SUMAC), are used. All three criteria investigate the correlation between two sets of vectors.

2.3.1 The modal assurance criterion

The modal assurance criterion (MAC) defines the correlation of two vector sets, i.e. modal vectors [All02]. The MAC is defined as

$$\text{MAC} = \frac{|\boldsymbol{\Phi}_a^H \boldsymbol{\Phi}_b|^2}{(\boldsymbol{\Phi}_a^H \boldsymbol{\Phi}_a)(\boldsymbol{\Phi}_b^H \boldsymbol{\Phi}_b)} \tag{2.31}$$

where subscript a denotes the mode shapes of the first model and subscript b the mode shapes of the second model. Superscript H denotes the Hermitian transpose. The MAC calculates, if the two considered vectors a and b have the same directions, even if they are different in magnitude [Ewi00]. The MAC is bounded by 0 and 1, where 0 denotes no correalation, i.e. the vectors a and b point in orthogonal directions and 1 a perfect match of the vectors. As mentioned in [Ewi00], the MAC is a deviation measure in least-squares-sense and can be used for real, as well as complex eigenvectors.

Commonly, the MAC is used to compare experimentally measured mode shapes with FE obtained mode shapes, to evaluate the similarity between both. A perfect fit, i.e. MAC=1, does normally not result because small differences between experiments and simulations occur. Thus, it is necessary to define problem dependent limits, to distinguish well- from uncorrelated models. If no specific requirements are defined, MAC ≥ 0.9 is considered as well-correlated models [Ewi00] .

2.3.2 The auto modal assurance criterion

A special case of the MAC is the so-called AutoMAC [Ewi00]. The AutoMAC also considers the correlation of two modal vectors, but with the special characteristic that the modal vectors are identical. In other words, they correspond to the same model. Thus, the AutoMAC is defined as

$$\text{AutoMAC} = \frac{|\boldsymbol{\Phi}_a^H \boldsymbol{\Phi}_a|^2}{(\boldsymbol{\Phi}_a^H \boldsymbol{\Phi}_a)(\boldsymbol{\Phi}_a^H \boldsymbol{\Phi}_a)} \tag{2.32}$$

The reason to estimate the AutoMAC is to analyze the cross-correlation between mode shapes. This defines if mode shapes are clearly separated and thus each mode shape can be identified, or if similar mode shapes occur that can therefore not be identified. An AutoMAC always results in AutoMAC=1 (perfect fit) in the diagonal and in the off-diagonal between 0 and 1. In [Ewi00] and [Kam10], the AutoMAC is used in the pretest planning. The AutoMAC is thereby calculated for the considered sensor sets, i.e the final sensor set obtained from the EfI in Equation 2.30, to evaluate if the chosen positions can identify all occuring modes in the range of interest. Overall, a reduced sensor set always results in a higher AutoMAC, i.e. in a higher cross-correlation of different modes, than a full sensor set.

2.3.3 The substructure modal assurance criterion

The second special case of the MAC is the SUMAC [Val10]. In this case the influence of the coupling of a substructure is evaluated. The mode shapes of a single substructure (model) are compared with the mode shapes of that same substructure coupled to another structure. The SUMAC is thus defined as

$$\text{SUMAC} = \frac{|\boldsymbol{\Phi}_g^{(s)^H} \boldsymbol{\Phi}_l^{(s)}|^2}{(\boldsymbol{\Phi}_g^{(s)^H} \boldsymbol{\Phi}_g^{(s)})(\boldsymbol{\Phi}_l^{(s)^H} \boldsymbol{\Phi}_l^{(s)})}. \tag{2.33}$$

Superscript (s) denotes the substructure to analyze and $\boldsymbol{\Phi}_l$ the mode shape of that substructure (s) in an individual setting (local) and $\boldsymbol{\Phi}_g$ the global mode shape, i.e. the mode shape of that substructure of interest coupled to another component. The SUMAC denotes, if a mode shape of substructure s is highly or slightly affected in the assembled model.

2.4 Model updating

The main aim of a model updating or calibration is to minimize a defined deviation metric between two models, i.e. between experimentally obtained FRFs $\boldsymbol{H}^X$ and the corresponding FRFs of an FE simulation $\boldsymbol{H}^{FE}$. The FE model is thereby the model which is updated. The experimental model is considered as the true system. The calibration of the FE model is performed by updating the mass and stiffness matrices $\boldsymbol{M}$ and $\boldsymbol{K}$ in the EoMs (Equation 2.1). During the updating process, it is very important to limit the physical properties of the model. This means that $\boldsymbol{M}$ and $\boldsymbol{K}$ need to be updated related to model parameters, such as Young's moduli, or material thicknesses and not by manually updating the values in the two matrices. Furthermore, these material parameters should be related to their true properties after calibration. A Young's modulus for steel (E=210 GPa) should for instance not end up in a range of a Young's modulus for aluminum (E=71 GPa). The model updating procedure is summarized by the following steps.

1. Mathematical models of the experimentally obtained data set as well as the full FE model are created, i.e. state space models of both. The experimental model is the reference data, wheras the FE model is calibrated.

2. A vector of inaccurate model parameters $\boldsymbol{P}$ is defined.

3. The eigenvalue problem is solved for the full FE model at nominal parameter settings $\boldsymbol{P}_0$, where the mass and stiffness matrices are functions of $\boldsymbol{P}$.

4. A model reduction procedure is applied on the FE model to consider only the (frequency) range of interest.

5. Damping is equalized for the experimental and FE systems to a sufficient high value.

6. A minimization to a defined metric is conducted by a variation of the parameters in $\boldsymbol{P}$. Therefore, the upper and lower bounds are defined for each parameter and multiple Latain hypercube (LHC) [MBC00] sets are created. $\boldsymbol{P}^*$ is the calibrated parameter set, i.e. the set which leads to the minimal deviation between experiment and simulation.

7. The inaccuracy or rather uncertainties in the parameters of $\boldsymbol{P}^*$ are analzed via bootstrapping [Vak+17].

The model updating procedure is considered for MDOF systems which are described by the general EoMs (Equation 2.1). The parametrization of the FE model with the parameter vector $\boldsymbol{P}$ defines a dependence on $\boldsymbol{P}$ for the mass and stiffness matrices, such that $\boldsymbol{M}$=$\boldsymbol{M}(\boldsymbol{P})$ and $\boldsymbol{K}$=$\boldsymbol{K}(\boldsymbol{P})$. It is possible to express $\boldsymbol{P}$ in relation to normalized parameters $\boldsymbol{p}$ and fixed nominal parameters $\boldsymbol{P}_0$, i.e $\boldsymbol{P}$=$\boldsymbol{P}_0(1+\boldsymbol{p})$ [AK15]. With the general state-space approach, described in Section 2.1.2, the FRFs for the experimental and FE model are defined as

$$\boldsymbol{H}^X(\mathrm{j}\omega) = \boldsymbol{C}(\mathrm{j}\omega\boldsymbol{I} - \boldsymbol{A})^{-1}\boldsymbol{B} + \boldsymbol{D} \tag{2.34}$$

$$\boldsymbol{H}^{FE}((\mathrm{j}\omega), \boldsymbol{p}) = \boldsymbol{C}(\mathrm{j}\omega\boldsymbol{I} - \boldsymbol{A}(\boldsymbol{p}))^{-1}\boldsymbol{B}(\boldsymbol{p}) + \boldsymbol{D}. \tag{2.35}$$

To find the parameter set $\boldsymbol{p}$=$\boldsymbol{p}^*$, which minimzes the deviation between $\boldsymbol{H}^{FE}(\boldsymbol{p})$ and $\boldsymbol{H}^X$, a deviation metric needs to be defined, which is estimated for multiple parameter sets. An deviation metric, that captures effects of small as well as high responses similarly, is suggested to be effective [AK15].

2.4.1 Deviation metric

A frequency based deviation metric δ for the calibration problem is defined by [AK15] as

$$\delta = \varepsilon^H\varepsilon \qquad \text{with} \quad \varepsilon(\boldsymbol{p}) = \log_{10}\mathrm{vect}(\boldsymbol{H}^{FE}(\boldsymbol{p})) - \log_{10}\mathrm{vect}(\boldsymbol{H}^X) \tag{2.36}$$

where superscript H denotes the Hermitian transpose. The expression vect(.) denotes a vectorizing operation of a matrix, where a column vector of $n_y n_u n_f$ x 1 is obtained. The non-linear least-squares minimzation problem is defined as

$$\boldsymbol{p}^* = \arg\min \frac{\varepsilon(\boldsymbol{p})^H\varepsilon(\boldsymbol{p})}{N}. \tag{2.37}$$

As previously mentioned, the deviation metric needs to be estimated for multiple parameter sets. The first set is defined by the nominal parameters, i.e. $\boldsymbol{p}$=0 such that $\boldsymbol{P}$=$\boldsymbol{P}_0$. The other parameter sets are generated with the aid of the LHC sampling, which is described in [MBC00]. The minimization is performed by a Levenberg-Marquardt algorithm, which is a non-linear least-squares minimzation and described in more detail in [[Lev44],[Mar63],[AEP13]]. The mentioned estimation of parameter uncertainties via bootstrapping is further explained in Section 2.4.2. Apart from the minimzation of the defined metric, it is suggested, to analyze the identifiability of the paramteters, described by the inverse of the FIM [AK15]. Parameters with a low identifiability, i.e. a high value in the inverse of the FIM, shall thereby not be considered in the calibration procedure, since they are not reliable.

2.4.2 Bootstrapping

The bootstrapping method is explained in detail in [HTJ09] and roughly summarized in this section. Bootstrapping is a method, that calculates the statistical accuracy of a model. It can be described as sampling with replacement. The data points z_n=(x_n, y_n) of the fitted model is collected in a so-called training set $\boldsymbol{Z}$=(z_1,z_2,...,z_n). From this set, a new set $\boldsymbol{Z}_B$ of same length as $\boldsymbol{Z}$ is created by randomly choosing data points z_n out of $\boldsymbol{Z}$. Replacement means, that the same data set z_n can be used multiple times. A fixed amount of bootstrap samples n_b defines how many different new sets $\boldsymbol{Z}_B$ are created. With these n_b data sets, any kind of statistical information, for instance prediction errors or variance can be estimated.

In this thesis, bootstrapping is applied on the raw test data. Thus, the original set of experimentally obtained FRFs, $\boldsymbol{H}^X$ denotes the training set, where n_b=20 new sets $\boldsymbol{H}_b^X$ are created by randomly picking data points at the 2000 frequency lines. The model fitting leads to n_b=20 calibrated parameter vectors $\boldsymbol{p}_b^*$, which are used to estimate the statictical information corresponding to the mean and variance in $\boldsymbol{p}_b^*$. The bootstrapping parameter vector can be expressed similarly to Equation 2.36 and 2.37 as:

$$\boldsymbol{p}_b^* = \arg\min \frac{\gamma(\boldsymbol{p})^H \gamma(\boldsymbol{p})}{N} \quad \text{and} \quad \gamma(\boldsymbol{p}) = \log_{10}\text{vect}(\boldsymbol{H}^{FE}(\boldsymbol{p}) - \log_{10}\text{vect}(\boldsymbol{H}_b^X) \tag{2.38}$$

2.4.3 Damping equalization

The term in Equation 2.1, which has not been discussed yet, is the systems damping matrix $\boldsymbol{V}$. The damping has to be estimated for the mathematical model of the EMA, as well as for the FE model. A damping equalization, in which equal modal damping for each mode is used for the experimental model and equal viscous damping based on that equal modal damping is applied on the FE model, is suggested in [AK15]. This method is used to avoid mode pairing and to regularize the minimzation problem. The described two damping conditions are defined as

$$\xi_i = \xi_0 \quad \forall i \qquad \text{for the EMA model} \tag{2.39}$$

$$\boldsymbol{V} = \boldsymbol{M}\boldsymbol{T}\text{diag}(m_n^{-1})\text{diag}(2\xi_0 m_n \omega_n)\text{diag}(m_n^{-1})\boldsymbol{T}^T\boldsymbol{M} \qquad \text{for the FE model} \tag{2.40}$$

where Equation 2.40 denotes the viscous damping for given mass and stiffness properties of a system [CK06]. The term ξ_0 denotes the constant modal damping, m_n the modal masses, ω_n the eigenfrequencies and $\boldsymbol{T}$ a matrix containing all eigenvectors obtained from the general EvP of the undamped system (Section 2.1.3). Thus, for each LHC computed parameter set $\boldsymbol{p}$, the corresponding damping matrix $\boldsymbol{V}(\boldsymbol{p})$ is evaluated with respect to Equation 2.40 with $\boldsymbol{M}(\boldsymbol{p})$ and $\boldsymbol{K}(\boldsymbol{p})$.

New FRFs for the experimental model with equalized damping are obtained by modification of the state-matrix $\boldsymbol{A}$ of the state-space approach in Equation 2.16. Multiplication of $\boldsymbol{A}$ with the eigenvectors $\boldsymbol{T}$ obtained from the general undamped EvP leads to a diagonalization as

$$\overline{\boldsymbol{A}} = \boldsymbol{T}^{-1}\boldsymbol{A}\boldsymbol{T} = \text{diag}(\lambda_n) \tag{2.41}$$

where λ_n are the complex conjugated poles. For a low relative damping ($\xi \ll 1$), the modal damping is related to the poles as

$$\xi_n = -\frac{\mathscr{R}(\lambda_n)}{|\mathscr{C}(\lambda_n)|} \tag{2.42}$$

where $\mathscr{R}$ and $\mathscr{C}$ denote the real and imaginary part of λ_n, respectively. Together with Equation 2.39 and 2.41, the new FRFs for the experimental model holds

$$\widetilde{\lambda_n} = (i - \xi_0)\mathscr{C}(\lambda_n) \quad \forall \mathscr{C}(\lambda_n) > 0 \quad \text{and} \quad \widetilde{\lambda_n} = (i + \xi_0)\mathscr{C}(\lambda_n) \quad \forall \mathscr{C}(\lambda_n) < 0 \tag{2.43}$$

$$\widetilde{\boldsymbol{A}} = \mathrm{diag}(\widetilde{\lambda_n}) \tag{2.44}$$

$$\boldsymbol{H}^X(\mathrm{i}\omega) = \boldsymbol{C}\boldsymbol{T}(\mathrm{i}\omega\boldsymbol{I} - \widetilde{\boldsymbol{A}})^{-1}\boldsymbol{T}^{-1}\boldsymbol{B} + \boldsymbol{D}. \tag{2.45}$$

2.4.4 Reduced order modeling

Another issue in the model calibration procedure is the size, i.e. the number of DoFs of the FE model to calibrate. It is well known, that the computational costs increase with an increasing number of DoFs. Thus, it is necessary to create reduced models, which sufficiently cover the range of interest. In the calibration procedure, the range of interest is defined by the frequency range of interest, $\omega_n \in[\omega_{min}\ \omega_{max}]$. Thus, the general EvP for each parameter setting needs to be solved in the defined range only. A common approach is to reduce the system matrices $\boldsymbol{M}$ and $\boldsymbol{K}$ with the eigenvector matrix $\boldsymbol{T}$ for the range of interest, as described in [Ewi00]. Since the model reduction also requires computational resources, [AK15] suggests to use a fixed reduction basis for all parameter settings together with a first order Taylor series expansion, i.e. gradients of the reduced order matrices, to form the reduced model. The fixed reduction basis is the eigenvector matrix $\boldsymbol{T}_0$, which includes the eigenvectors for the nominal parameter set $\boldsymbol{p}_0$. The reduction of the system matrices for any parameter setting $\boldsymbol{p}$ is then defined as

$$\overline{\boldsymbol{M}}(\boldsymbol{p}) = \boldsymbol{T}_0^T\boldsymbol{M}\boldsymbol{T}_0 \qquad\qquad \overline{\boldsymbol{K}}(\boldsymbol{p}) = \boldsymbol{T}_0^T\boldsymbol{K}\boldsymbol{T}_0 \tag{2.46}$$

where the nominal reduced matrices are $\overline{\boldsymbol{M}}(\boldsymbol{p}_0)$=$\overline{\boldsymbol{M}}_0$ and $\overline{\boldsymbol{K}}(\boldsymbol{p}_0)$=$\overline{\boldsymbol{K}}_0$. The gradients of each parameter i in the parameter vector $\boldsymbol{p}$ are defined as

$$\overline{\boldsymbol{M}}_{,i} = \boldsymbol{T}_0^T\left(\frac{d\boldsymbol{M}}{dp_i}|_{p=p_0}\right)\boldsymbol{T}_0 \qquad\qquad \overline{\boldsymbol{K}}_{,i} = \boldsymbol{T}_0^T\left(\frac{d\boldsymbol{K}}{dp_i}|_{p=p_0}\right)\boldsymbol{T}_0 \tag{2.47}$$

and the first order Taylor series expansion leads to

$$\widetilde{\boldsymbol{M}}(\boldsymbol{p}) = \overline{\boldsymbol{M}}_0 + \sum_{i=1}^{n}(p_i - p_{i,0})\overline{\boldsymbol{M}}_{,i} \qquad\qquad \widetilde{\boldsymbol{K}}(\boldsymbol{p}) = \overline{\boldsymbol{K}}_0 + \sum_{i=1}^{n}(p_i - p_{i,0})\overline{\boldsymbol{K}}_{,i} \tag{2.48}$$

where $p_{i,0}$ is the nominal parameter of the i:th parameter. Equation 2.47 and 2.48 are estimated from the full model once and then used for the whole calibration procedure. The FRFs of the reduced FE model are then defined as

$$\boldsymbol{H}^{FE}(\mathrm{i}\omega), \boldsymbol{p}) = \widetilde{\boldsymbol{C}}(\mathrm{i}\omega\boldsymbol{I} - \widetilde{\boldsymbol{A}}(\boldsymbol{p}))^{-1}\widetilde{\boldsymbol{B}}(\boldsymbol{p}) + \widetilde{\boldsymbol{D}} \tag{2.49}$$

$$\widetilde{\boldsymbol{A}} = \begin{bmatrix} \boldsymbol{0} & \boldsymbol{I} \\ -\widetilde{\boldsymbol{M}}^{-1}\widetilde{\boldsymbol{K}} & -\widetilde{\boldsymbol{M}}^{-1}\widetilde{\boldsymbol{V}} \end{bmatrix} \qquad \widetilde{\boldsymbol{B}} = \left[\boldsymbol{0} - \widetilde{\boldsymbol{M}}^{-1}\boldsymbol{T}_0^T U\right]\widetilde{\boldsymbol{C}} = \boldsymbol{C}\begin{bmatrix} \boldsymbol{T}_0 & \boldsymbol{0} \\ \boldsymbol{0} & \boldsymbol{T}_0 \end{bmatrix} \qquad \widetilde{\boldsymbol{D}} = \boldsymbol{D} \tag{2.50}$$

where $\widetilde{\boldsymbol{V}}$ is estimated by Equation 2.40 with $\widetilde{\boldsymbol{M}}$ and $\widetilde{\boldsymbol{K}}$, respectively.

2.5 Dynamic substructure synthesis

As already mentioned, a major challenge in FE modeling is the handling of large and complex structures. FE models of structures like aircrafts or cars can easily contain millions of DoFs, when modelling the whole assembly. This leads to large computational costs and should be reduced. A common approach to reduce the amount of DoFs is through dynamic substructuring [KRV08]. Substructuring means the division of a large structure into several substructures and analyzing them separately. The solutions are then assembled to estimate the behavior of the full structure. In [KRV08] it is also mentioned that substructuring is not only

considered in the FEA, but also allows the combination of analytically and experimentally established responses of substructures. Different methods of substructuring or coupling methods exists. For instance assembling in the physical, the modal and the frequency domain [KRV08] . Independent from the method, two conditions need to be satisfied when assembling multiple structures.

1. The compatibility condition, i.e. equal displacements at the interface points.
2. The equilibrium condition, i.e. the force equilibrium at the interface DoFs.

It is also suggested in [KRV08] that substructering occurs not only in different domains, but also in combination with model reduction. Furthermore, coupling can be handled by assuming interface displacements or forces as unknown. In this work, the so-called CMS with a Craig-Bampton (CB) reduction is considerd. The theoretical relations are shown in the following sections.

2.5.1 Component-mode-synthesis

The CMS is a method to couple systems in the modal domain [KRV08]. The transformation is done by the use of modal vectors and leads to a reduction of the system as long as not all eigenmodes of the system are included. As described in [CK06], the CMS considers different types of modes, for example free-interface modes, fixed-interface modes and rigid-body modes (RBMs). The theoretical background of the CMS is presented in this thesis according to [CK06]. In dynamic substructuring, the general EoMs (Equation 2.1) are considered for each substructure as

$$\boldsymbol{M}^{(s)}\ \ddot{\boldsymbol{q}}^{(s)} + \boldsymbol{V}^{(s)}\ \dot{\boldsymbol{q}}^{(s)} + \boldsymbol{K}^{(s)}\ \boldsymbol{q}^{(s)} = \boldsymbol{f}^{(s)} + \boldsymbol{g}^{(s)} \tag{2.51}$$

where the superscript s denotes the single substructures. The matrices $\boldsymbol{M}^{(s)}$, $\boldsymbol{V}^{(s)}$, $\boldsymbol{K}^{(s)}$ and $\boldsymbol{q}^{(s)}$ are the mass and stiffness matrix and the displacement vector of the component, respectively. In addition to the external applied forces $\boldsymbol{f}^{(s)}$ on the RHS, a vector including interface forces $\boldsymbol{g}^{(s)}$ occurs. The transformation to the modal domain for each substructure is defined by

$$\boldsymbol{q}^{(s)} = \boldsymbol{R}^{(s)}\boldsymbol{\eta}^{(s)} \tag{2.52}$$

where $\boldsymbol{\eta}^{(s)}$ are the displacements in generalized coordinates and $\boldsymbol{R}^{(s)}$ a matrix containing the considered mode shapes. Combining Equation 2.52 and 2.51 and multiplying each term by $\boldsymbol{R}^{(s)T}$ from the left leads to the decoupled EoMs in generalized coordinates.

$$\widehat{\boldsymbol{M}}^{(s)}\ \ddot{\boldsymbol{\eta}}^{(s)} + \widehat{\boldsymbol{V}}^{(s)}\ \dot{\boldsymbol{\eta}}^{(s)} + \hat{\boldsymbol{K}}^{(s)}\ \boldsymbol{\eta}^{(s)} = \widehat{\boldsymbol{f}}^{(s)} + \widehat{\boldsymbol{g}}^{(s)} \tag{2.53}$$

$$\widehat{\boldsymbol{M}}^{(s)} = \boldsymbol{R}^{(s)T}\boldsymbol{M}^{(s)}\boldsymbol{R}^{(s)} \qquad \widehat{\boldsymbol{V}}^{(s)} = \boldsymbol{R}^{(s)T}\boldsymbol{V}^{(s)}\boldsymbol{R}^{(s)} \qquad \widehat{\boldsymbol{K}}^{(s)} = \boldsymbol{R}^{(s)T}\boldsymbol{K}^{(s)}\boldsymbol{R}^{(s)} \tag{2.54}$$

$$\widehat{\boldsymbol{g}}^{(s)} = \boldsymbol{R}^{(s)T}\boldsymbol{g}^{(s)} \qquad \widehat{\boldsymbol{f}}^{(s)} = \boldsymbol{R}^{(s)T}\boldsymbol{f}^{(s)} \tag{2.55}$$

2.5.2 Normal modes

As mentioned before, the CMS includes a transformation to generalized coordinates as shown in Equation 2.52. The types of modes included in the transformation matrix $\boldsymbol{R}$ depend on the method used for the model reduction. Generally, all types of Ritz vectors are usable as reduction basis [CK06]. In this thesis, the CB reduction is used, which uses fixed-interface normal modes and interface constraint modes [CK06]. The different modes are used to capture the dynamic behavior of each substructure in the assembly process. Normal modes are eigenvectors of the substructure. Generally, the different mode types are defined from partitioning of the general EoMs

$$\begin{bmatrix}\boldsymbol{M}_{ii} & \boldsymbol{M}_{ib}\\ \boldsymbol{M}_{bi} & \boldsymbol{M}_{bb}\end{bmatrix}\begin{bmatrix}\ddot{\boldsymbol{q}}_i\\ \ddot{\boldsymbol{q}}_b\end{bmatrix} + \begin{bmatrix}\boldsymbol{V}_{ii} & \boldsymbol{V}_{ib}\\ \boldsymbol{V}_{bi} & \boldsymbol{V}_{bb}\end{bmatrix}\begin{bmatrix}\dot{\boldsymbol{q}}_i\\ \dot{\boldsymbol{q}}_b\end{bmatrix} + \begin{bmatrix}\boldsymbol{K}_{ii} & \boldsymbol{K}_{ib}\\ \boldsymbol{K}_{bi} & \boldsymbol{K}_{bb}\end{bmatrix}\begin{bmatrix}\boldsymbol{q}_i\\ \boldsymbol{q}_b\end{bmatrix} = \begin{bmatrix}\boldsymbol{0}_i\\ \boldsymbol{f}_b + \boldsymbol{g}_b\end{bmatrix} \tag{2.56}$$

where subscript i denotes internal DoFs and b boundary DoFs.

Fixed interface modes

The fixed interface modes are obtained by fixing the boundary DoFs, which leads to the 2_{nd} row in Equation 2.56 equal to zero, i.e $\boldsymbol{q}_b$=$\boldsymbol{0}$. Considered is an undamped system and the remaining equation holds

$$\boldsymbol{M}_{ii}\ddot{\boldsymbol{q}}_i + \boldsymbol{K}_{ii}\boldsymbol{q}_i = \boldsymbol{0}. \tag{2.57}$$

To obtain the resulting eigenmodes and eigenfrequencies, the general EvP is solved

$$(\boldsymbol{K}_{ii} - \boldsymbol{\omega}_{i,j}^2\boldsymbol{M}_{ii})\boldsymbol{\Phi}_{i,j} = \boldsymbol{0} \tag{2.58}$$

where $\boldsymbol{\Phi}_{i,j}$ includes the fixed interface vibration modes.

Static constraint modes

Static constraint modes include the static deformation when a unit displacement is applied on one boundary DoF in $\boldsymbol{q}_b$. The first row in Equation 2.56 then holds

$$\boldsymbol{M}_{ii}\ddot{\boldsymbol{q}}_i + \boldsymbol{M}_{ib}\ddot{\boldsymbol{q}}_b + \boldsymbol{K}_{ii}\boldsymbol{q}_i + \boldsymbol{K}_{ib}\boldsymbol{q}_b = \boldsymbol{0} \tag{2.59}$$

where the static part of $\boldsymbol{q}_i$ can be solved by neglecting inertia forces [Voo09]. This leads to

$$\boldsymbol{q}_{i,stat} = -\boldsymbol{K}_{ii}^{-1}\boldsymbol{K}_{ib}\boldsymbol{q}_b \equiv \boldsymbol{\Psi}_C\boldsymbol{q}_b \tag{2.60}$$

where $\boldsymbol{\Psi}_C$=$-\boldsymbol{K}_{ii}^{-1}\boldsymbol{K}_{ib}$ is called static condensation matrix and includes the static constraint modes. With these mode types, it is possible to reduce the full set of DoFs $\boldsymbol{q}$ to the boundary DoFs $\boldsymbol{q}_b$ as

$$\boldsymbol{q} = \begin{bmatrix}\boldsymbol{q}_i \\ \boldsymbol{q}_b\end{bmatrix} = \begin{bmatrix}\boldsymbol{\Psi}_C \\ \boldsymbol{I}\end{bmatrix}\boldsymbol{q}_b. \tag{2.61}$$

2.5.3 Craig-Bampton reduction

The CB transform or reduction method combines the two previously explained mode types, i.e. the fixed interface $\boldsymbol{\Phi}_{i,j}$ and static constraint modes $\boldsymbol{\Psi}_C$. The advantage of the static constraint modes in Equation 2.61 is, that the DoFs are retained in the global domain. This property enables a direct assembly of substructures. The resulting CB transform for each substructure s is defined in [CK06]

$$\begin{bmatrix}\boldsymbol{q}_b \\ \boldsymbol{q}_i\end{bmatrix}^{(s)} = \begin{bmatrix}\boldsymbol{I}_{bb} & \boldsymbol{0} \\ \boldsymbol{\Psi}_{ib} & \boldsymbol{\Phi}_{ik}\end{bmatrix}^{(s)} \begin{bmatrix}\boldsymbol{\eta}_b \\ \boldsymbol{\eta}_k\end{bmatrix}^{(s)} \equiv \boldsymbol{R}_{CB} \begin{bmatrix}\boldsymbol{\eta}_b \\ \boldsymbol{\eta}_k\end{bmatrix}^{(s)} \tag{2.62}$$

where subscript b denotes boundary DoFs in the global domain, k the modal DoFs, subscript i internal DoFs and η DoFs in generalized coordinates. The CB transform, Equation 2.62, together with Equation 2.51 leads to the CB mass and stiffness matrices

$$\widehat{\boldsymbol{M}}_{CB}^{(s)} = \begin{bmatrix}\widehat{\boldsymbol{M}}_{bb} & \widehat{\boldsymbol{M}}_{bk} \\ \widehat{\boldsymbol{M}}_{kb} & \boldsymbol{I}_{kk}\end{bmatrix}^{(s)} \qquad \widehat{\boldsymbol{K}}_{CB}^{(s)} = \begin{bmatrix}\widehat{\boldsymbol{K}}_{bb} & \boldsymbol{0}_{bk} \\ \boldsymbol{0}_{kb} & \boldsymbol{\Lambda}_{kk}\end{bmatrix}^{(s)}. \tag{2.63}$$

with

$$\boldsymbol{\Lambda} = \mathrm{diag}(\omega^2) \tag{2.64}$$

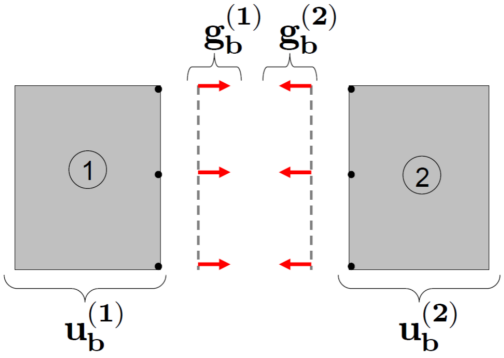

Figure 2.1: *Assembly of two substructures using interface displacements in a conforming mesh [Val10]. The vector $\boldsymbol{u}_b$ denotes the interface displacements which are calles $\boldsymbol{q}_b$ in this thesis.*

2.5.4 Assembly of substructures

The assembly or coupling of multiple substructurs can be performed in different ways. First, there is the so-called direct coupling in the physical domain, second the coupling in the modal domain and third the coupling in the frequency domain [KRV08]. But there also exist coupling in the state-space domain [Sjo07]. Moreover, the coupling can be divided into coupling of interface displacements to interface displacements $\boldsymbol{q}_b^{(1)} \rightarrow \boldsymbol{q}_b^{(2)}$, coupling of interface forces to interface forces $\boldsymbol{g}_b^{(1)} \rightarrow \boldsymbol{g}_b^{(2)}$ or a mixed coupling $\boldsymbol{q}_b^{(1)} \rightarrow \boldsymbol{g}_b^{(2)}$ [Voo09]. These different assembly methods lead to primal and dual formulations of equations for the assembled system. The CB reduction used in this thesis, keeps the interface DoFs in the physical domain and leads to coupling of interface to interface displacements. This coupling method is presented in the following. More details about the other methods can be found in [[KRV08],[Voo09],[Val10] and [Sjo07]].

Direct coupling - coupling of interface displacements

As mentioned before, the direct coupling procedure requires that the interface DoFs are kept in the global domain. This can be true for full FE models, but as well for reduced models, for instance when considering a CB reduction. Figure 2.1 shows the coupling of two substructures using interface displcements. The general EoMs (Equation 2.1) are rewritten including interface forces $\boldsymbol{g}$ as

$$\boldsymbol{M}\ \ddot{\boldsymbol{q}} + \boldsymbol{V}\ \dot{\boldsymbol{q}} + \boldsymbol{K}\ \boldsymbol{q} = \boldsymbol{f} + \boldsymbol{g} \tag{2.65}$$

where the system matrices as well as displacement and force vectors of the whole assembly include the corresponding vectors and matrices of each substructure in block-diagonal form [KRV08].

$$\boldsymbol{M} = \begin{bmatrix} \boldsymbol{M}^1 & & \\ & \ddots & \\ & & \boldsymbol{M}^n \end{bmatrix} \qquad \boldsymbol{K} = \begin{bmatrix} \boldsymbol{K}^1 & & \\ & \ddots & \\ & & \boldsymbol{K}^n \end{bmatrix} \qquad \boldsymbol{V} = \begin{bmatrix} \boldsymbol{V}^1 & & \\ & \ddots & \\ & & \boldsymbol{V}^n \end{bmatrix} \tag{2.66}$$

$$\boldsymbol{q} = \begin{bmatrix} \boldsymbol{q}^1 & \cdots & \boldsymbol{q}^n \end{bmatrix}^T \qquad \boldsymbol{f} = \begin{bmatrix} \boldsymbol{f}^1 & \cdots & \boldsymbol{f}^n \end{bmatrix}^T \qquad \boldsymbol{g} = \begin{bmatrix} \boldsymbol{g}^1 & \cdots & \boldsymbol{g}^n \end{bmatrix}^T. \tag{2.67}$$

The assembly of n substructures has to satisfy the compatibility and the equilibrium condition. Mathematically, they are defined as

$$\boldsymbol{q}_b^{(a)} = \boldsymbol{q}_b^{(b)} \qquad \boldsymbol{S}\ \boldsymbol{q} = \boldsymbol{0} \tag{2.68}$$

$$\boldsymbol{g}_b^{(a)} + \boldsymbol{g}_b^{(b)} = \boldsymbol{0} \qquad \boldsymbol{L}^T\ \boldsymbol{g} = \boldsymbol{0} \tag{2.69}$$

where the substructures a and b are neighboring substructures. $\boldsymbol{S}$ and $\boldsymbol{L}$ are Boolean matrices identifying interface DoFs. If the DoFs of the coupled systems are matching, which means that the interface area is meshed identically, $\boldsymbol{S}$ is a signed Boolean matrix containing only 1, -1 and 0. $\boldsymbol{L}$ is a matrix containing only 1 and 0.

The Equations 2.65, 2.68 and 2.69 define the full coupled system.

In the primal formulation, as described in [KRV08], a unique set of interface DoFs $\overline{\boldsymbol{q}}$ is obtained, which holds

$$\boldsymbol{q} = \boldsymbol{L}\ \overline{\boldsymbol{q}}. \tag{2.70}$$

It satisfies Equation 2.68 for any $\bar{\boldsymbol{q}}$ as

$$\boldsymbol{S}\ \boldsymbol{q} = \boldsymbol{S}\ \boldsymbol{L}\ \overline{\boldsymbol{q}} = \boldsymbol{0} \qquad \forall \overline{\boldsymbol{q}} \tag{2.71}$$

which means that $\boldsymbol{S}$ and $\boldsymbol{L}$ are nullspaces of each other

$$\boldsymbol{L} = \mathrm{null}(\boldsymbol{S}) \qquad \boldsymbol{S}^T = \mathrm{null}(\boldsymbol{L}^T). \tag{2.72}$$

Due to this fact, the equation system for the coupled system can be rewritten as

$$\boldsymbol{M}\boldsymbol{L}\ \ddot{\boldsymbol{q}} + \boldsymbol{V}\boldsymbol{L}\ \dot{\boldsymbol{q}} + \boldsymbol{K}\boldsymbol{L}\ \boldsymbol{q} = \boldsymbol{f} + \boldsymbol{g} \tag{2.73}$$

$$\boldsymbol{L}^T\ \boldsymbol{g} = \boldsymbol{0} \tag{2.74}$$

By mutiplying Equation 2.73 with $\boldsymbol{L}^T$ from the left and substituting with Equation 2.70, the final equation for the primal assembled system can be expressed as

$$\overline{\boldsymbol{M}}\ \ddot{\overline{\boldsymbol{q}}} + \overline{\boldsymbol{V}}\ \dot{\overline{\boldsymbol{q}}} + \overline{\boldsymbol{K}}\ \overline{\boldsymbol{q}} = \overline{\boldsymbol{f}} \tag{2.75}$$

with

$$\overline{\boldsymbol{M}} = \boldsymbol{L}^T\boldsymbol{M}\boldsymbol{L} \qquad \overline{\boldsymbol{V}} = \boldsymbol{L}^T\boldsymbol{V}\boldsymbol{L} \tag{2.76}$$

$$\overline{\boldsymbol{K}} = \boldsymbol{L}^T\boldsymbol{K}\boldsymbol{L} \qquad \overline{\boldsymbol{f}} = \boldsymbol{L}^T\boldsymbol{f} \tag{2.77}$$

The applied CB reduction on the full system leads to the block diagonal matrices in Equation 2.65 including the CB matrices defined in Equation 2.63 of each substructure.

3 Method

This chapter describes the work that was accomplished to fulfill the aim of this thesis, described in Section 1.2. Overall, the project was divided into three main phases: pretest, test and posttest phase. Each phase involved EMA as well as CAE related challenges, which means that the simulation and the experiment were carried out in parallel.

3.1 Software

The pre- and postprocessing as well as the solving itself were performed with Ansa for pre-, Altair Hyperview for postprocessing and MSC Nastran for solving the modal analysis, i.e the SOL103. Furthermore Matlab R2015b and its System Identification toolbox, as well as the open-source FEMCali toolbox using the N4SID method [MAL96] were used for analyzing measurement data, estimating mathematical models and updating of FEA towards EMA results.

3.2 Models

Two different types of models were used in this thesis. FE models, i.e. analytical models and experimental models, which are the test specimen from the vibration experiments. Three FE models were obtained from VCC: a calibrated rear subframe, a nominal rear subframe and a model of the BIW. The test specimen included the BIW and two rear subframes (in the following named subfame).

3.2.1 Model adjustments

This section presents the adjustments on both, the FE model and the corresponding test specimen of the BIW, which were required before the EMA was accomplished. Overall, the adjustments had to ensure conformity of the FE model and the test specimen.

The automotive industry defines assemblies related to the included parts. The car body for instance is part of the assemblies named body in grey (BIG), body in blue (BIB) and body in white (BIW). These three groups can be considered as variations of each other. The main differences are: a BIB is the main car body including doors, windshield and other windows, a BIG does not include the doors and a BIW is the car body including neither doors, trunk lid, windshield and other windows. The BIW is the one of interest in this thesis.

Brackets, affected by the local modes in the frequency range between 30 Hz and 300 Hz, as this is the frequency range of interest, were removed from the FE model as well as from the test specimen.

3.2.2 Finite element model of the BIW

The final FE model (after adjustments) of the BIW contained more than two million number of elements and nodes. SOLID elements in combination with RBE3 elements represent spot welds and glued connections. Panels, brackets and the main structure are modelled with SHELL elements on the midsurfaces and an assigned thickness. Connections are modelled according to the Volvo guide lines with RBE2 elements and the corresponding bolt/screw as CBAR element. Since the obtained test specimen is painted and includes sprayable damping, the corresponding masses were added via non structural mass (NSM) cards to the affected properties.

In total, the FE model includes over 10 million DoFs and a total mass of 427 kg, including 11.7 kg of the NSM. Figure 3.1 shows the FE model of the BIW used for all CAE analyses.

3.3 Experimental modal analysis

This section summarizes the realization of the EMA, including the pretest and test phase. The test setup, technical data of the measurement equipment as well as the realization of the EMA itself are presented. An

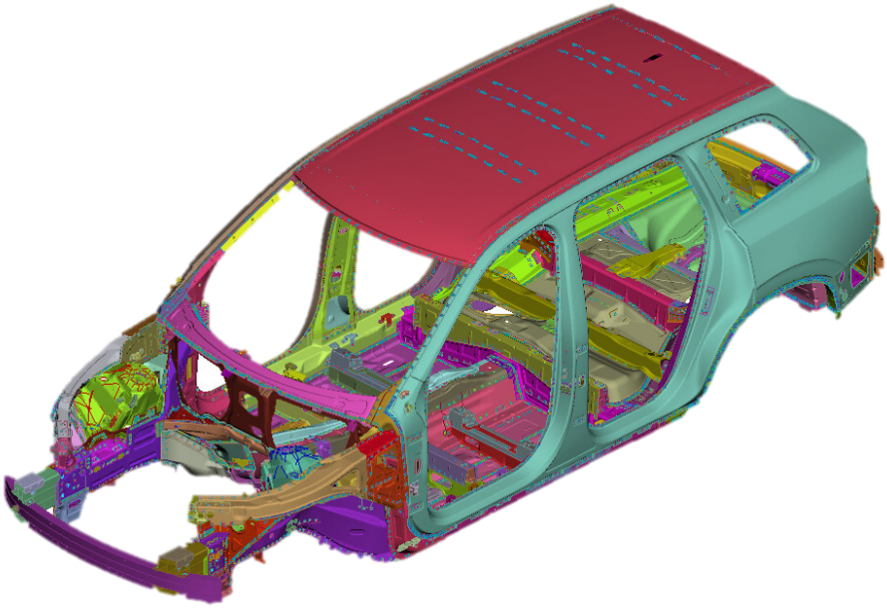

Figure 3.1: *FE model of the BIW in the isometric view. The different colors denote different properties.*

EMA was done for the BIW alone and for two assemblies, the coupling of the BIW with subframe 112 and subframe 220.

3.3.1 Evaluation of sensor positions

On the basis of EfI (Section 2.2.1), the final accelerometers were positioned. The positioning was performed on a candidate DoF set (DoF_c) obtained from Volvo. These candidate positions were included in the provided FE model, and correspond to the typical positions that are used in EMAs at Volvo on a BIG. Volvo uses triaxial sensors at 90 positions, which means that 270 DoFs are measured. During this project, 26 uniaxial accelerometers were availaible. Thus the candidate DoF_c were reduced to 26 final DoFs (DoF_f). The reduction to DoF_f was done considering the first eight eigenmodes of the BIW only. The eigenmodes correspond to global modes since at higher frequency, local roof modes would cause problems in finding a proper sensor placement with a low amount of accelerometers. Nevertheless, to still measure a response of the roof, the EfI was applied for 23 DoFs only and the remaining three sensors were manually placed on the roof, i.e. the beams at the roof.

Apart from the EfI, the cross-correlation, i.e. the separation of eigenmodes should be considered when picking sensor positions. In previous studies [Sch+04], the AutoMAC is suggested to analyze the cross-correlation and replace positions if a high cross-correlation occurs. Therefore, the AutoMAC was evaluated for the EfI obtained positions DoF_f and the positions were replaced accordingly. The evaluation of DoF_f can be summarized as follows:

1. Modal analysis of the FE model for the BIW, to obtain the eigenvectors of the candidate DoFs DoF_c.
   (a) Each chosen position requires a local coordinate system, for uniaxial accelerometers with one axis (z-axis) orientated out-of-plane.
2. Solve the AutoMAC, Equation 2.32, of DoF_c to assess the available DoFs if necessary.
3. Apply the EfI, see Section 2.2.1, to obtain DoF_f.
4. Solve the AutoMAC, Equation 2.32, of DoF_f and replace DoFs with a high cross-correlation.
5. Define the actuator positions, i.e. check if possible actuator positions are included in DoF_f and if not, replace DoFs to include actuator DoFs.

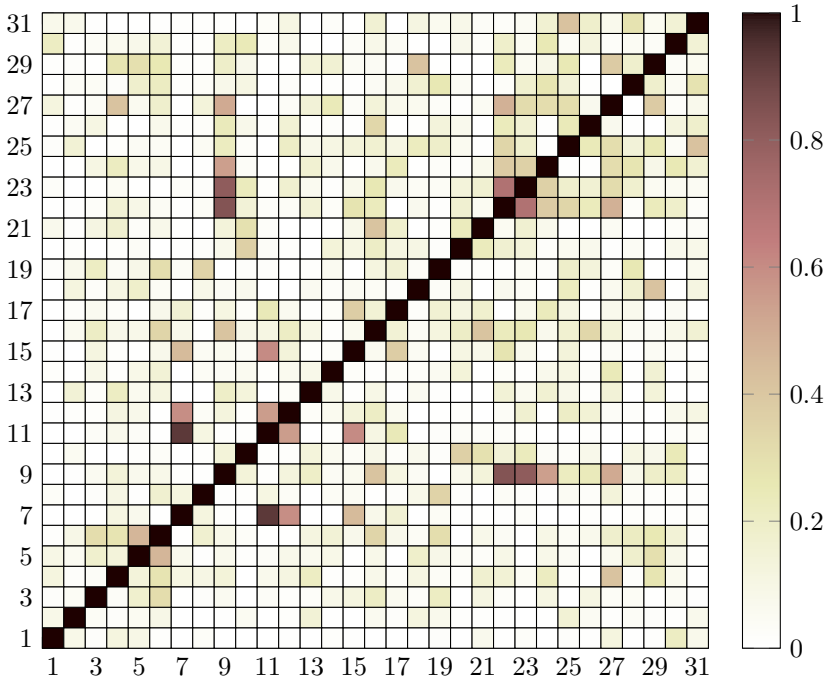

Figure 3.2: *AutoMAC of the final sensor set of the BIW for the first 31 flexible modes.*

6. Solve the AutoMAC of the modified set DoF_f and thus assess the final sensor positions.

The chosen actuator positions have to enable excitation of all mode shapes in the frequency range of interest [Sch+04]. If a single position is not sufficient to excite all modes, multiple positions have to be excited. This thesis focused on the global modes, which can all be excited from one position. This position is similar to one of the positions used in [Sch+04]. Figure 3.3 and 3.4 show the final accelerometer positions DoF_f. The transformation of the sensor coordinates for sensors obtained by the FEA were done with the use of common measuring equipment: angle meters, calipers, compasses, etc. The equipment was used to position the sensors as accurate as possible. Figure 3.2 shows the AutoMAC of the final accelerometer positions DoF_f. Some cross-correlation is visible, but the eight global modes (mode 1 to 8) are clearly separated. Cross-correlation occurs in the local modes only.

Sensor positions in the assembly

In the second part of the thesis, EMAs were performed in the assembled setup, in which a subframe is attached to the BIW. To obtain information about the coupled subframes, 10 triaxial sensors, i.e 30 DoFs, were mounted on the subframes. The positions are equal for both subframes 112 and 220. The 10 positions were taken from the set used in [GA17]. The main requirements for the selection of the sensor positions were the accessibility of the position in the assembly and that the positions were part of the calibration set of both subframes (Section 3.5.1). Thus, the chosen sensors belong to the ones, which give a good fit between the mathematical model and the raw measured data. The chosen positions on the subframes are shown in Figure 3.5.

3.3.2 Test setup and process

As mentioned in [Tec], the common boundary conditions for EMAs are either the free-free support or the fixed support. These two conditions are able to completely suppress the RBMs or at least clearly separate the modes from the first flexible mode shape. In this thesis, the EMA was carried out with the free-free support. This was implemented by lifting the BIW with a hydraulic crane and by using long lightweight high-strength lines, which are shown in Figure 3.6(a). For the mounting, four hooks were attached to the roof of the BIW. In total, three different types of accelerometers were used in the EMAs: Uniaxial PCB Piezotronic type 352C22/NC, uniaxial PCB Piezotronic type 352A24/NC and triaxial PCB Piezotronic type 356A03. The former weigh 0.5 gram each, the second and third weigh 0.8 and 1.0 gram, respectively. The corresponding type of accelerometers

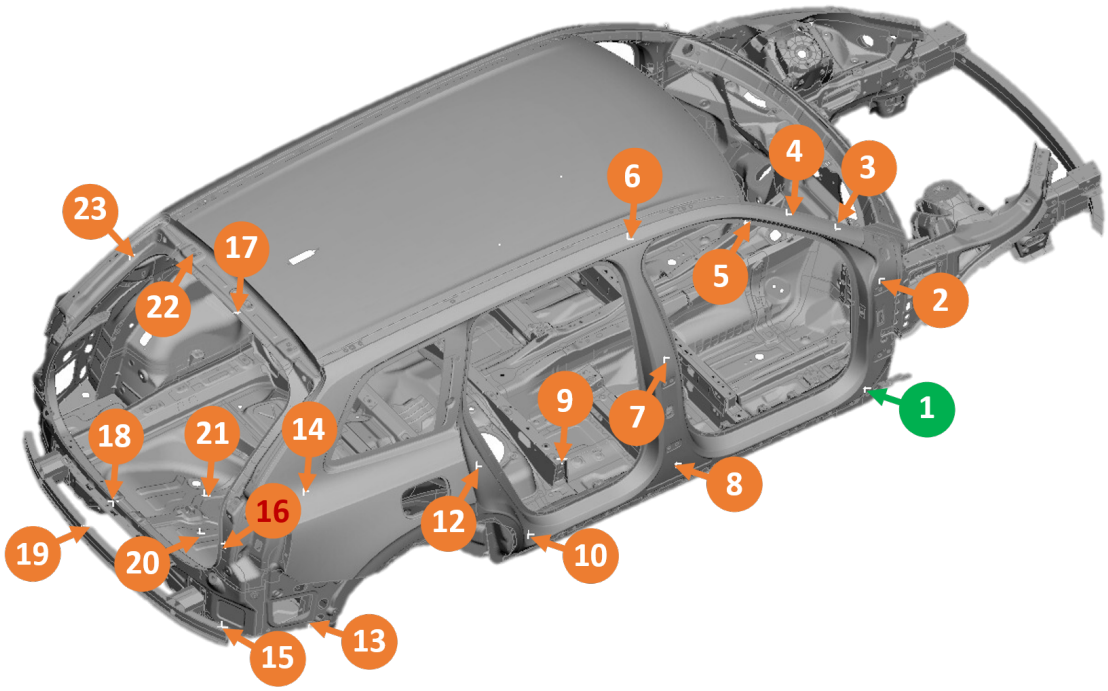

Figure 3.3: *Accelerometer locations on the right side of the BIW and the trunk area. Red numbered position denotes the sensor, which is placed on the opposite side of the actuator. Orange positions are the uniaxial accelerometers of type 352C22/NC, green denotes the uniaxial type 352A24/NC.*

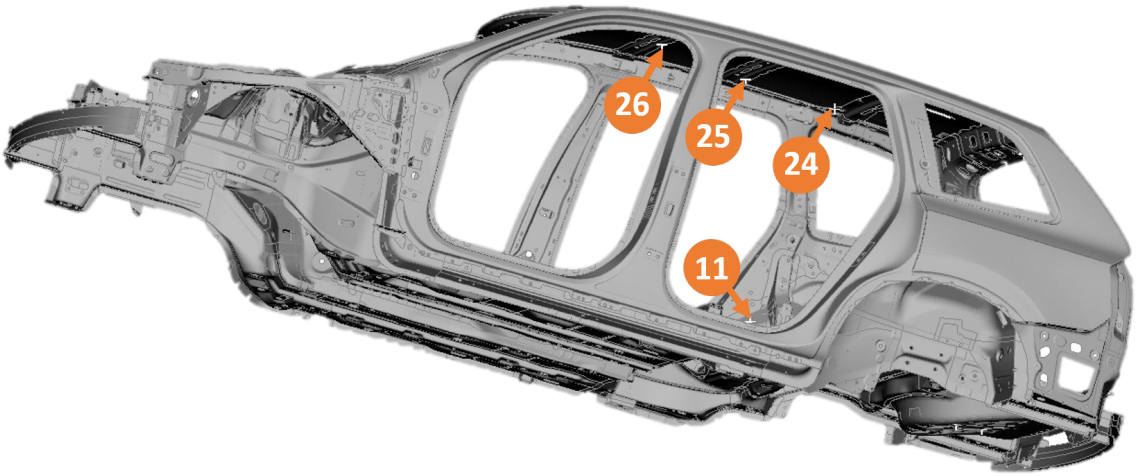

Figure 3.4: *Accelerometer positions at the roof beams and inside the BIW.*

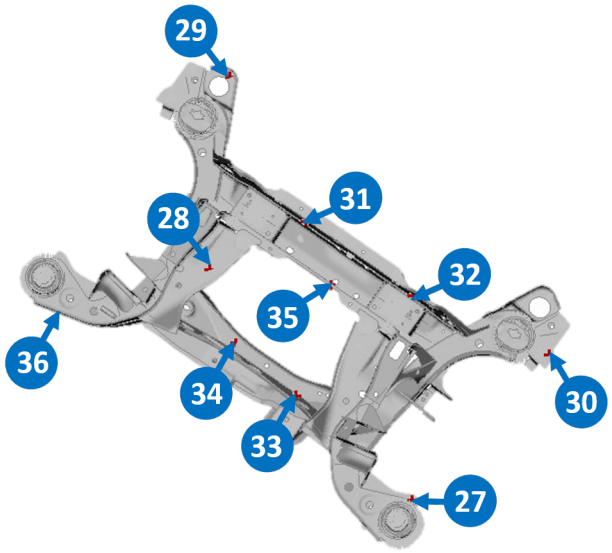

Figure 3.5: *Positions of the 10 triaxial accelerometers on the subframe in the coupling analysis of BIW and the two subframes.*

at the positions are shown in Figure 3.3 to 3.5. The shaker was a Ling Dynamic System make and of type 207 (maximum amplitude 7.0 N) with a metallic stinger approximately 7.0 mm in length and a load cell attached between BIW and shaker, from Brüel&Kjaer type 8203 with an IEPE converter 2647B. All uniaxial accelerometers were mounted with the aid of synthetic wax to the structure. The triaxial sensors were glued. The load cell was attached with a stinger attachment plate, adding 0.2 gram to the setup. In the EMA of the assembly, the subframes 112 and 220 were attached with four M14x110 bolts made of steel, including a 3.0 mm thick washer. The four bolts were fixed with a locking torque of 50 kNm for both assemblies. Each bolt has a weight of 161.0 gram. The EMAs of both models, the BIW alone and the assembly, were excited by a multisine. The used multisine excites the structure isochronic with sinusoidal signals at multiple frequencies. The frequencies are taken from a defined measurement range and the number of frequency lines defines how many sets are taken to cover the range. Two frequency ranges were considered. In the first measurement, 2000 frequency lines in a range between 20 Hz and 300 Hz were recorded. In the second measurement, the frequency range was reduced to 30 Hz to 100 Hz to resolve the frequency range of the eight global modes in greater detail. The amplitude of the excitation was 1.3 N in the measurements of the BIW alone and 1.8 N in the measurements of the assembly. The amplitudes were estimated by fast chirp tests to avoid a non-linear response of the structure on the one hand and to determine the influence of the support of the shaker on the other hand. The measurements had to show an independence of the support of the shaker. Figure 3.6 and 3.7 show the setup for the EMA on the BIW. Figure 3.8 illustrates the setup of the assembly. With respect to of the assembly setup, the original setup of the BIW was modified by mounting 10 additional triaxial accelerometers onto the subframe. Thus, the shaker attachment as well as the free-free boundary condition and the 26 sensors at the BIW were still valid for the EMAs of the assemblies.

3.4 System identification of measurement data

The system identification of measurement data, i.e. frequency domain input-output data, evaluates mathematical models that cover the test data [Mata]. The obtained models are of first order, i.e. state-space models, described by the matrices $\boldsymbol{A}$, $\boldsymbol{B}$, $\boldsymbol{C}$ and $\boldsymbol{D}$, c.f. Section 2.1.2. In this thesis, state-space models were evaluated with the N4SID method, which is described in detail in [MAL96]. Generally, state-space models are polynomial approximations and require a proper model order. A proper model order is exactly twice the amount of expected modes in a certain frequency range, since eigenvalues always occur in complex conjugated pairs. A too high model order can be compensated by a modal reduction of states, in which states with a low input-output importance are removed. The mathematical model of the measured data forms the basis for further analyses. Thus, high resolution approximation is required to obtain accurate results. During this project, different steps

(a) (b)

Figure 3.6: *Test setup for the EMA of the BIW. (a) Free-free support of the BIW showing the lightweight high-strength lines. (b) shaker attachment of the BIW at sensor location 16.*

(a) (b)

Figure 3.7: *Mounted accelerometers of Dof_f, (a) shows sensors on the side of the BIW. (b) sensors in the trunk area.*

(a) (b)

Figure 3.8: *The assembled rear subframe on the BIW. (a) Attached rear subframe on the BIW from the side. (b) attached rear subframe on the BIW from below. Some of the triaxial sensors as well as one of the four M14x110 bolts including the washer is shown in (b).*

were performed, to obtain proper state-space models. These are further explained below. Overall, state-space models were created for the measurement data of the BIW alone, subframe 112 alone and the assembly of the BIW and with the two subframes 112 and 220.

3.4.1 Improvement techniques for state-space models

One challenge to obtain a good state-space model was related to the resolution of the measured FRFs, i.e. differences in certain channels (sensors). The measured reponses of a complex structure often do not coincide in all channels. In many cases, not all modes are clearly visible in all channels. The consideration of all channels for the state-space model estimation resulted in a poor fit between FRFs and state-space model.
This is obvious, since the frequencies for detected modes can not be separated. An estimation of a state-space model when considering only a subset of channels, i.e. the channels which seperate clearly all expected modes, led to a much better fit between FRFs and state-space model. Afterwards the FRFs in the remaining channles are accounted for the state-space model by a re-estimation of the state-space matrices $\boldsymbol{B}$, $\boldsymbol{C}$ and $\boldsymbol{D}$. This means that the state-space matrices are optimized by a linear least-squares fitting which is a linear regression to improve the accuracy. Beside from including poorer channels, the re-estimation was used in this project to merge stepwise evaluated state-space models.

Apart from the partition of channels, an inflation of several measurement sets can also improve the mathematical model. This could either be different kind of data, such as a mix of chirp and multisine data, or subranges with higher resolution (more frequency lines) in a specific frequency range. The former was done in case of the subframe 112 (and also 220 in [GA17]) and the latter for the state-space model of the BIW, where measurements with a higer resolution were considered in the range between 30 Hz and 100 Hz. If a large frequency range is considered, it is suggested to stepwise estimate the mathematical models. The models of each section are merged to one large state-space model, which descibes the FRF of the complete range.

Another step is the manual addition of a high and a low pole out of the frequency range of interest. This helps to capture the behavior at the bounds of a frequency range. A pole around zero increased the fit in the range around the RBMs. A high frequency pole improved the fit close to the upper bound.

3.4.2 Mathematical model of the BIW

A check of the FRFs of all 26 channels highlighted a couple of channels that clearly separated 10 modes in a frequency range between 20 Hz and 65 Hz, whereby other channels separated only up to 9 modes. Thus, the channels, that separated 10 modes, were used for the estimation of the state-space model and the remaining ones were included by the re-estimation. In total, 13 out of 26 channels were later included in this range. A model order of 20 was chosen and two poles, one around 0 Hz and another one around 70 Hz were added manually. In total, a state-space model up to 170 Hz was established by splitting the raw data into seven subranges. The range of 20 Hz to 65 Hz is the first subrange. All seven subranges were evaluated by a subset of channels. Afterwards two poles were inflated and a re-estimation of the state-space matrices $\boldsymbol{B}$, $\boldsymbol{C}$ and $\boldsymbol{D}$ with 15 iterations was conducted. At the end, all 7 submodels were merged to one model describing the behavior

Table 3.1: Estimation of the mathematical model for the BIW and the two assemblies A_{112} and A_{220}. Shown are the considered subranges, the frequencies of inflated poles and the model order per subrange.

# subrange	f_{min} [Hz]	f_{max} [Hz]	lower pole [Hz]	upper pole [Hz]	model order BIW	model order assemblies
1	30.00	65.00	1.00	67.8	20	18
2	65.00	87.00	62.00	92.25	24	18
3	87.00	100.00	85.00	105.00	20	20
4	100.00	125.00	92.00	155.00	28	24
5	125.00	140.00	117.00	170.00	24	20
6	140.00	154.00	138.00	170.00	16	16
7	154.00	170.00	138.00	179.00	20	20
full	**30**	**170.00**			**152**	**136**

between 20 Hz and 170 Hz. An overview of the subranges, i.e. the inflated poles, model orders and frequency boundaries, is shown in Table 3.1.

3.4.3 Mathematical model of the subframe 112

As later shown in Section 3.5, a state-space model of the experimental data as well as the FE model is required in the calibration procedure. All FE related steps are automatically done in the FEMcali toolbox. For the experimental data, two state-space models, one for the mass loaded configuration and one for the configuration without mass loading were established. Approximately 20 modes were found in the triaxial channels in the mass loaded configuration [GA17]. Thus, a model order of 40 was considered effective. Two poles, one around zero and one above 225 Hz were manually added to capture the influence at the bounds of the frequency range more precisely. The state-space model was based on the 24 triaxial channels only, since the uniaxial sensors did not capture the local bushing modes. The state-space model was accounted for all 56 channels, including addition of chirp data for the low frequency range below 40 Hz and a re-estimation with 15 iterations of the state-space matrices $\boldsymbol{B}$, $\boldsymbol{C}$ and $\boldsymbol{D}$.

The FRFs for the configuration without mass loading showed approximately 10 modes in the frequency range between 60 Hz and 350 Hz. Thus a model order of 20 was applied. Used were the FRFs later up to 265 Hz. This range includes 8 of the 10 modes. Again, two poles were added manually. In this configuration, all channels were directly used to evaluate a proper mathematical model. Chirp data was also added for the low frequency region below 60 Hz and the state-space matrices $\boldsymbol{B}$, $\boldsymbol{C}$ and $\boldsymbol{D}$ were re-estimated.

3.4.4 Mathematical models of the assemblies

An EMA was performed for two assemblies, A_{112} and A_{220}, which denote the assembly of the BIW with subframe 112 and 220, respectively. State-space models were evaluated for a freqeuncy range between 30 Hz and 170 Hz. The high amount of occuring modes, i.e. 68 eigenmodes, were handled by dividing the FRFs in 7 sections as shown in Table 3.1. For each section, the state-space model was estimated with a proper model order for a subset of channels. It was followed by accounting for the remaining channels adding a set of a high and low pole. As usual, the state-space matrices $\boldsymbol{B}$, $\boldsymbol{C}$ and $\boldsymbol{D}$ were re-estimated with 15 iterations. For each state-space model, the eigenvalue problem was solved separately to obtain the eigenfrequencies and mode shapes. All eigenvectors, eigenfrequencies and corresponding FRFs of the 7 state-space models were finally merged to one model, that describes the behavior between 30 Hz and 170 Hz. Since the raw measurement data for both assemblies were similar, the mathematical model was estimated for both in the same way.

3.5 Calibration of the subframe

In this section, the FE model of a subframe is calibrated against measurement data. The vibration measurements were performed in another project [GA17]. Additionally, a calibration of a subframe (subframe 220) is presented

in [GA17]. Thus, with the calibration performed in this thesis, two calibrated FE models for the suframes exist in total. These two models were used in the assembly with the BIW (c.f. Section 4.3) to analyze the influence of variation in nominally indentical components in an assembly.

Two measurement sets were available in the calibration procedure. The data sets correspond to two subframes (subframe 111 and 112), which are nominally identical to subframe 220. To cover the largest spread, the measured responses of subframe 111 and 112 were compared to 220. The most diverging one was used in the calibration procedure. To define the differences, three different analyses were considered, i.e. the fit according to the normalized root mean square error (NRMSE) of the full raw test data sets, the differences in the resulting eignfrequencies Δ and the MAC correlation with respect to Equation 2.31 from the corresponding state-space models of the three subframes. Thus, state-space models were created according to Section 3.4. The NRMSE is defined as [Matb]

$$\text{NRMSE} = 1 - \frac{||\boldsymbol{x}_{ref} - \boldsymbol{x}||}{||\boldsymbol{x}_{ref} - \text{mean}(\boldsymbol{x}_{ref})||} \tag{3.1}$$

and bounded by -∞ $\leq$NRMSE$\leq$ 1, where 1 denotes a perfect fit and -∞ an inadequate fit. The vector $\boldsymbol{x}$ denotes the data used for the error estimation, which is the response $\boldsymbol{H}^X(\omega_i)$ of subframe 111 and 112. The vector $\boldsymbol{x}_{ref}$=$\boldsymbol{H}^X(\omega_i)$ is the response of subframe 220. The test data without additional mass loading were used in a frequency range between 20 Hz and 290 Hz, which corresponds to the first eight eigenmodes. The details are shown in [GA17]. Figure 3.9 shows the MAC analysis of subframe 220 with 111 and 112, respectively. Table 3.2 summarizes the resulting eigenfrequencies f_i for the eight eigenmodes, where f=$\omega/(2\pi)$. In addition, the NRMSE is shown. The MAC correlation in Figure 3.9 shows three uncorrelated (MAC<0.1) for both subframes and two well correlated (MAC>0.9) modes. All three analyses identify subframe 112 as the most different one compared to 220. Therefore, subrame 112 is used in the calibration procedure. More details about the measurement, setup, technical data of sensors and actuators, can be found in [GA17].

The calibration of subframe 112 followed the physics described in Section 2.4 with the use of Matlab and the toolbox FEMcali. The calibration was done in two steps and covers the freqeuncy range 20 Hz to 265 Hz. First, the mass loaded configuration was calibrated in the frequency range between 40 Hz and 225 Hz [GA17] to obtain four bushing parameters. These are shown in Figure 3.10. In a second step, the FE model of the configuration without mass loading was updated in a frequency range between 20 Hz and 265 Hz, which correspondes to the first eight eigenmodes of the subframe. The previously obtained bushing parameters were thereby fixed.

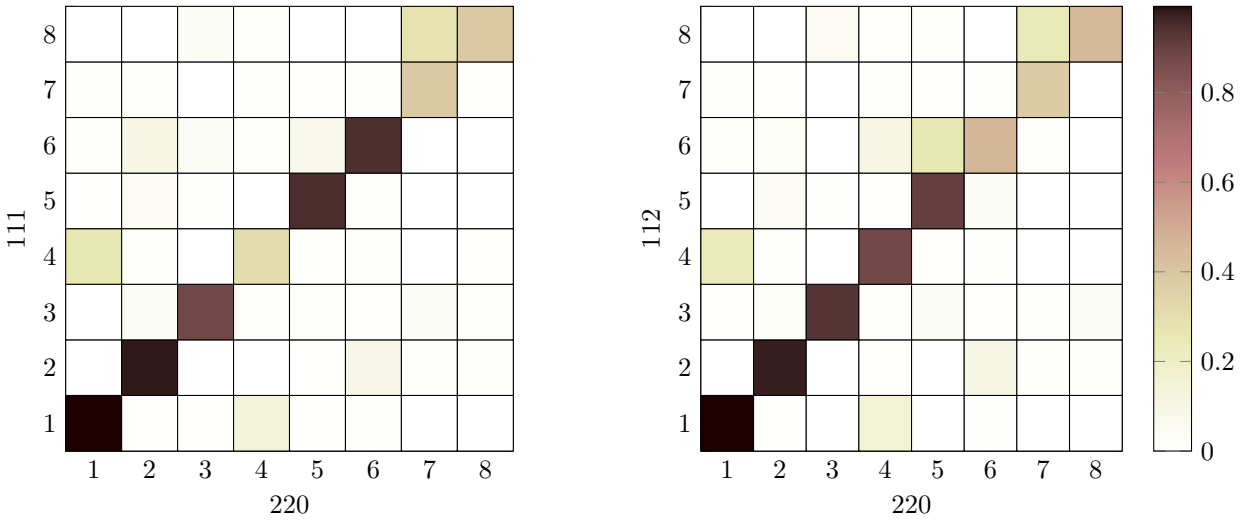

Figure 3.9: *MAC correlation analysis of the evaluated state-space models for the first eight structural modes of the rear subframe. (a) shows the MAC of the model obtained from data set 220 and 111 and (b) from the data sets 220 and 112.*

Table 3.2: The first eieght flexible modes of the measured response of the subframes 220, 111 and 112. The NRMSE is estimated with respect to Equation 3.1. The deviation of f_{111} and f_{112} to f_{220} [%] is denoted by Δ_{111} and Δ_{112}, respectively.

Mode	f_{220} [Hz]	f_{111} [Hz]	Δ_{111}[%]	f_{112} [Hz]	Δ_{112}[%]
1	76.8	75.9	1.11	75.8	1.24
2	160.5	155.8	2.97	153.4	4.61
3	193.0	191.8	0.65	191.3	0.89
4	195.2	194.2	0.51	193.7	0.78
5	204.9	204.1	0.37	203.7	0.56
6	210.8	207.0	1.80	205.4	2.62
7	240.9	240.1	0.32	238.7	0.90
8	253.9	252.7	0.45	252.3	0.62
NRMSE		0.73		0.32	

3.5.1 Set definition

A leave-out validation of the calibrated FE model requires a set of sensors that are not used in the calibration procedure. Thus, sets for calibration and validation were defined before the calibration procedure started. In the mass loaded configuration, the channels of the state-space model, which fit ≥97% to the raw test data according to the NRMSE in Equation 3.1 were taken as calibration sensors, the remaining ones were used as validation sensors. In the configuration without mass loading, the sensor that fit ≥87% were taken for calibration and the remaining ones for validation. The corresponding channels of the four sets are listed below. The subscript *ml* denotes the mass loaded configuration. The numbering of the sensors correspond to the positions shown in Figure 3.3 to 3.5.

- calib_{ml}=[1x, 1z, 2x, 2z, 3x, 3z, 4x, 4z, 5x, 5y, 5z, 6x, 6y, 6z, 7x, 7z, 8x, 8z, 9x, 10x, 16, 20, 21, 22, 25, 26, 27, 28, 29, 31, 32, 35, 36]
- valid_{ml}=[1y, 2y, 3y, 4y, 7y, 8y, 9y, 9z, 10y, 10z, 11, 12, 13, 14, 15, 17, 18, 19, 23, 24, 30, 33, 34]
- calib=[1x, 1y, 1z, 2x, 2y, 2z, 3x, 3y, 3z, 4x, 4y, 4z, 5y, 5z, 6x, 6y, 6z, 7y, 7z, 8z, 9x, 10x, 11, 12, 13, 14, 15, 16, 17, 18, 19, 20, 22, 23, 25, 26, 27, 29, 30, 31, 32, 33, 35, 36]
- valid=[5x, 7x, 8x, 8y, 9y, 9z, 10y, 10z, 21, 24, 28, 34]

3.5.2 The calibration parameters

Figure 3.10 shows the parameters, which were updated in the calibration procedure for subframe 112. In total, 7 stiffness parameters were updated. As mentioned before, the 4 rubber bushing stiffnesses were determined in the configuration with mass loading and the additonal three parameters, i.e. three Young's moduli of steel parts were updated in the configuration without mass loading. Tested were much more than the 7 parameters shown in Figure 3.10. Nevertheless, only these 7 parameters showed suitable results for the identifiability, for the parameter statistics shown in Section 4.2 as well as fixing of mode switches. The four thickness parameters t_a to t_d differ between the mass loaded configuration (1.20 mm) and the configuration without mass loading (1.40 mm) but they are not updated in the calibration procedure.

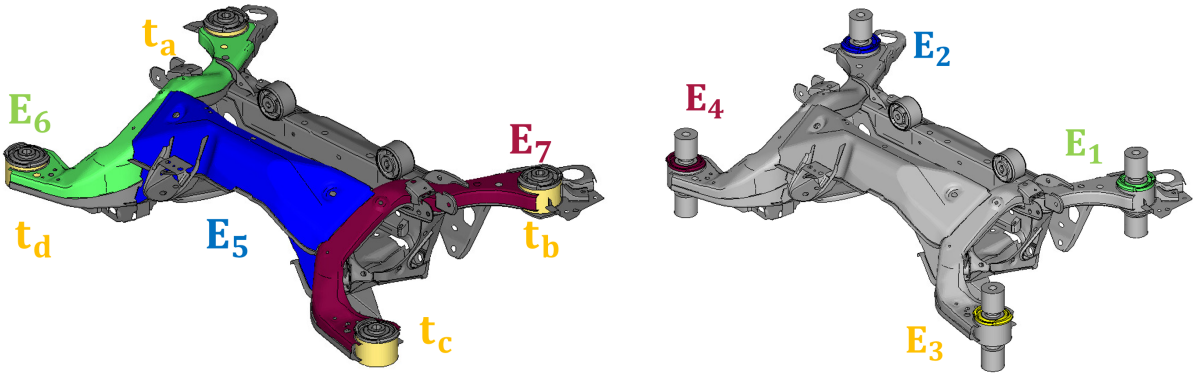

(a) (b)

Figure 3.10: *Updated parameters in the calibration procedure. (a) Parameters in the configuration without mass loading. (b) Young's moduli of the rubber bushings obtained in the mass loaded configuration. E denotes a stiffness and t a thickness parameter.*

.

4 Results

4.1 Results of the BIW

The analysis on the BIW alone, i.e. the correlation between FEA and EMA is presented in this chapter. As mentioned before, the mathematical model of the EMA covers a frequency range between 20 Hz and 65 Hz in higher resolution and in lower resolution up to 170 Hz. The focus of the correlation is on the 8 global mode shapes, which occur at frequencies below 60 Hz. Figure 4.1 shows the first 9 eigenmodes of the BIW. Red colored areas denote areas which are higly affected in the corresponding mode shape, whereby blue areas are almost not affected. For a better visibility of the mode shapes, a deformation factor of 20 is applied in the figure. The counting of the modes starts with 1 in the FEA for the first global mode. This means that the RBMs are not presented here. Figure 4.1(i) shows the first local mode that mainly affects the roof of the BIW. Table 4.1 compares the results from the EMA and the FEA. It presents the eigenfrequencies for all 10 modes between 20 Hz and 65 Hz of the EMA as well as the corresponding FE results. Furthermore, the differences between the two models are listed and the MAC number, evaluated according to Equation 2.31 is shown. One difference is that the FEA computes 15 eigenmodes (modes are shown in Appendix A) below 65 Hz and the EMA determines only 10 modes. As already mentioned in Section 2.2.1, the main aim is, due to a low amount of sensors, to capture the 8 global modes of the BIW for which the sensor positions were mainly evaluated.

Figure 4.2(a) shows the sum over all FRFs of the raw test data and the state-space model of the BIW between 30 Hz and 170 Hz. The state-space model shows a good representation of the measured test data. The fit of

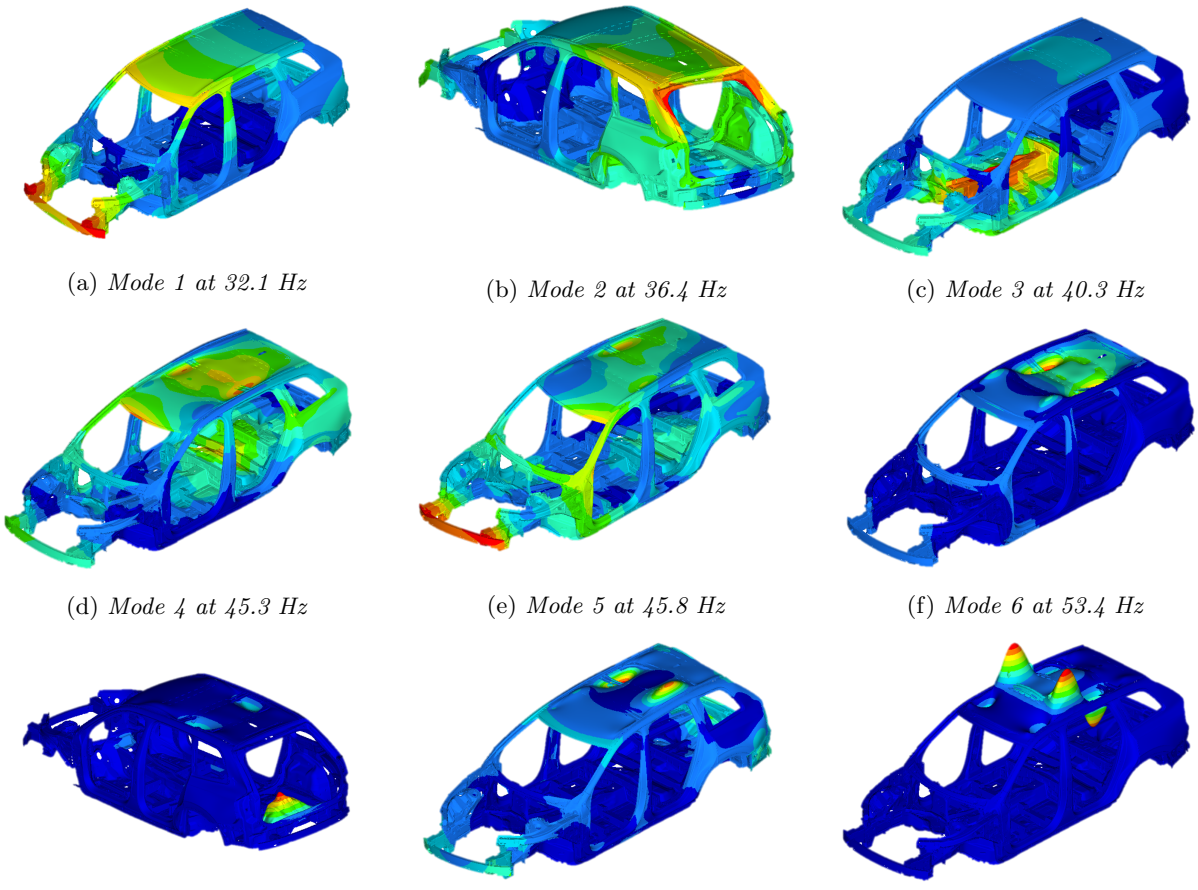

(a) *Mode 1 at 32.1 Hz* (b) *Mode 2 at 36.4 Hz* (c) *Mode 3 at 40.3 Hz*

(d) *Mode 4 at 45.3 Hz* (e) *Mode 5 at 45.8 Hz* (f) *Mode 6 at 53.4 Hz*

(g) *Mode 7 at 57.7 Hz* (h) *Mode 8 at 58.7 Hz* (i) *Mode 9 at 59.7 Hz*

Figure 4.1: *The first 9 flexible eigenmodes of the BIW. (a) to (h) denote the global mode shapes and (i) shows local effects on the roof.*

Table 4.1: Results of the modal analyses on the BIW. Subscript EMA denotes experimentally obtained results and FE denotes results obtained from the FEA. Shown are the resulting frequencies f in Hz, their relative difference Δf in % and the MAC number. Fitted are the modes of the FE model to the EMA, that showed the highest MAC number. A MAC, which denotes a high fit, i.e. MAC>0.9) is highlighted by bold numbers.

#mode EMA	#mode FE	f_{EMA} [Hz]	f_{FE} [Hz]	Δf_{EMA} [%]	MAC
1	1	35.0	32.1	8.4	**0.92**
2	2	39.1	36.4	6.8	**0.94**
3	6	43.7	53.5	-22.3	0.73
4	4	46.1	45.3	1.6	0.82
5	5	50.0	45.8	8.4	0.35
6	9	52.7	59.7	-13.3	0.85
7	7	57.2	57.7	-0.9	**0.98**
8	12	59.9	61.9	-3.4	0.49
9	8	62.2	58.7	5.6	0.77
10	9	64.5	59.7	7.4	0.48

the sum over all FRFs with respect to the NRMSE (Equation 3.1) is 0.963. Figure 4.2(b) shows the FRF measured at sensor 14, which correspond to the sensor with the highest fit between measured data and identified state-space model. However, a comparison between FEA and EMA indicates almost no match. As shown in Figure 4.3 for channel 15. It is visible, that the resonances are partly similar below 60 Hz. The difference is mainly a shift in frequency. Nevertheless, the two FRFs diverge completely for frequencies above 60 Hz. The NRMSE between FEA and EMA results in $-1.397 \cdot 10^3$, which denotes a very poor fit.

As mentioned in Section 2.3.1, modes with MAC values above 0.9 are considered as well-correlated. Thus, the EMA modes 1, 2 and 7 correlate well to the FE model. Mode 1 and 2 show a difference in the eigenfrequencies of up to 8.4% between FEA and EMA. This indicates a too low stiffness of the FE model to represent these two modes. Mode 7 does not show a significant difference in the eigenfrequencies. Furthermore, mode 7 shows a high cross-correlation (MAC=0.98) to mode 11, which can be found in Appendix A. Generally, cross-correlation should be avoided as mentioned in Section 3.3.1. Since the focus in this analysis is on the global modes the cross-correlation to mode 11, which is a local mode, was accepted in the sensor placement. The AutoMAC in Figure 3.2 predicted this correlation. Thus, this cross-correlation can be used as an additional validation criterion, which means that the experimental and FE model are coincide in their resulting mode shapes for mode 7 and mode 11.

Usually, it is preferable that the high MAC values result in the diagonal, i.e. the same order of the modes, do define a high correlation between the experimental and FE model. The diagonal trend can be seen in Figure 4.4 for the four first modes of both models as well as mode 7, mode 9 (8) and 10 (9). Mode 3 of the EMA also shows a significant correlation to mode 6 of the FEA. Mode 5 and 8 of the EMA do not show any correlation to an FE mode. Mode 6 of the EMA indicates a correlation to mode 9 of the FEA. It should be mentioned that a modal reduction on the EMA results, i.e. a suppression of the EMA mode 8, would improve the diagonal trend in the MAC. However, Figure 4.2 shows that some EMA channels show a mode at this frequency around 60 Hz. Thus a modal reduction would not represent the complete results of the EMA.

Conclusively, the fit between the FEA and EMA is unsatisfactory. Only three modes can be identified with a high correlation. Different input positions for the actuation did not result in other mode shapes for the EMA. Thus, it is assumed that the received FE model of the BIW do not represent the test setup situation sufficiently. The main differences is presumably the reduction of the BIW model from a BIG model. If the reduction is not fully correct, i.e. the FE model includes still parts that do not belong to a BIW or parts that do belong to a BIW are removed. This can effect the results significantly. Furthermore, the FE model was created with differences in modelling techniques for spot welds. These do not influence analyses on a BIG, but probably on a BIW, because the BIG includes much more parts with a stiffening influence of the whole structure. Thus, the FEA and EMA are treated separately in all further analyses only compared qualitatively.

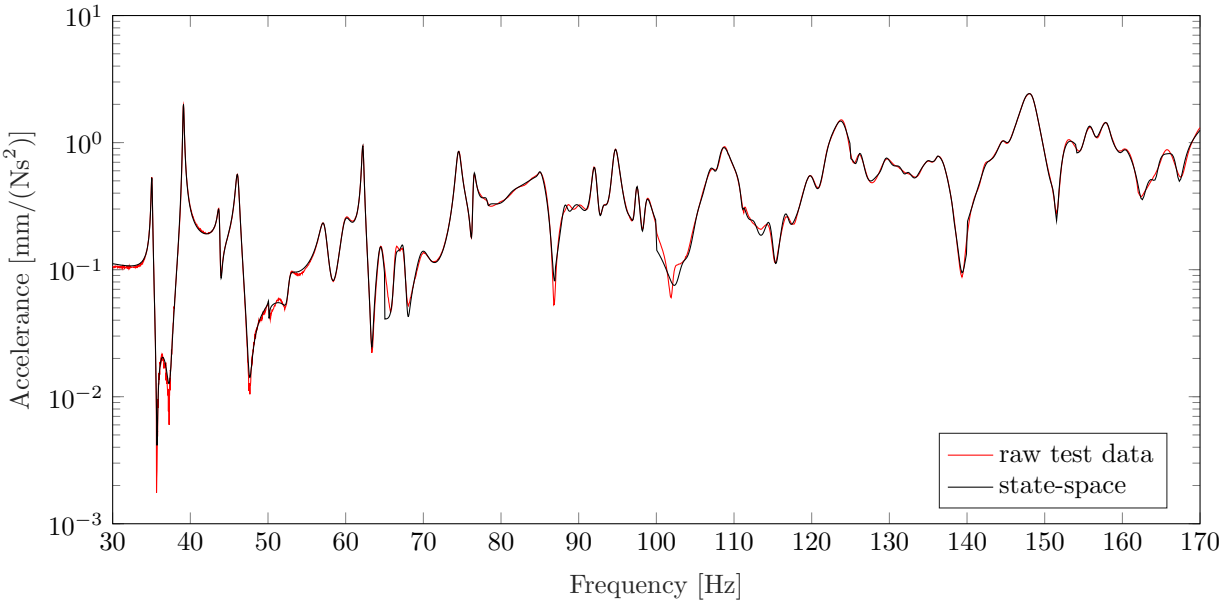

(a) *Sum over all FRFs*

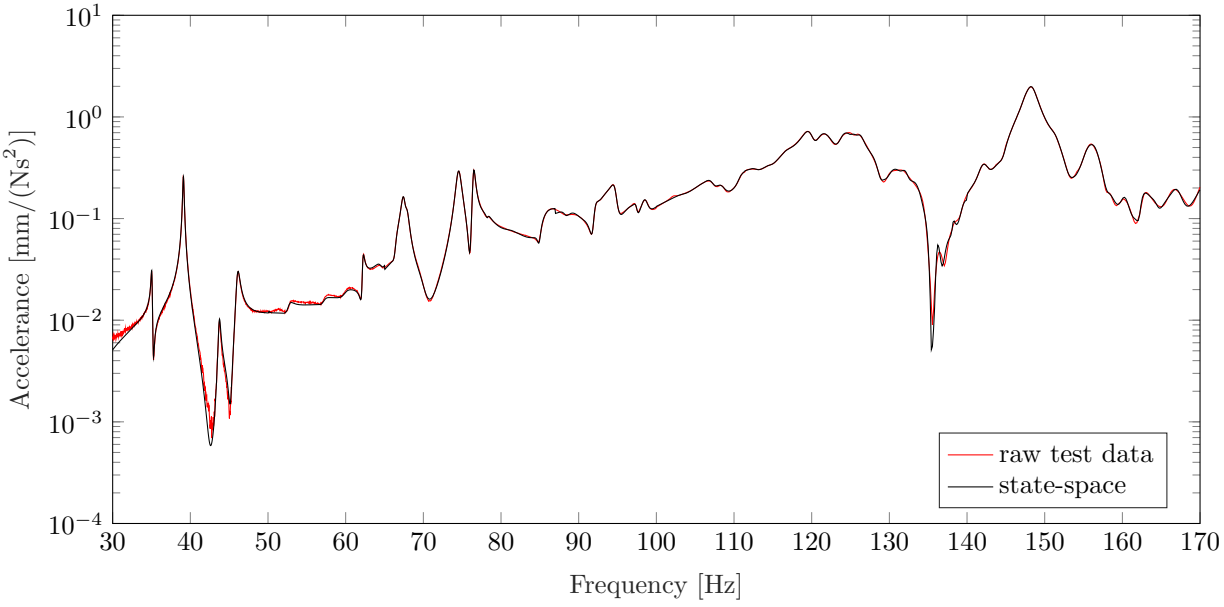

(b) *Sensor 14*

Figure 4.2: *FRFs of the raw test data and the identified state-space model of the BIW. (a) Sum over all FRFs between 30 Hz and 170 Hz. (b) FRFs in sensor 14 between 30 Hz and 170 Hz.*

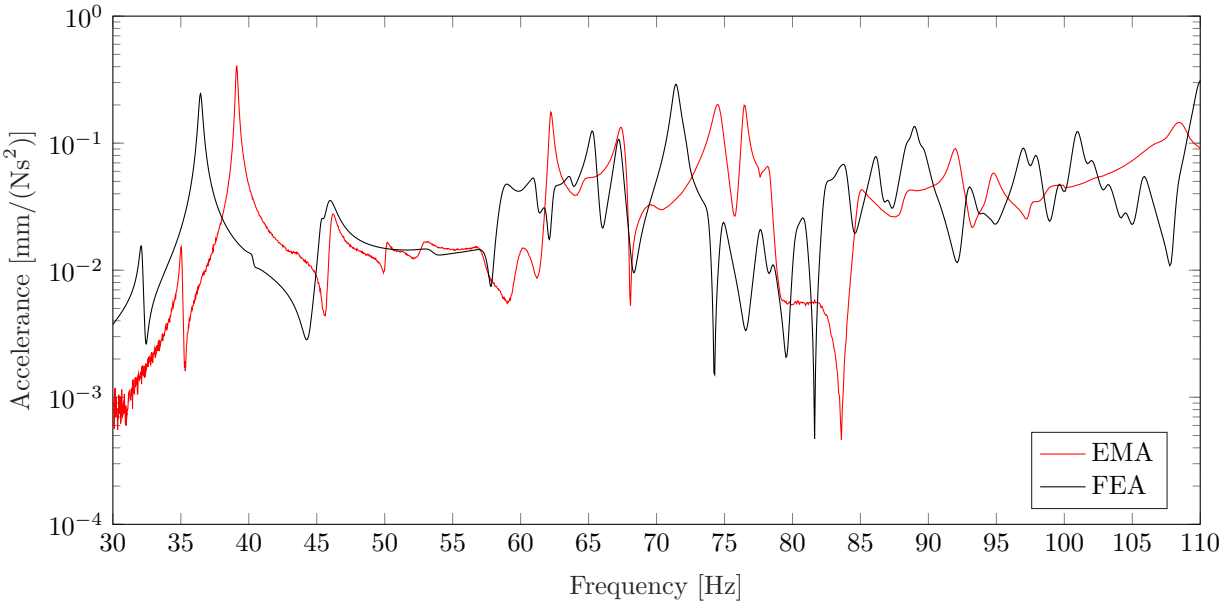

Figure 4.3: *FRFs obtained by the EMA and FEA in channel 15. Red denotes the EMA obtained results and black the FRF calculated by FEA.*

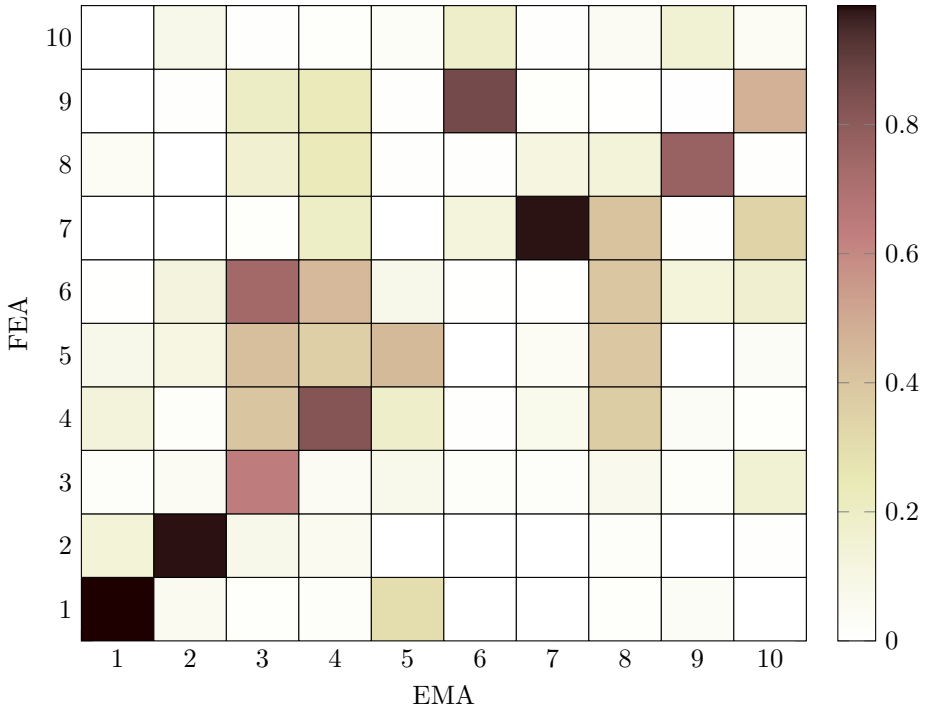

Figure 4.4: *MAC correlation between the FEA and EMA obtained eigenvectors.*

4.2 Calibration of the rear subframe

This section presents the calibration results of the subframe 112. It also shows a comparison to the calibrated subframe 220 from [GA17]. Analyzed are the fit of the FRFs, eigenfrequencies and the MAC correlation.

4.2.1 Calibrated subframe 112

As mentioned in Section 3.5.2, the calibration of subframe 112 was done by modifying the nominal values of in total seven parameters: Four Young's moduli belong to the material of the bushings (rubber) and three Young's moduli to steel parts. The former were determined in the mass loaded configuration and the latter in the calibration up to 265 Hz in the configuration without mass loading. Table 4.2 shows the nominal and calibrated values of the modified parameters for both configurations. Moreover, Table 4.2 summarizes the calibration statistics obtained from the bootstrapping procedure. These incorporate the coefficient of variation (COV), the mean value of each parameter and the deviation metric δ with respect to Equation 2.36. The mean value is displayed in parenthesis after the corresponding parameter. The nominal FE model $\mathrm{FE}_{\mathrm{nom}}$ corresponds to the FE model without mass loading. The FE models, that are related to the mass loaded configuration include the subscript ml. Additionally, the final mass of each FE model is shown. Table 4.3 shows the eigenfrequencies of the nominal and calibrated FE models as well as for the state-space models (EMA) that correspond to the measured raw data. Furthermore, the relative difference Δ between the experimental results and the results of the calibrated FE model is presented.

Table 4.2 shows a low COV for most of the parameters. An outlier with a COV of 5.58% can be detected at parameter E_1, which denotes the rubber stiffness of one bushing (c.f. Figure 3.10). The COV describes the parameter sensitivity to the noise of the measurement. A low COV indicates a stable and thus a reliable parameter. This means that E_1 should be considered as the most uncertain parameter. The mean values of some calibrated parameters differ substantially from the updated value, for instance for the parameters E_2 and E_7. The mean value is obtained from the bootstrapping analysis, which uses the raw experimantal data. The calibrated value is obtained from the estimated state-space model, which is not always equal to the raw data, as seen in Figure 4.5. Overall, most of the stiffness parameters, i.e. the Young's moduli E_1 to E_6 have been decreased according to their nominal value. The mass of FE_{265} is identical to $\mathrm{FE}_{\mathrm{nom}}$, since only stiffness values are updated. A comparison of the eigenfrequencies of $\mathrm{FE}_{\mathrm{nom}}$ and EMA in Table 4.3 shows, that the first eight flexible modes were measured to be lower than calculated by the FEA. A reduction of the stiffness by keeping the mass constant results in lower eigenfrequencies since the relation $\omega{=}\sqrt{k/m}$ between these three parameters holds. Thus, it is feasible, that most of the Young's moduli were decreased. Mode 2 is the only mode, where the frequency was not decreased after calibration. That means that FEA and EMA still differ by 5 Hz. Mode 2 practically affects only the backplate of the subframe (see Appendix A.1). This mode shape is quite local. Parameters, such as the plate thickness or stiffness of these area, are not included in the calibration parameter set. These would negatively influence the other mode shapes, i.e. mode switches and decreased MAC values.

Figure 4.5(a) shows the FRFs in channel 4x, a channel with a high fit for EMA and FE_{265}. Figure 4.5(b) shows the FRFs in a channel 30, which is a poorer one. These two channels are similar to the ones presented in [GA17]. Shown are the raw test data, the identfied state-space model and the two FE models $\mathrm{FE}_{\mathrm{nom}}$ and FE_{265}. The FRFs in Figure 4.5 support what is already visible in Table 4.3. Around mode 2, the shift in frequency for both FE models in comparison with the test data is clearly visible. The mode shapes are similar, which is also shown in Figure 4.6. Both channels indicate that FE_{265} correlates much better to the test data between 190 Hz and 200 Hz, which correspond to mode 3 to 6. The shift in frequency around 156 Hz is similar in $\mathrm{FE}_{\mathrm{nom}}$ and FE_{265}, but the resonances are of higher amplitude and thus more similar to the measured FRFs. Overall, the FRFs in channel 4x fit better between the different mode shapes, than the FRFs in channel 30. FE_{265} in channel 30 captures the resonances of the stae-sapce model quite well but shows larger deviations between the different resonances, for example between 160 Hz and 200 Hz as well as at the anti-resonance around 220 Hz.

Figure 4.6 shows the MAC correlation between the EMA and FEA obtained mode shapes before and after calibration. A significant increase for the correlation of the eigenvectors after calibration can be seen. The mode switch between mode 3 and 4 is fixed. Furthermore, the MAC values of mode 5 and 6 significantly increase by keeping the remaining ones still highly correlated (MAC>0.9). In total, mode 4 and 6 are the only ones that do not possess a high correlation (MAC>0.9) after calibration, but a much higher correlation

Table 4.2: Nominal and calibrated parameters, calibration statistics and masses for the two configurations. Parenthesis denote the mean value. The deviation according to Equation 2.36 is shown as well.

Parameter	FE_{nom}	FE_{ml}	FE_{265}	FE_{ml}^{COV}[%]	FE_{265}^{COV}[%]
E_1[MPa]	5.00	4.01 (3.90)	4.01	5.58	
E_2[MPa]	5.00	4.12 (3.27)	4.12	2.08	
E_3[MPa]	5.00	3.13 (3.56)	3.13	1.76	
E_4[MPa]	5.00	2.70 (2.57)	2.70	1.01	
E_5[GPa]	210.0	210.0	183.6 (183.1)		0.34
E_6[GPa]	210.0	210.0	202.1 (196.3)		1.09
E_7[GPa]	210.0	210.0	220.5 (238.8)		0.88
mass [kg]	26.73	37.01	26.73		
δ	0.91	0.62	0.56		

Table 4.3: Eigenfrequencies in [Hz] between 40 Hz and 265 Hz for the nominal and calibrated FE models as well as the experimental models.

Mode	EMA_{ml}	FE_{ml}^{nom}	FE_{ml}	Δ_{ml}[%]	EMA	FE_{nom}	FE_{265}	Δ_{265}[%]
1	41.60	46.45	42.47	2.08	75.88	78.20	76.68	1.06
2		48.16	43.73		153.47	158.18	157.86	2.86
3	52.08	53.92	52.34	0.51	191.35	194.63	191.04	-0.16
4	63.27	78.60	64.18	1.43	193.71	196.97	193.51	-0.10
5	66.60	80.03	66.07	-0.79	203.81	207.37	203.67	-0.07
6	67.84	82.50	68.66	1.21	205.42	208.84	206.95	0.74
7		84.96	70.86		238.77	241.10	237.15	-0.68
8		86.42	71.66		252.52	254.27	250.26	-0.90

than in FE_{nom}. The optimization by updating material parameter is just one option for model calibration. Other options are geometrical adjustments, for example curvature or thickness changes of surface sections. These adjustments are much more complex and are not included in this work. Nevertheless, it might be an opportunity to improve the calibration, for example to reach a high correlation for mode 4 and 6.

4.2.2 Comparison of subframe 112 and 220

Last, the two calibarted FE models of subframe 112 and 220 are compared up to a frequency of 265 Hz. Figure 4.8 shows the channels 4x and 30 for the two subframes. Figure 4.7 shows the MAC between the two calibrated models. It can be seen, that the FRFs are quite similar for the first two modes up to 156 Hz with as small shift in frequency around mode 2. Around mode 3 to 6, larger differences in the FRFs occur, which denote mainly a shift in frequency as well. The MAC in Figure 4.7 shows the lowest correlation for mode 3 to 6, but overall, the two calibrated subframes show a high correlation. Mode 4 is the only mode with a MAC below 0.9, i.e. MAC=0.89. The MAC is calculated between the channels, which occur in the calibration set of both subframes. That means, that 39 out of 56 channels are used. Figure 4.7 shows the frequencies of the occuring modes. It can be seen, that the differences between the two subframes are larger in frequency than in the mode shapes. This means, that the calibration of the nominal FE model FE_{nom} against two experimentally obtained data sets leads to a similar results for the occuring mode shapes, but to a shift in frequency.

Figure 4.9 shows the FRFs in channel 4x and channel 22 for the mass loaded configuration between 40 Hz and 220 Hz. The mass loaded configuration contains only updated bushing stiffnesses. All other parameters are identical in the subframes. Sensor 4 belongs to the set of sensors placed on the added masses [GA17]. It can be seen, that the differences in the mass loaded configuration are more significant than in the configuration without mass loading. Especially between 130 Hz and 160 Hz large differences are visible. Further, the mass loaded configuration shows more eigenmodes between 40 Hz and 220 Hz than the configuration without mass loading, as expected because the mass loading brings more modes down in frequency.

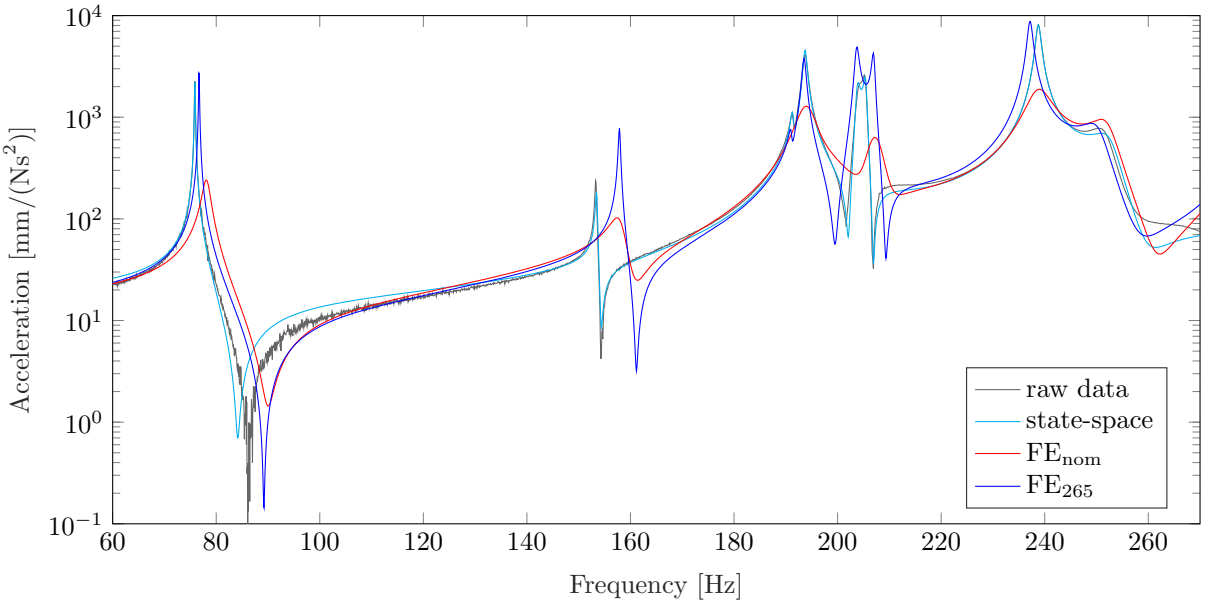

(a) *FRF in channel 4x*

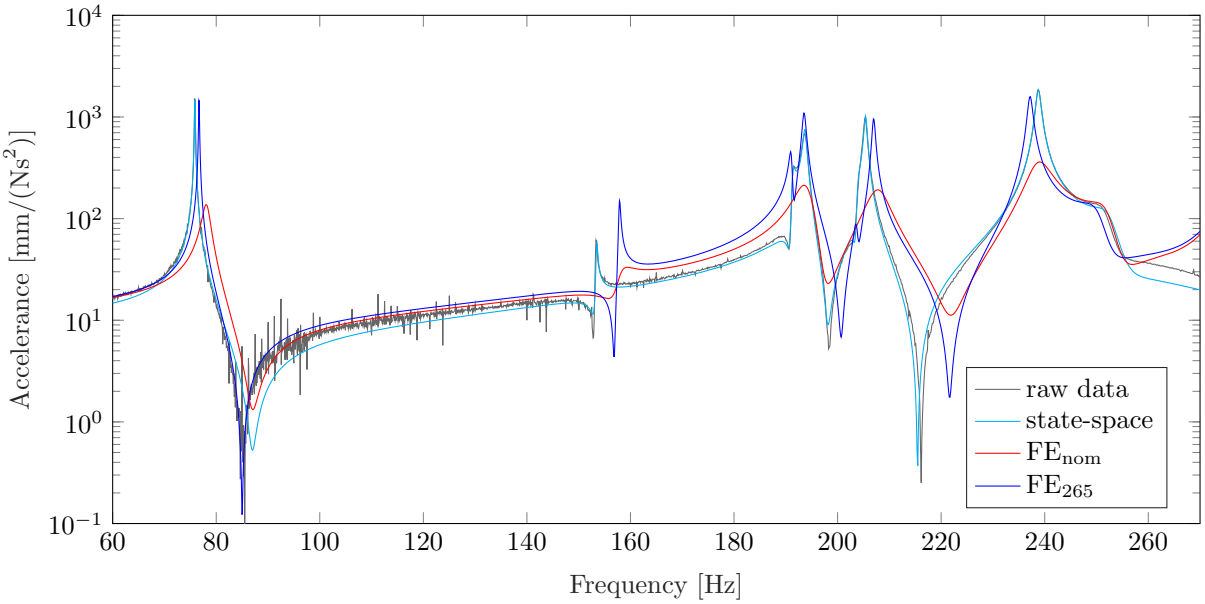

(b) *FRF in channel 30*

Figure 4.5: *FRFs of the calibrated subframe 112 and 220 between 60 Hz and 270 Hz. Shown is the raw test data (grey), the corresponding state-space model (black), the nominal FE model FE_{nom} (red) and the calibrated FE model FE_{265} (blue).*

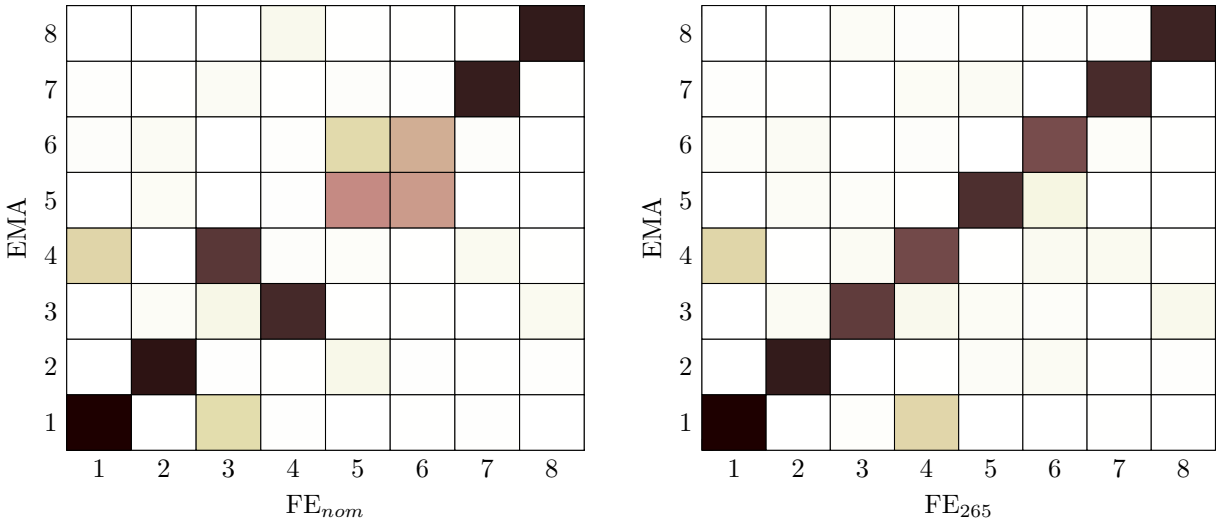

Figure 4.6: *MAC correlation between experimentally and CAE obtained eigenvectors. (a) MAC before calibration. (b) MAC after calibration.*

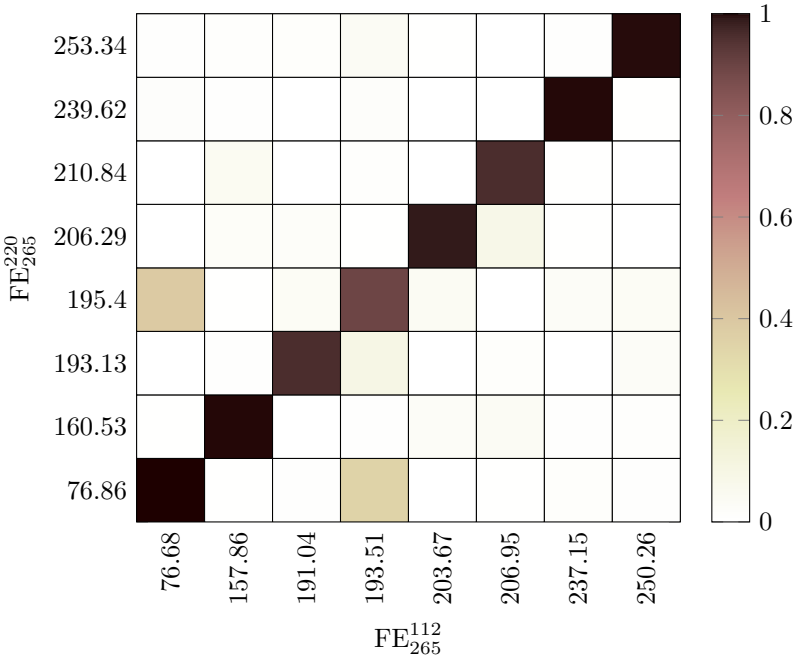

Figure 4.7: *MAC correlation of subframe 112 and 220 between 70 Hz and 265 Hz, i.e. the first eight eigenmodes.*

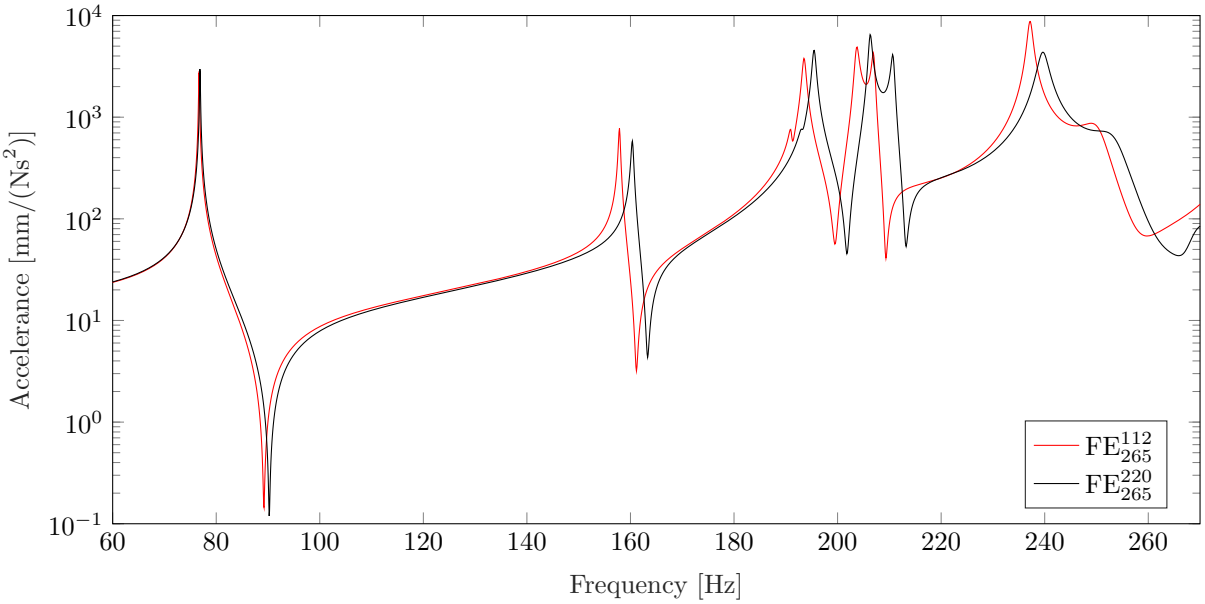

(a) *FRFs in channel 4x*

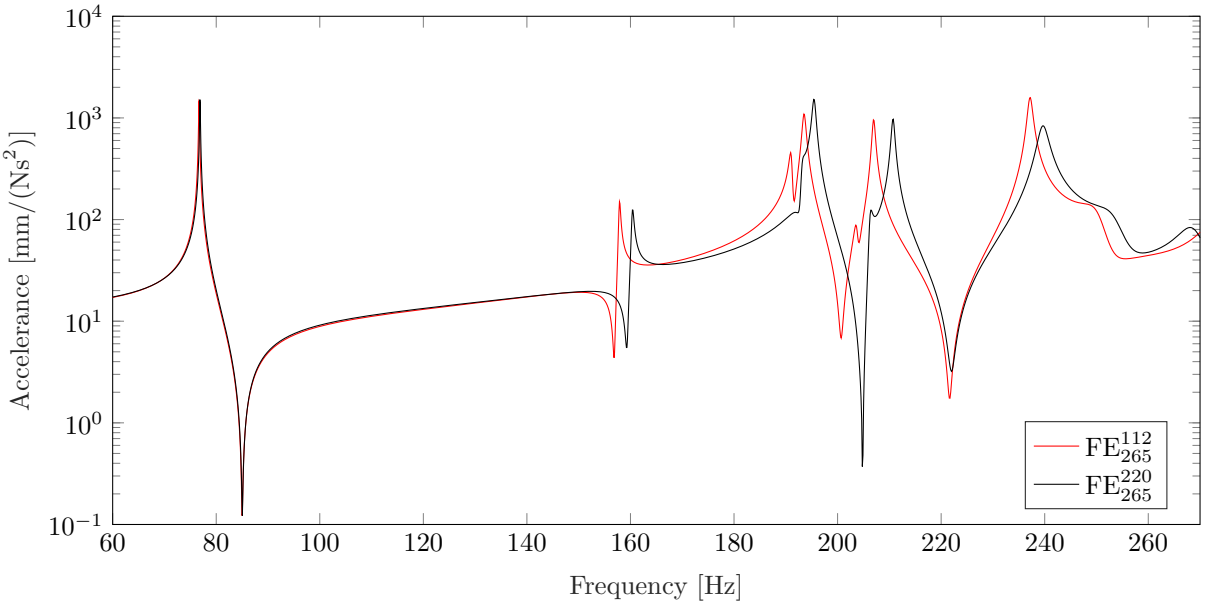

(b) *FRFs in channel 30*

Figure 4.8: *FRFs of the calibrated subframe 112 and 220 between 60 Hz and 270 Hz.* FE_{265}^{112} *denotes the calibrated FE model of subframe 112 (red) and* FE_{265}^{220} *stands for the calibrated model of subframe 220 (black).*

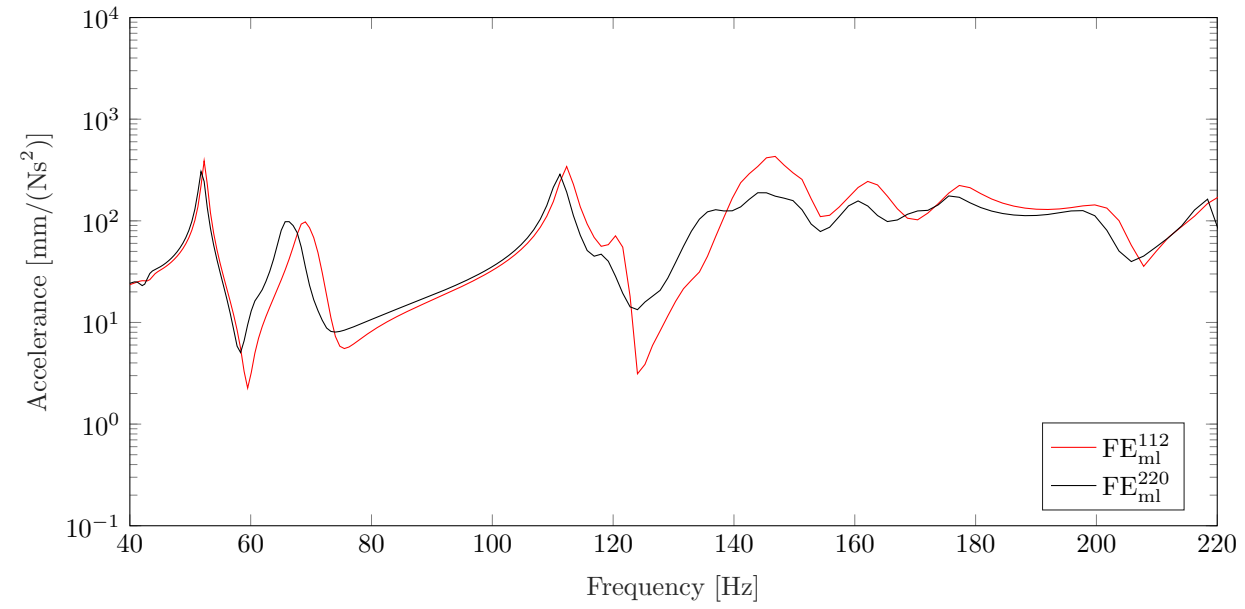

(a) *FRFs in channel 4x*

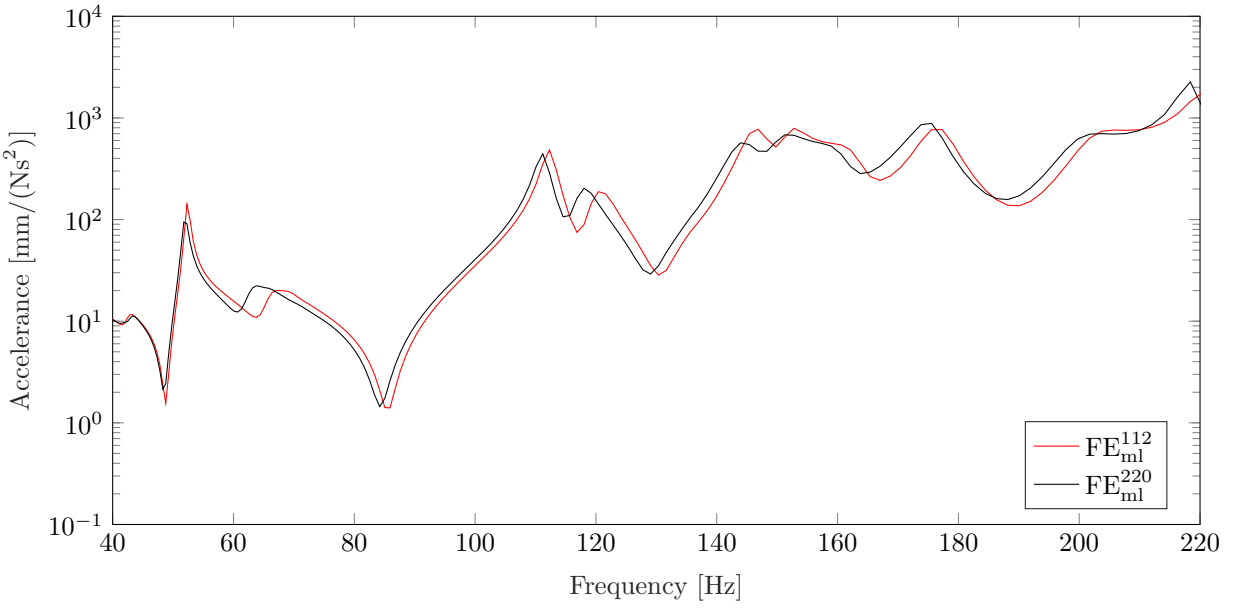

(b) *FRFs in channel 22*

Figure 4.9: *FRFs in channel 4x and 22 of subframe 112 and 220 between 40 Hz and 220 Hz in the mass loaded configuration.*

Table 4.4: Number of DOFs and computed modes for the different models of the subframes, BIW and the assembly. The number of modes up to 600 Hz has not been computed for the two assemblies.

	BIW	subframe 112	subframe 220	A_{112}	A_{220}
# DoFs full	>10 million	>0.5 million	>0.5 million	>15 million	>15 million
# DoFs CB	1929	84	84	1989	1989
# modes	1879	30	30	-	-
mass [kg]	427.25	26.73	26.52	454.39	456.15

Table 4.5: SUMAC correlation values for the modes 1 to 48 of the assemblies A_{112} and A_{220}. Modes, which are less affected by the assembly (SUMAC>0.9), correspond to the BIW mode shapes and are highlighted by bold numbers.

# mode	SUMAC A_{112}	SUMAC A_{220}	# mode	SUMAC A_{112}	SUMAC A_{220}	# mode	SUMAC A_{112}	SUMAC A_{220}
1	**0.99**	**0.99**	17	0.75	0.73	33	0.22	0.22
2	**1.00**	**1.00**	18	0.28	0.26	34	0.43	0.54
3	0.76	0.76	19	**0.94**	**0.94**	35	0.18	0.15
4	**0.90**	**0.90**	20	**0.97**	**0.92**	36	0.13	0.13
5	0.65	0.65	21	0.06	0.02	37	0.00	0.00
6	**1.00**	**1.00**	22	0.17	0.11	38	0.27	0.27
7	**0.99**	**0.99**	23	0.62	0.60	39	0.10	0.12
8	**0.98**	**0.97**	24	0.07	0.14	40	0.57	0.58
9	0.01	0.01	25	0.02	0.02	41	0.58	0.54
10	0.07	0.07	26	0.34	0.33	42	0.14	0.18
11	0.02	0.01	27	0.18	0.18	43	0.50	0.49
12	0.09	0.11	28	0.39	0.39	44	0.29	0.28
13	0.03	0.03	29	0.03	0.03	45	0.67	0.69
14	0.79	0.78	30	0.07	0.07	46	0.77	0.82
15	**0.99**	**0.99**	31	0.09	0.08	47	0.00	0.05
16	0.85	0.84	32	0.02	0.02	48	0.54	0.12

4.3 Assembly of BIW and subframes

This section summarizes the results of the assembly of one BIW coupled with the two calibrated subframes 112 and 220. In the following, the assembly with subframe 112 is designated as A_{112} and the assembly with subframe 220 as A_{220}. The calibration results of the two subframes are shown in Section 4.2. The coupling is considered from the experimental as well as simulation point of view. The differences between the two coupled models in terms of eigenfrequencies and mode shapes are of interest. These models include FE models, the experiment as well as the comparison of both. As already mentioned in Section 4.1, the FE model and the EMA do not correlate well. This led to the conclusion that the FE model does not model the experimental test setup, or rather BIW test specimen well. This inconsistency will also negatively influence the results for the assembly, since the same BIW model is used. Thus, this section qualitativley compares FEA and EMA results by comparing trends instead of a direct comparison of eigenvalues, vectors, etc.

4.3.1 Coupling in FE

The coupling in A_{112} and A_{220} was performed with the CMS presented in Section 2.5.3 and 2.5.4. The resulting eigenfrequencies and eigenvectors are compared as well as the sum of the FRFs for the sensors at the BIW. The SUMAC is introduced to analyze which mode shapes of the BIW are affected by the coupling to a subframe. The damping of the coupled system $\boldsymbol{V}_{cms}$ is modeled as modal damping as described in Equation 2.40. In this equation ξ_0 is set to the average of the damping estimated in the EMA for the BIW (ξ_0=0.0049) and the two assemblies A_{112} (ξ_0=0.0051) and A_{220} (ξ_0=0.0051). To cover all effects on the interface, a frequency range of 0

Hz up to 600 Hz was considered for all coupled models in the FEA. For substructures with a linear behavior, it is suggested to use 1.5 to 2.0 times the maximum frequency of interest [AMR14], which is well captured by the chosen frequency range.

Table 4.4 summarizes the amount of DoFs used for the different structures. Moreover, the amount of considered modes as well as the mass of each model is listed. The mass of the two assemblies included the connectors of the four screws.

Let's first take a look at the SUMAC according to Equation 2.33. The SUMAC is evaluated between the BIW alone and the corresponding assemblies. A low SUMAC corresponds to a high influence of a mode due to the assembly and a high SUMAC correlates to almost no influence for the global mode shape on the BIW. Table 4.5 lists all SUMAC values for the first 48 mode shapes between 30 Hz and 100 Hz. The SUMAC values up to mode 178 can be found in Appendix . They show low SUMAC values and thus a change of the original BIW modes shapes. The range between 30 Hz and 170 Hz will be analyzed in the experimental coupling in Section 4.3.2. In that range, the FE coupling is treated as well. Table 4.5 shows, that in case of the eight global mode shapes (mode 1 to 8), only the modes 3 and 5 are mainly influenced by the coupling of the subframes to the BIW. Figure 4.1 shows, that mode 3 and 5 correspond to modes, where the area of the subframe or the adjacent area (mode 3) is highly affected by the mode shape. The remaining 6 modes do not show any or only a low contribution in the subframe area. Thus, it seems plausible that mode 3 and 5 are designated as mainly affected. At higher frequencies, most of the modes are significantly affected, except for the modes 15, 19 and 20. On average, the attachment of subframe 112 has a similar effect as the attachment of subframe 220 in terms of the SUMAC. This is plausible because two nominally identical parts are connected and may not lead to a completely different behavior. In total, both assemblies show 169 out of 178 modes with a SUMAC$<$0.9.

Figure 4.10 shows the sum of the resulting FRFs of all the sensor positions in a frequency range between 30 Hz and 300 Hz in (a) and a more detaile view for the range between 30 Hz and 170 Hz for the two assemblies in (b). Table 4.6 summarizes the eigenfrequencies, relative difference and MAC correlation values for all modes up to 170 Hz with a MAC$<$1.00. The results of all values can be found in Appendix D. The MAC and the relative difference Δ in eigenfrequencies are estimated between the two assemblies A_{112} and A_{220}.

Figure 4.10 shows a similar dynamic response of both assemblies. Major differences are visible around 100 Hz, 125 Hz to 140 Hz and 220 Hz. The NRMSE is 0.870 for the range up to 300 Hz and 0.868 up to 170 Hz for the sum of the FRFs. A separate analysis of each channel shows, that the sensors on the BIW, except 12 and 26, show a higher fit according to the NRMSE than the sensors on the subframes of the two assemblies. This means, that larger differences occur in the local behavior of the subframes but do not propagate proportional in the assemblies, i.e. the differences are less visible in the assemblies. Figure G.1 shows the FRFs of sensor 12 and 36, normal (z)-direction, for both assemblies. These two channels correspond to the weakest fit of the BIW and subframe sensors. Sensor 12 shows the major difference between the two assemblies around 100 Hz to 110 Hz and between 120 Hz and 140 Hz, similar to the sum of the FRFs in Figure 4.10. Channel 36z additonally indicates differences between 150 Hz and 170 Hz. A check of all channels shows that the differences between 150 Hz and 170 Hz are generally only visible in sensors on the subframe. Appendix E shows for completeness the sum over the FRFs for the BIW sensors and subframe sensors, separately.

Table 4.6 shows a similar dynamic response in the lower frequency range, i.e. below 96 Hz of both assemblies. All modes below 74 Hz show a MAC=1.00 and are skipped in the table. They can be found in Appendix H. All mode shapes are still highly correlated, i.e. MAC$>$0.90, below a frequency of 96 Hz. Low correlation occurs for two modes around 97 Hz, one around 103 Hz and 122 Hz, three around 127 Hz and further for single modes at higher frequencies. The weakest correlation occurs around 166 Hz, for seven modes, where the MAC denotes completely non-correlated modes, i.e. MAC$<$0.1. This area corresponds, as mentioned before, to the significant differences on the channels on the subframes. Visible is, that the non-correlated modes occur, where A_{112} results in lower eigenfrequencies than A_{220}. In total, 22 out of 178 modes show a low or no correlation between the the two assemblies. Thus, the majority of mode shapes show a similar response for both assemblies.

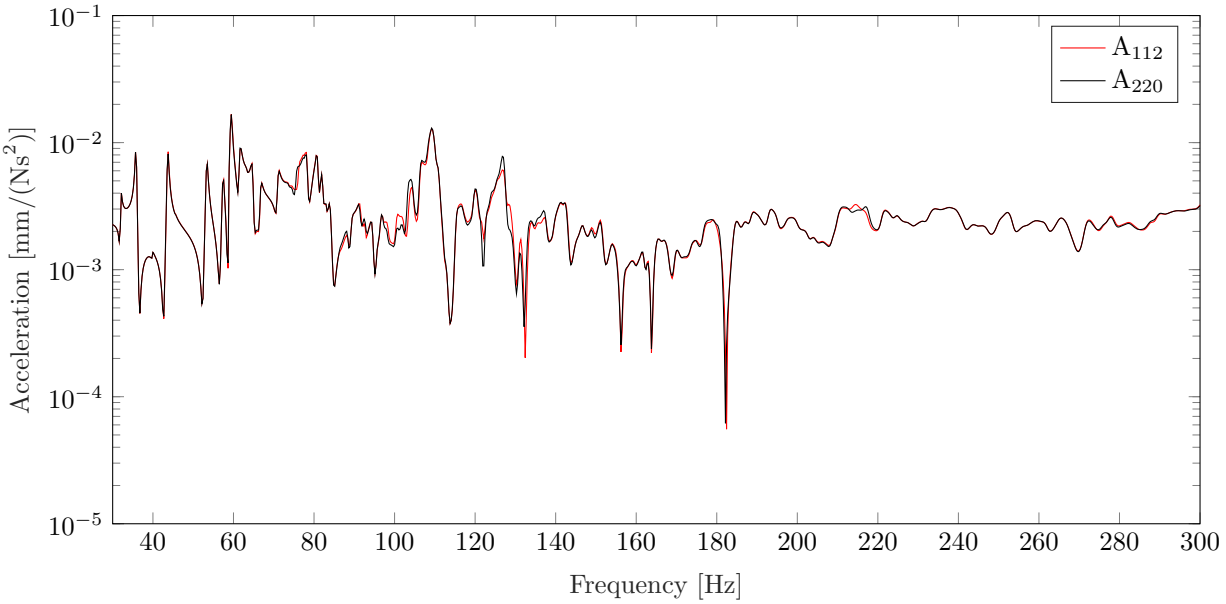

(a) *30 Hz and 300 Hz*

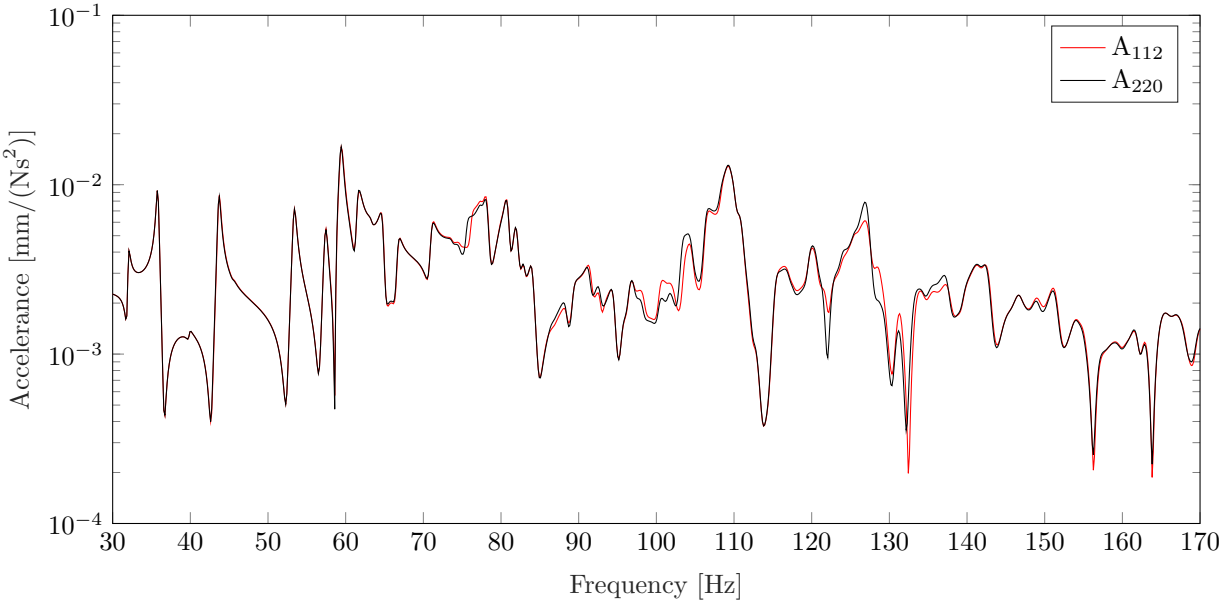

(b) *30 Hz and 170 Hz*

Figure 4.10: *Sum of all FRFs estimated of the CMS. (a) frequency range between 30 Hz and 300 Hz. (b) frequency range between 30 Hz to 170 Hz. Red denotes the assembly A_{112} and black denotes the assembly A_{220}.*

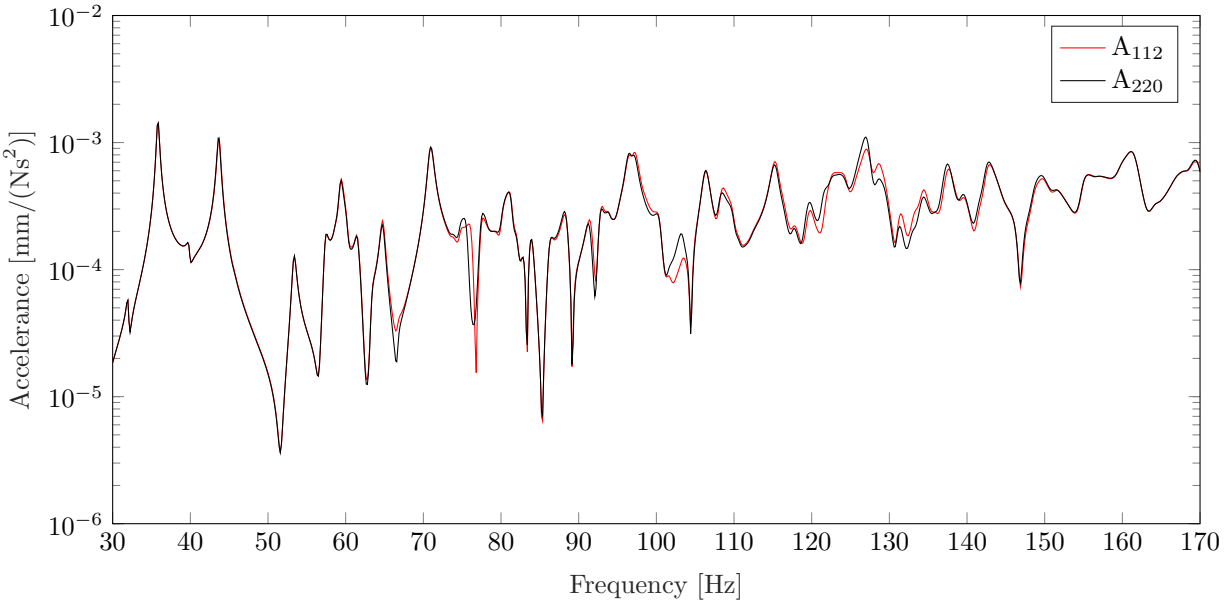

(a) *FRFs in channel 12*

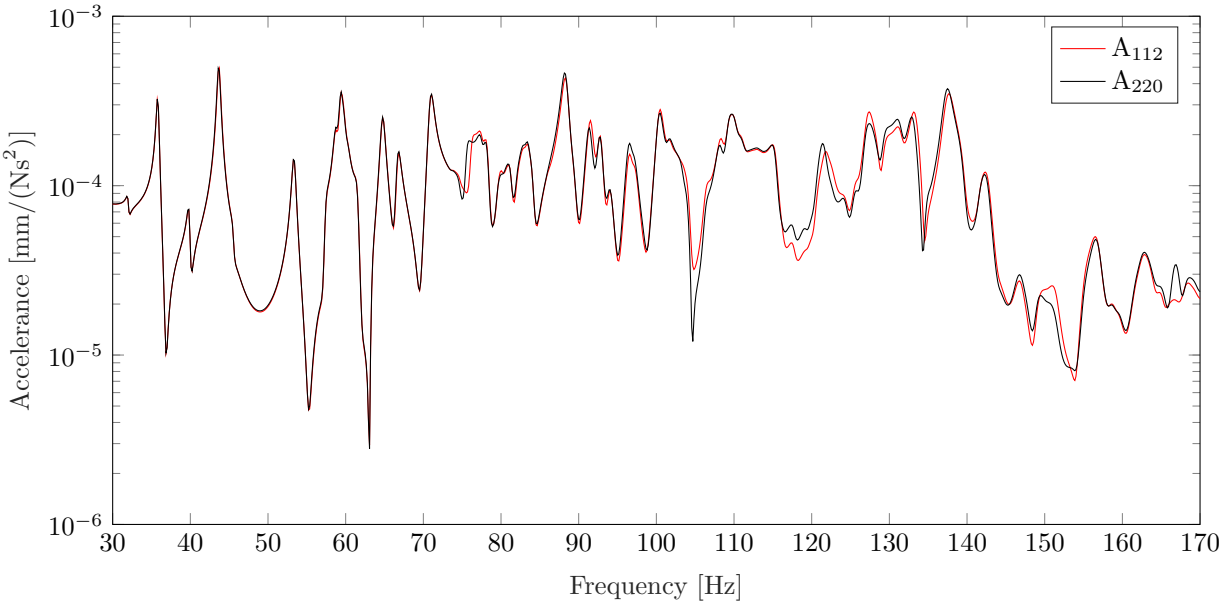

(b) *FRFs in channel 36z*

Figure 4.11: *FRFs between 30 Hz and 170 Hz for channel 12 and 36z.*

Table 4.6: The eigenfrequencies of the first 178 flexible modes with a MAC<1.00 between the two assemblies. A_{112} and A_{220} are obtained from FEA. The relative difference is denoted by Δ_A and calculated between A_{112} and A_{220} in %. MAC denotes the correlation of A_{112} and A_{220} with respect to Equation 2.31.

# mode	BIW	A_{112}	A_{220}	Δ_A	MAC	# mode	BIW	A_{112}	A_{220}	Δ_A	MAC
20	74.76	74.72	74.69	0.03	**0.95**	100	136.02	132.00	132.00	0.00	**0.99**
21	77.57	76.16	75.56	0.60	**0.99**	101	136.14	133.25	133.03	0.22	**0.92**
22	78.49	77.47	77.44	0.04	**0.97**	102	136.23	133.40	133.34	0.06	0.8
24	80.06	79.55	79.47	0.08	**0.97**	103	137.11	134.43	134.40	0.03	**0.99**
34	88.89	88.29	88.23	0.06	**0.98**	108	141.07	137.36	137.34	0.02	0.66
35	89.46	88.38	88.37	0.01	**0.97**	109	141.36	137.49	137.43	0.05	**0.94**
41	93.91	93.10	93.02	0.08	**0.99**	110	141.65	137.75	137.63	0.11	**0.93**
43	95.55	93.96	93.94	0.02	**0.99**	111	141.75	139.12	139.11	0.01	**0.99**
46	97.75	96.52	96.49	0.03	**0.99**	113	142.94	140.86	140.82	0.05	**0.99**
47	99.52	97.17	97.12	0.05	0.89	117	145.98	142.65	142.58	0.08	**0.94**
48	100.77	97.23	97.21	0.02	0.75	118	146.73	142.74	142.73	0.01	**0.98**
49	101.74	98.39	98.21	0.18	**0.98**	119	147.04	143.04	143.04	0.00	**0.99**
50	102.55	100.43	100.37	0.06	**0.99**	128	151.03	148.72	148.70	0.02	**0.99**
51	103.05	101.57	101.56	0.02	**0.94**	129	151.25	149.13	149.09	0.03	0.60
52	104.22	102.38	102.32	0.06	**0.97**	130	152.35	149.14	149.13	0.01	0.06
53	104.52	103.02	103.02	0.01	**0.96**	131	152.81	149.62	149.55	0.07	**0.99**
54	105.30	103.59	103.33	0.26	0.89	133	153.96	151.14	150.99	0.16	**0.94**
55	107.06	104.10	104.01	0.09	**0.99**	134	154.66	151.30	151.28	0.02	0.45
56	107.27	104.67	104.59	0.08	**0.99**	139	156.97	154.18	154.16	0.03	**0.97**
57	107.90	104.76	104.74	0.02	**0.99**	141	157.99	155.00	154.94	0.05	**0.99**
60	109.72	107.92	107.91	0.01	**0.93**	148	161.81	158.52	158.50	0.01	0.64
61	110.16	108.36	108.22	0.13	**0.99**	149	162.03	158.68	158.59	0.08	**0.97**
64	111.99	110.27	110.26	0.01	**0.97**	157	166.00	162.70	162.70	0.00	**0.93**
69	113.82	112.80	112.79	0.01	**0.99**	159	166.57	164.33	164.35	-0.02	**0.93**
77	120.48	119.37	119.28	0.09	**0.99**	160	166.78	164.50	164.50	-0.01	**0.99**
81	124.10	121.86	121.48	0.39	**0.91**	161	167.62	165.03	165.05	-0.02	0.83
82	124.12	122.45	122.40	0.04	**0.93**	162	168.21	165.26	165.47	-0.21	0.17
83	124.24	122.72	122.62	0.11	0.86	163	168.72	165.62	166.01	-0.39	0.02
84	125.21	123.89	123.86	0.03	**0.99**	164	168.92	166.03	166.16	-0.13	0.02
87	126.18	124.44	124.38	0.06	**0.96**	165	169.18	166.16	166.49	-0.33	0.04
89	127.42	125.68	125.64	0.04	**0.97**	166	169.53	166.59	166.63	-0.04	0.39
90	128.13	125.99	125.94	0.04	**0.91**	167	170.27	167.19	167.30	-0.12	0.74
91	129.26	126.44	126.30	0.14	**0.90**	168	170.65	168.02	167.99	0.03	**0.99**
92	130.23	126.94	126.93	0.01	**0.98**	169	170.70	168.15	168.13	0.02	0.77
93	130.96	127.22	127.10	0.12	0.75	170	170.98	168.73	168.72	0.01	**0.97**
94	131.06	128.42	127.56	0.86	0.80	173	172.39	169.63	169.63	0.00	**0.94**
95	132.00	128.66	128.62	0.05	0.84	174	172.56	170.29	170.29	0.00	**0.99**
96	133.28	129.27	129.25	0.02	**0.98**	175	172.77	170.69	170.69	0.00	**0.99**
97	133.72	130.87	130.79	0.08	**0.98**	176	173.59	170.74	170.74	0.00	**0.99**
98	134.59	131.29	131.25	0.04	**0.95**	178	174.66	171.65	171.62	0.03	**0.93**
99	135.80	131.44	131.38	0.06	**0.97**						

Table 4.7: SUMAC correlation values for mode 1 to 29 of the assemblies A_{112} and A_{220}. Modes, which are less affected by the assembly (SUMAC>0.9), correspond to the BIW mode shapes and are highlighted by bold numbers. The paranthesis denote the corresponding mode of the BIW alone.

# mode	SUMAC A_{112}	SUMAC A_{220}	# mode	SUMAC A_{112}	SUMAC A_{220}	# mode	SUMAC A_{112}	SUMAC A_{220}
1(1)	**0.99**	**0.99**	11(12)	0.02	0.08	21(22)	0.48	0.41
2(2)	**0.99**	**0.99**	12(13)	0.00	0.00	22(23)	0.14	0.08
3(4)	**0.90**	**0.90**	13(14)	0.18	0.18	23(24)	0.28	0.30
4(5)	0.46	0.68	14(15)	0.66	0.65	24(25)	0.00	0.00
5(6)	**0.99**	**0.98**	15(16)	0.01	0.01	25(26)	0.43	0.40
6(7)	**1.00**	**1.00**	16(17)	0.04	0.00	26(27)	0.02	0.01
7(8)	**0.98**	**0.99**	17(18)	0.22	0.21	27(28)	0.07	0.17
8(9)	**0.97**	**0.97**	18(19)	0.01	0.01	28(29)	0.06	0.06
9(10)	0.37	0.35	19(20)	0.42	0.34	29(30)	0.32	0.02
10(11)	0.01	0.02	20(21)	0.00	0.00			

4.3.2 Coupling in EMA

This chapter summarizes the experimental results of the analysis of the two assemblies. Both assemblies are measured in the frequency range between 30 Hz and 300 Hz and considered in more detail between 30 Hz and 170 Hz. Similar to the FE coupling, the SUMAC is evaluated and summarized for the modes up to 100 Hz in Table 4.7. The SUMAC for all modes up to 170 Hz can be found in Appendix F. The EMA highlights that mode 3 and 4 are the most affected modes. At higher frequencies, i.e. above 60 Hz, most of the modes are significantly affected. On average, both assemblies show a similar SUMAC. This means that the same modes are equally affected. In total, both assemblies show 61 out of 67 modes with a SUMAC<0.9. This demonstrates a high influence of the coupling of the subframe for the mode shapes of the BIW.

Figure 4.12(a) shows the the sum over all measured FRFs in the sensors between 30 Hz and 300 Hz. The FRFs show in the whole range small deviations. Major diffrences are visible around 90 Hz, 120 Hz to 140 Hz, 160 Hz and 200 Hz to 220 Hz. The area around 220 Hz seems affected by a mode switch. The range up to 170 Hz is considered in more detail, which captures most of the major affected areas. Figure 4.12(b) shows the sum over all FRFs of the raw test data together with the identified state-space models for the two assemblies. Shown is the frequency range between 30 Hz and 170 Hz. The state-space models are estimated in an identical procedure for both measurements. This allows to capture the difference between the two measurement data sets. It can be seen, that the mathematical models capture the measured data pretty good. Both state-space models show a weak fit only around 70 Hz and 120 Hz. Here, not all channels show a distinct resonance. Additionally, from the graphs in Figure 4.12 it can be concluded that the differences between the two assemblies are the eigenvectors. The resonances occur at similar frequencies. Figure 4.13 shows the FRFs of the same two sensors, i.e. sensor 12 and 36z, as in the FE coupling. The fit according to the NRMSE is 0.780 for the raw data in the range between 30 Hz and 300 Hz. Between 30 Hz and 170 Hz, the fit results in 0.865 for both the raw data and the state-space models. The separate analysis of each sensor denotes on average higher variations in the sensors on the subframe than in the sensors on the BIW. This is also true in the FE coupling. Appendix G shows for completeness the sum over the FRFs for the BIW sensors and subframe sensors, separately.

Table 4.8 summarizes the frequencies for the 67 estimated modes below 170 Hz of the two assemblies as well as the relative difference Δ in frequencies between both and the MAC values for the eigenvectors. Additionally, the eigenfrequencies of the individual analysis of the BIW are shown. The maximum relative difference in frequency is 0.89% for the two assemblies. In total, 32 out of 67 modes show a high correlation MAC>0.9. The MAC denotes the frequency range between 140 Hz and 160 Hz as containing the fewest modes correlated. The majority of the mode shapes occur in A_{112} at higher frequencies than in A_{220}. In comparison to the eigenfrequencies of the BIW alone, the assemblies result in mode shapes at higher frequencies, which means that in a general sense the increase of stiffness excels the increase of mass.

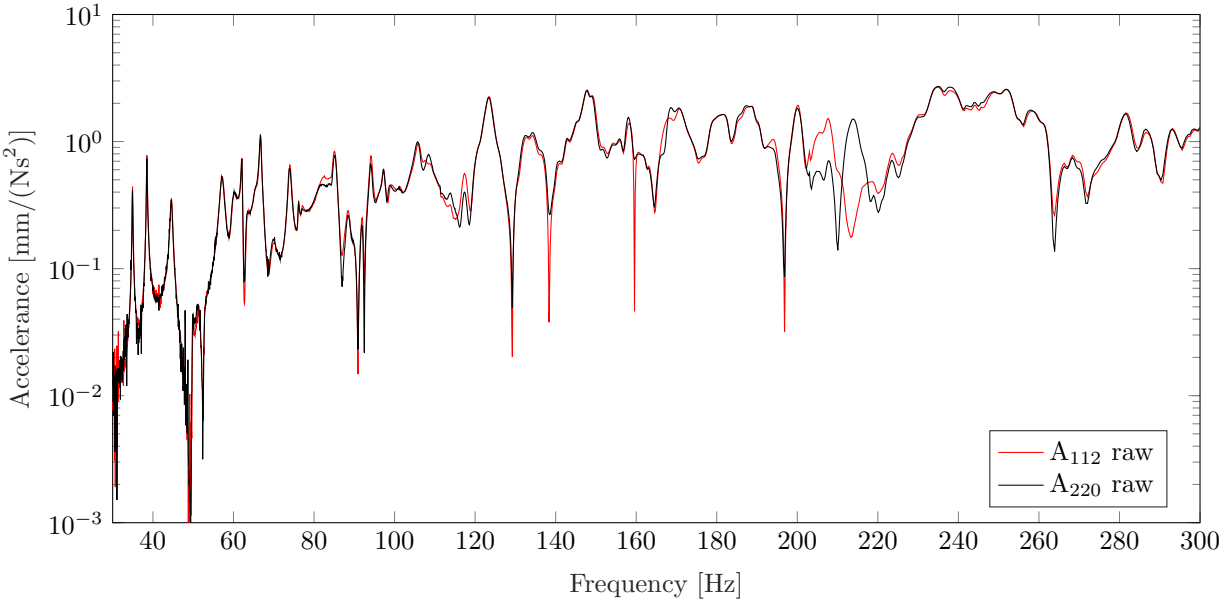

(a) *Frequency range between 30 Hz and 300 Hz*

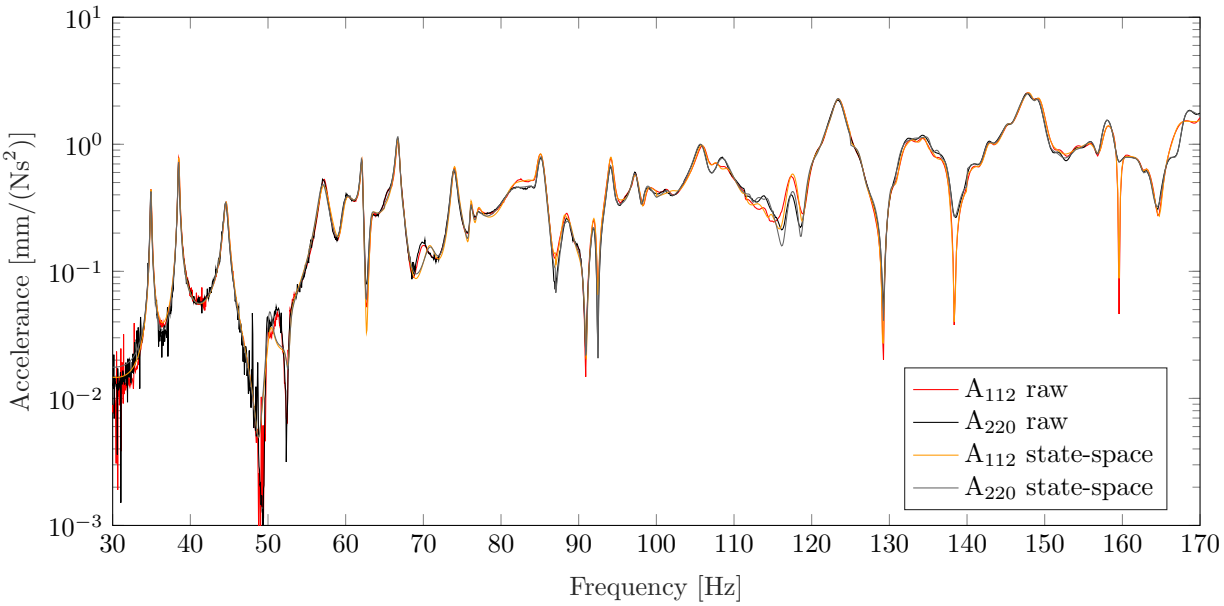

(b) *Frequency range between 30 Hz and 170 Hz.*

Figure 4.12: *Sum of FRFs. (a) between 30 and 300 Hz and (b) between 30 and 170 Hz.*

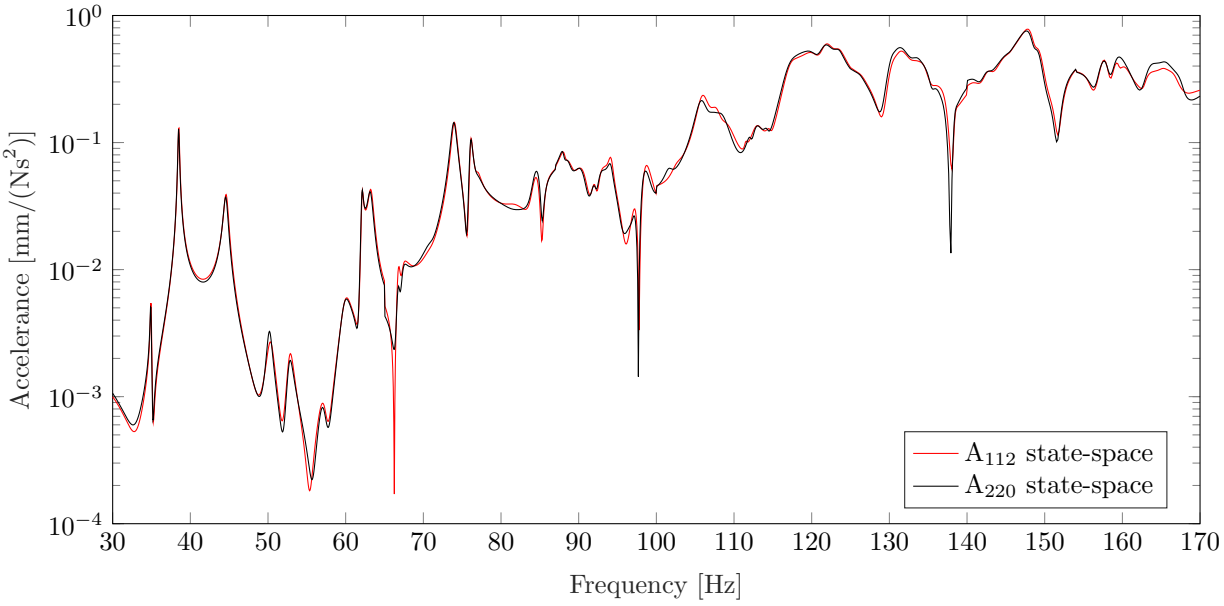

(a) *FRFs in channel 12*

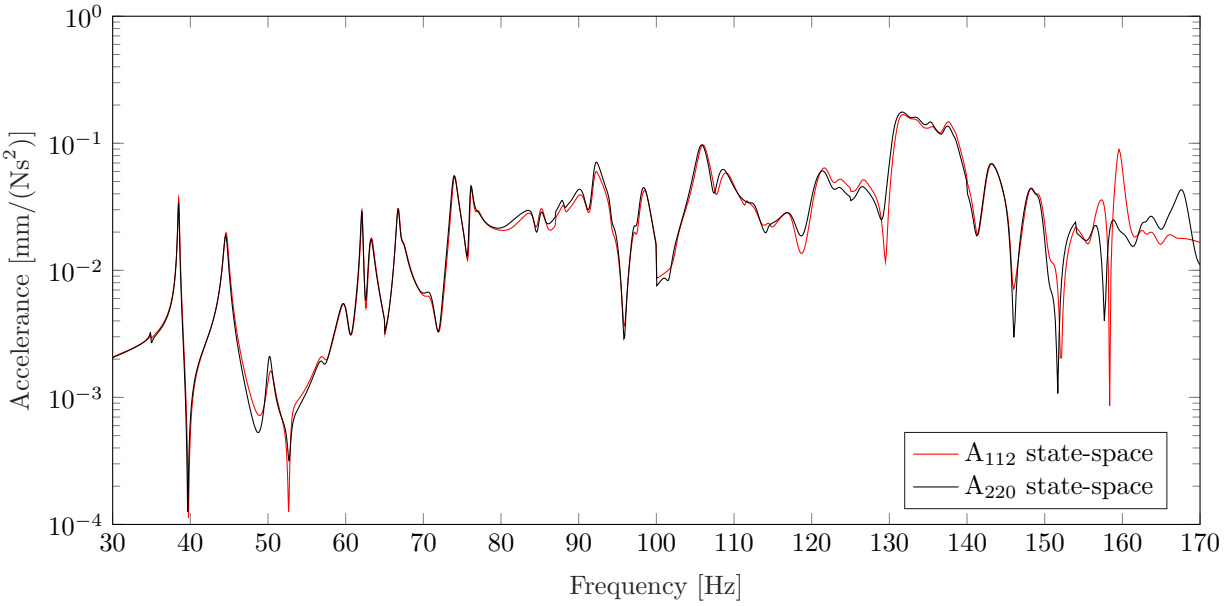

(b) *FRFs in channel 36z*

Figure 4.13: *FRFs between 30 Hz and 170 Hz for channel 12 and 36z.*

Table 4.8: The eigenfrequencies of the first 67 flexible modes below 170 Hz obtained from the EMA. Δ_A denotes the relative difference between A_{112} and A_{220} in %. MAC denotes the correlation of A_{112} and A_{220}.

# mode	BIW	A_{112}	A_{220}	Δ_A	MAC	# mode	BIW	A_{112}	A_{220}	Δ_A	MAC
1	35.05	34.94	34.92	0.06	**1.00**	35	107.22	114.59	114.25	0.29	0.73
2	39.11	38.51	38.49	0.05	**1.00**	36	108.37	117.34	117.23	0.09	**0.91**
3	43.73	44.61	44.56	0.11	**1.00**	37	110.94	118.11	118.10	0.01	0.87
4	46.08	50.31	50.17	0.28	0.86	38	111.16	120.35	120.20	0.13	**0.98**
5	50.11	52.83	52.77	0.11	**0.99**	39	112.55	121.79	121.63	0.13	0.15
6	52.68	57.15	57.03	0.22	**1.00**	40	114.63	123.44	123.40	0.03	**0.96**
7	57.21	59.94	59.87	0.11	**0.96**	41	116.78	126.47	126.27	0.16	**1.00**
8	59.91	62.12	62.09	0.05	**1.00**	42	118.01	130.09	129.82	0.21	0.59
9	62.22	63.25	63.19	0.10	**0.99**	43	119.99	131.06	130.41	0.50	0.51
10	64.50	66.77	66.75	0.03	**1.00**	44	120.96	131.45	131.55	-0.08	0.39
11	66.40	67.29	67.28	0.03	**0.97**	45	122.04	133.17	133.42	-0.19	0.33
12	67.46	70.82	70.87	-0.07	0.06	46	123.88	134.52	135.38	-0.64	0.54
13	67.87	73.99	73.92	0.10	**1.00**	47	125.79	135.46	136.68	-0.89	0.68
14	69.82	76.10	76.06	0.05	**1.00**	48	126.27	137.48	137.38	0.07	**0.90**
15	74.53	76.92	76.88	0.06	**0.96**	49	128.75	138.39	138.38	0.01	0.39
16	75.51	81.40	81.44	-0.05	0.86	50	129.52	141.39	141.43	-0.03	0.12
17	76.47	84.37	84.39	-0.02	**0.98**	51	131.51	142.72	142.61	0.08	0.64
18	77.70	85.17	85.17	0.01	**0.99**	52	132.22	144.44	144.99	-0.38	0.71
19	78.28	88.19	88.05	0.16	**0.98**	53	133.78	145.51	145.45	0.04	0.76
20	80.94	88.68	88.60	0.08	**0.98**	54	134.97	148.41	148.56	-0.10	**0.99**
21	84.93	90.58	90.50	0.09	**0.98**	55	136.25	148.83	148.75	0.05	0.79
22	85.48	92.13	92.11	0.02	0.01	56	136.91	149.19	149.00	0.13	**0.97**
23	88.32	92.65	92.58	0.07	**0.94**	57	138.17	151.67	151.70	-0.02	**0.99**
24	89.87	94.17	94.14	0.03	**0.98**	58	139.27	156.09	156.24	-0.09	0.29
25	92.02	95.04	94.75	0.30	0.00	59	141.81	157.70	156.95	0.48	0.27
26	92.92	97.26	97.17	0.10	0.75	60	142.54	158.56	157.91	0.41	0.05
27	93.28	97.56	98.00	-0.44	0.68	61	144.75	159.56	159.11	0.28	0.05
28	94.01	98.46	98.24	0.22	**0.92**	62	146.96	160.29	160.28	0.01	0.87
29	94.63	102.52	101.61	0.89	0.24	63	147.72	162.78	162.80	-0.01	0.00
30	96.68	105.95	105.79	0.15	**0.99**	64	148.17	163.70	163.28	0.26	0.05
31	97.46	107.73	107.29	0.41	**0.92**	65	151.47	165.22	165.51	-0.18	0.76
32	98.58	109.00	108.36	0.59	**0.96**	66	152.43	166.74	167.73	-0.59	0.19
33	103.54	111.50	112.14	-0.58	0.86	67	155.52	169.05	169.25	-0.12	0.65
34	105.46	112.92	112.85	0.06	0.47						

4.3.3 Comparison of FEA and EMA results

As mentioned before, a comparison is only considered qualitatively between the FEA and EMA obtained results. Overall, a lot of similarities can be found between the FEA and EMA of the two assemblies A_{112} and A_{220}. In both analyses the SUMACs denote lower effects on the global mode shapes (mode 1 to 8) than on the local mode shapes. On average, both assemblies show larger differences in the sensors at the subframes, than at the sensors on the BIW. This means, that the local differences have a reduced effect in the assembly. Beyond that, both analyses denote roughly the frequency area between 160 Hz and 167 Hz as mostly different between the two assemblies. Apart from this range, a low correlation occurs on different eigenfrequencies in the FEA and EMA, but the global distribution, i.e. that sets of frequencies with high correlation (MAC>0.9) occur between low correlated modes, can be found in both analyses. The maximum deviation in frequency between both assemblies is 0.86% in the FEA and 0.89% in the EMA, which is similar. In the FEA, A_{112} results in slightly higher eigenfrequencies than A_{220} (positive relative difference) below 164 Hz. In the EMA, this is not true for all, but the majority of the modes.

In comparison with the eigenfrequencies of the modal analysis of the BIW alone, the EMA denotes more significant influences than the FEA, i.e. the eigenfrequencies of the assemblies above 70 Hz are significant larger than the eigenfrequencies of the BIW alone. Contrarily, the FEA identifies all modes of the two assemblies at lower frequencies than of the BIW alone. This means, that in the FEA, more mass than stiffeness is added due to the assembly and in the EMA vice versa. It should be mentioned, that the result of the EMA is highly dependent on the mathematical model, i.e. the model order.

4.3.4 Influence in the assembly

The EMA and the FEA both show differences between the two assemblies A_{112} and A_{220}. Differences in the eigenfrequencies of the occuring modes are negligible, but significant differences occur in the mode shapes themselve. The FRFs of the FEA as well as the EMA do not diverge completey at a specific frequency. Rather, they diverge section wise, because high correlated mode shapes appear between non-correlated mode shapes. Both analyses shows differences between the two assemblies at several frequencies between 76 Hz and 160 Hz, in which the free-free analysis of the individual subframes does not point out significant differences (c.f Section 4.2.2). Thus, it is difficult to find reasons for the differences between the two assemblies in this range. Three further analyses are considered to define reasons for the discrepancies. First, the calibration parameters of the two subframes are analysed in more detail, second the influence of (multiple) mounting and last the fixed-interface modes of the two subframes.

Influence of calibration parameters

To motivate differences between the two assemblies, i.e. definition of the parameters of most influence, three modifications of A_{112} are considered in FEAs. First, an adjustment of the rubber stiffnesses between A_{112} and A_{220}, called $A_{112,B}$, second an adjustment of the steel part stiffnesses, denoted with $A_{112,E}$ and last an adjustment of the plate thicknesses denoted with $A_{112,T}$. In all three modifications, the corresponding parameters in A_{112} were exchanged with the parameters of A_{220}, by keeping all other as found in the calibration in Section 4.2.1. Figure 4.14 shows the corresponding sums over all FRFs for all modifications of A_{112} as well as the sum over FRFs for A_{220} between 30 Hz and 170 Hz. It can be seen, that the major differences in the FRFs occur around 70 Hz, 90 Hz to 110 Hz and 130 Hz to 140 Hz. The NRMSEs according to Equation 3.1 are summarized in Table 4.10 for the sum of the FRFs, calculated between A_{220} and the modifications of A_{112}. The NRMSE is largest for $A_{112,B}$, which denotes the best fit to A_{220}. The weakest fit results for $A_{112,E}$. The NRMSE for the original model A_{112} is 0.868, which is lower than for $A_{112,B}$. More important is the correlation of the eigenvectors than the general curve fit. The MAC correlation values, where at least one model shows a MAC<0.98 are as well summarized in Table H.4 and 4.10. Furthermore, the eigenfrequencies of the mode shapes are presented. The results for all 178 modes can be found in Appendix H. In total, $A_{112,B}$ estimates 14 out of 178 modes as low correlated to A_{220}, $A_{112,E}$ estimates 42 and $A_{112,T}$ estimates 54 modes, respectively. As a reminder, A_{112} estimates 22 out of 178 modes as low correlated. Table H.4 and 4.10 show that different mode shapes are affected by the different parameter adjustments. $A_{112,T}$ results in a low correlation between 154 Hz an 168 Hz (Table 4.10), while $A_{112,B}$ and $A_{112,E}$ results in a high correlation for the majority of the modes in this range. $A_{112,E}$ calculates a low correlation for the eigenvectors between 166 Hz and 171 Hz, while $A_{112,B}$ and $A_{112,T}$ calculate mainly a high correlation here. Overall, only three modes exists, i.e. 161, 162 and

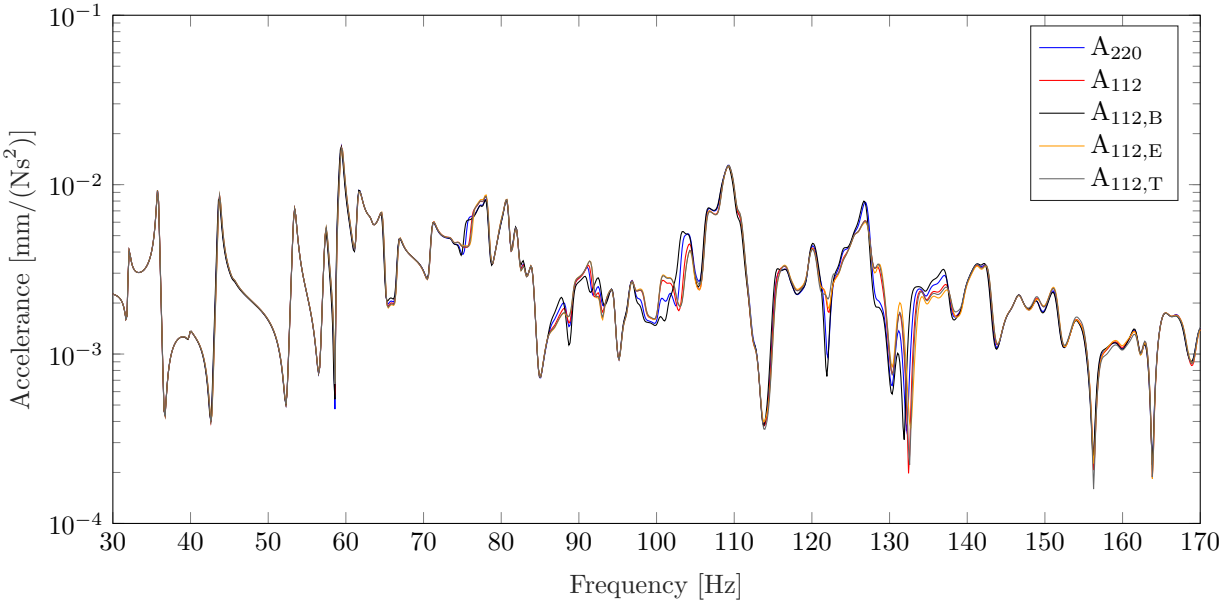

Figure 4.14: *Sum of the FRFs over all channels of A_{220} and all models of A_{112} in the frequency range between 30 Hz and 170 Hz.*

164, where $A_{112,E}$ or $A_{112,T}$ estimate a high correlation but $A_{112,B}$ a low correlation. The relative difference between A_{220} and the three modifications of A_{112} in frequency is negligibly small for all modifications.

Conclusively, the NRMSE, as well as the MAC correlation and the FRFs in Figure 4.14 suggest the model with adjusted rubber stiffnesses $A_{112,B}$ as best correlated to A_{220}. This means, that uncertainties in the stiffness of the bushings, i.e. the interface, have the main influence in the assembly. Another study, which specifies a large influence of the bushing stiffnesses, is the analysis of the mass loaded configuration of the individual subframes in Section 4.2.2. The only difference in the two models are the bushing parameters. Significant differences are visible at frequencies above 140 Hz. If the rubber stiffness is similar, less mode shapes show deviations between the two assemblies, even if thickness and steel properties are different. The adjustments of the steel stiffnesses, $A_{112,E}$, while keeping the differences in the bushing and thickness parameters, leads to even more deviations between the two assemblies than A_{112}. This motivates even more, that the rubber stiffnesses are of high importance, because the mode shapes change significantly by changing the rubber stiffness. The adjustment of the thicknesses $A_{112,T}$ has a negative influence similarly to the steel stiffnesses. The deviation between the two assemblies is larger by adjusting only the thicknesses. These negative effects of adjusting only steel properties and thicknesses, indicate a significant relation to the change of rubber stiffnesses. Figure 4.15 shows addtionally to the NRMSE of the sum of all FRFs, the fit for each single channel according to the NRMSE between A_{220} and all modifications of A_{112}. $A_{220,B}$ shows in the majority of the channels the best and $A_{112,T}$ the worst fit to A_{220}. In 18 out of 56 channels, A_{112} shows a higher fit according to the NRMSE than $A_{112,B}$. The NRMSE results differ between several channels. Channel 31z and 32z indicate significant differences between the four models of A_{112} and channel 17 and 22 indicate small differences.

Influence of mounting

Another study analyzes the influence of multiple coupling of the same subframe. The assembly A_{220} is measured twice, with a complete detachment between the two measurements. Considered is the frequency range between 30 Hz and 100 Hz.

The fit with respect to the NRMSE is 0.827 for the sensors on the subframes of the raw test data. It results in 0.916 for the sensors on the BIW only and in 0.884 for all channels. The corresponding state-space models show a fit of 0.900, 0.926 and 0.913, respectively. Overall, a noticible difference between the two measurements of A_{220} is visible. This means, that the mounting of the subframe influences the dynamic response as well. The mounting was done by hand using a torque wrench, which measures the torque. Further,

Table 4.9: Eigenfrequencies, MAC correlation values and relative differences Δ in frequency between A_{220} and the modifications of A_{112}, i.e. $A_{112,B}$, $A_{112,E}$ and $A_{112,T}$.

# mode	A_{220}	$A_{112,B}$			$A_{112,E}$			$A_{112,T}$		
	f [Hz]	f [Hz]	$\Delta_{112,B}$	MAC	f [Hz]	$\Delta_{112,E}$	MAC	f [Hz]	$\Delta_{112,T}$	MAC
20	74.69	74.65	-0.04	**0.95**	74.72	0.04	**0.93**	74.72	0.03	**0.95**
22	77.44	77.41	-0.03	**0.97**	77.51	0.07	**0.93**	77.48	0.05	**0.96**
24	79.47	79.44	-0.04	**0.97**	79.60	0.12	**0.94**	79.57	0.10	**0.96**
34	88.23	87.96	-0.28	**0.98**	88.36	0.13	0.46	88.35	0.12	0.61
35	88.37	88.37	0.00	**0.97**	88.43	0.06	0.09	88.41	0.04	0.22
43	93.94	93.92	-0.02	**0.99**	93.98	0.04	**0.97**	93.98	0.03	**0.97**
47	97.12	97.08	-0.03	0.89	97.18	0.06	0.82	97.18	0.06	0.85
48	97.21	97.21	-0.01	0.75	97.25	0.03	0.59	97.24	0.03	0.64
49	98.21	98.10	-0.11	**0.98**	98.44	0.23	**0.97**	98.42	0.21	**0.98**
51	101.56	101.54	-0.01	**0.94**	101.57	0.02	**0.92**	101.58	0.02	**0.93**
52	102.32	102.22	-0.11	**0.97**	102.40	0.08	**0.93**	102.40	0.08	**0.93**
53	103.02	102.96	-0.05	**0.96**	103.03	0.01	**0.93**	103.03	0.01	**0.93**
54	103.33	103.11	-0.22	0.89	103.70	0.37	0.68	103.70	0.37	0.65
55	104.01	103.96	-0.04	**0.99**	104.15	0.14	**0.97**	104.15	0.14	**0.97**
57	104.74	104.69	-0.05	**0.99**	104.80	0.06	**0.93**	104.82	0.08	**0.95**
60	107.91	107.91	-0.01	**0.93**	107.92	0.01	**0.92**	107.92	0.01	**0.91**
64	110.26	110.25	-0.01	**0.97**	110.28	0.02	**0.95**	110.28	0.02	**0.94**
81	121.48	121.22	-0.26	**0.91**	121.91	0.43	0.88	122.00	0.52	0.75
82	122.40	122.37	-0.03	**0.93**	122.46	0.06	**0.92**	122.48	0.08	0.83
83	122.62	122.60	-0.02	0.86	122.74	0.12	0.82	122.81	0.19	0.67
87	124.38	124.34	-0.03	**0.96**	124.45	0.08	**0.95**	124.45	0.08	**0.94**
89	125.64	125.59	-0.05	**0.97**	125.69	0.05	**0.96**	125.69	0.05	**0.96**
90	125.94	125.91	-0.03	**0.91**	125.99	0.05	0.88	125.99	0.05	0.88
91	126.30	126.23	-0.07	**0.90**	126.46	0.16	0.88	126.45	0.15	0.89
92	126.93	126.90	-0.03	**0.98**	126.95	0.01	**0.97**	126.94	0.01	**0.98**
93	127.10	126.97	-0.13	0.75	127.25	0.15	0.74	127.23	0.13	0.74
94	127.56	127.36	-0.20	0.80	128.58	1.01	0.47	128.50	0.94	0.75
95	128.62	128.60	-0.02	0.84	128.79	0.17	0.44	128.69	0.08	0.70
96	129.25	129.23	-0.02	**0.98**	129.29	0.03	**0.93**	129.27	0.02	**0.98**
97	130.79	130.76	-0.03	**0.98**	130.90	0.11	**0.95**	130.88	0.09	**0.97**
98	131.25	131.22	-0.03	**0.95**	131.30	0.06	0.88	131.29	0.05	**0.91**
99	131.38	131.34	-0.05	**0.97**	131.48	0.10	**0.94**	131.46	0.08	**0.95**
100	132.00	132.00	0.00	**0.99**	132.01	0.00	**0.97**	132.01	0.00	**0.98**
101	133.03	132.64	-0.39	**0.92**	133.30	0.27	0.31	133.29	0.26	0.69
102	133.34	133.32	-0.01	0.80	133.64	0.31	0.65	133.48	0.15	0.69
108	137.34	137.26	-0.08	0.66	137.38	0.04	0.27	137.37	0.03	0.42
109	137.43	137.39	-0.04	**0.94**	137.51	0.08	0.83	137.50	0.07	**0.90**
110	137.63	137.59	-0.05	**0.93**	137.85	0.21	0.88	137.79	0.16	**0.91**
117	142.58	142.52	-0.06	**0.94**	142.68	0.10	0.74	142.67	0.09	0.77
118	142.73	142.72	-0.01	**0.98**	142.75	0.02	**0.90**	142.75	0.02	**0.90**
119	143.04	143.03	-0.01	**0.99**	143.05	0.01	**0.98**	143.05	0.01	**0.96**
123	146.50	146.49	-0.01	**1.00**	146.53	0.03	**1.00**	146.51	0.01	**0.97**
125	147.51	147.48	-0.03	**1.00**	147.55	0.04	**1.00**	147.49	-0.02	**0.95**
129	149.09	149.07	-0.03	0.60	149.13	0.04	0.08	149.12	0.02	0.81
130	149.13	149.12	0.00	0.06	149.15	0.03	0.03	149.13	0.01	0.29
131	149.55	149.53	-0.02	**0.99**	149.65	0.10	**0.98**	149.61	0.06	**0.96**
132	150.39	150.38	-0.01	**1.00**	150.41	0.02	**0.99**	150.38	-0.01	**0.91**
133	150.99	150.93	-0.06	**0.94**	151.18	0.19	0.82	151.15	0.16	**0.92**

Table 4.10: Eigenfrequencies, MAC correlation values and relative differences Δ in frequency between A_{220} and the modifications of A_{112}, i.e. $A_{112,B}$, $A_{112,E}$ and $A_{112,T}$. Additionally, the fit according to the NRMSE for the sum over all FRFs is shown.

# mode	A_{220}	$A_{112,B}$			$A_{112,E}$			$A_{112,T}$		
	f [Hz]	f [Hz]	$\Delta_{112,B}$	MAC	f [Hz]	$\Delta_{112,E}$	MAC	f [Hz]	$\Delta_{112,T}$	MAC
134	151.28	151.26	-0.02	0.45	151.32	0.04	0.15	151.30	0.02	0.28
135	151.33	151.32	-0.02	**0.93**	151.42	0.09	0.81	151.38	0.05	0.88
136	152.59	152.59	-0.01	**1.00**	152.61	0.02	**0.99**	152.59	0.00	**0.92**
138	154.01	153.99	-0.03	**1.00**	154.04	0.03	**0.99**	154.04	0.03	**0.96**
139	154.16	154.14	-0.02	**0.97**	154.20	0.04	**0.95**	154.18	0.02	0.74
141	154.94	154.93	-0.02	**0.99**	155.02	0.07	**0.99**	154.98	0.04	0.75
142	155.59	155.59	-0.01	**1.00**	155.61	0.01	**1.00**	155.57	-0.02	0.51
143	155.96	155.95	0.00	**1.00**	155.96	0.01	**1.00**	155.95	-0.01	0.81
144	156.71	156.70	-0.02	**1.00**	156.74	0.02	**1.00**	156.52	-0.20	0.07
145	156.98	156.97	0.00	**1.00**	156.98	0.00	**1.00**	156.87	-0.11	0.05
146	157.42	157.40	-0.03	**1.00**	157.49	0.06	**1.00**	156.98	-0.45	0.57
147	158.22	158.21	-0.01	**1.00**	158.24	0.02	**1.00**	157.50	-0.72	0.72
148	158.50	158.49	-0.01	0.64	158.52	0.02	0.61	158.24	-0.26	0.22
149	158.59	158.55	-0.04	**0.97**	158.69	0.10	**0.97**	158.52	-0.08	0.02
150	159.58	159.57	-0.01	**1.00**	159.58	0.00	**1.00**	158.73	-0.85	0.02
151	160.23	160.23	0.00	**1.00**	160.23	0.00	**1.00**	159.59	-0.65	0.00
152	160.65	160.65	0.00	**1.00**	160.65	0.01	**1.00**	160.23	-0.41	0.20
153	161.42	161.41	-0.02	**1.00**	161.48	0.06	**0.99**	160.65	-0.77	0.05
154	161.79	161.78	0.00	**1.00**	161.79	0.00	**1.00**	161.49	-0.30	0.00
155	162.05	162.05	0.00	**1.00**	162.05	0.00	**1.00**	161.79	-0.26	0.48
156	162.61	162.60	-0.01	**1.00**	162.62	0.01	**1.00**	162.05	-0.55	0.40
157	162.70	162.70	0.00	**0.93**	162.71	0.01	0.83	162.62	-0.08	0.05
158	163.20	163.19	-0.01	**1.00**	163.23	0.03	**1.00**	162.71	-0.50	0.09
159	164.35	164.32	-0.03	**0.93**	164.36	0.01	**0.94**	163.23	-1.11	0.57
160	164.50	164.50	-0.01	**0.99**	164.51	0.01	**1.00**	164.37	-0.14	0.38
161	165.05	165.01	-0.04	0.83	165.06	0.01	**0.99**	164.51	-0.54	0.89
162	165.47	165.17	-0.30	0.17	165.50	0.03	**0.92**	165.06	-0.41	0.58
163	166.01	165.56	-0.45	0.02	166.02	0.01	0.83	165.51	-0.50	0.54
164	166.16	166.02	-0.14	0.02	166.16	0.00	**0.94**	166.02	-0.14	0.00
165	166.49	166.16	-0.33	0.04	166.59	0.09	0.03	166.16	-0.33	0.00
166	166.63	166.59	-0.04	0.39	167.08	0.45	0.20	166.59	-0.04	0.08
167	167.30	167.14	-0.16	0.74	168.02	0.71	0.01	167.11	-0.19	0.21
168	167.99	167.96	-0.02	**0.99**	168.13	0.14	0.82	168.03	0.04	**0.97**
169	168.13	168.12	-0.01	0.77	168.73	0.59	0.11	168.14	0.00	0.50
170	168.72	168.72	0.00	**0.97**	169.00	0.28	0.16	168.73	0.01	0.83
171	169.00	169.00	0.00	**1.00**	169.58	0.58	0.00	169.00	0.00	**0.99**
172	169.54	169.53	-0.01	**1.00**	169.61	0.08	0.31	169.57	0.04	**0.99**
173	169.63	169.62	-0.01	**0.94**	170.28	0.65	0.04	169.62	-0.01	0.71
174	170.29	170.29	0.00	**0.99**	170.66	0.37	0.13	170.29	0.00	**0.95**
175	170.69	170.68	0.00	**0.99**	170.73	0.04	0.27	170.68	-0.01	0.86
176	170.74	170.73	0.00	**0.99**	171.14	0.41	0.00	170.73	0.00	**0.93**
177	171.14	171.14	-0.01	**1.00**	171.65	0.50	0.08	171.15	0.00	**0.99**
178	171.62	171.61	-0.01	**0.93**	171.81	0.19	0.04	171.65	0.02	**0.92**
NRMSE		0.898			0.830			0.838		
Δ_{max}		-0.45			1.01			-1.11		

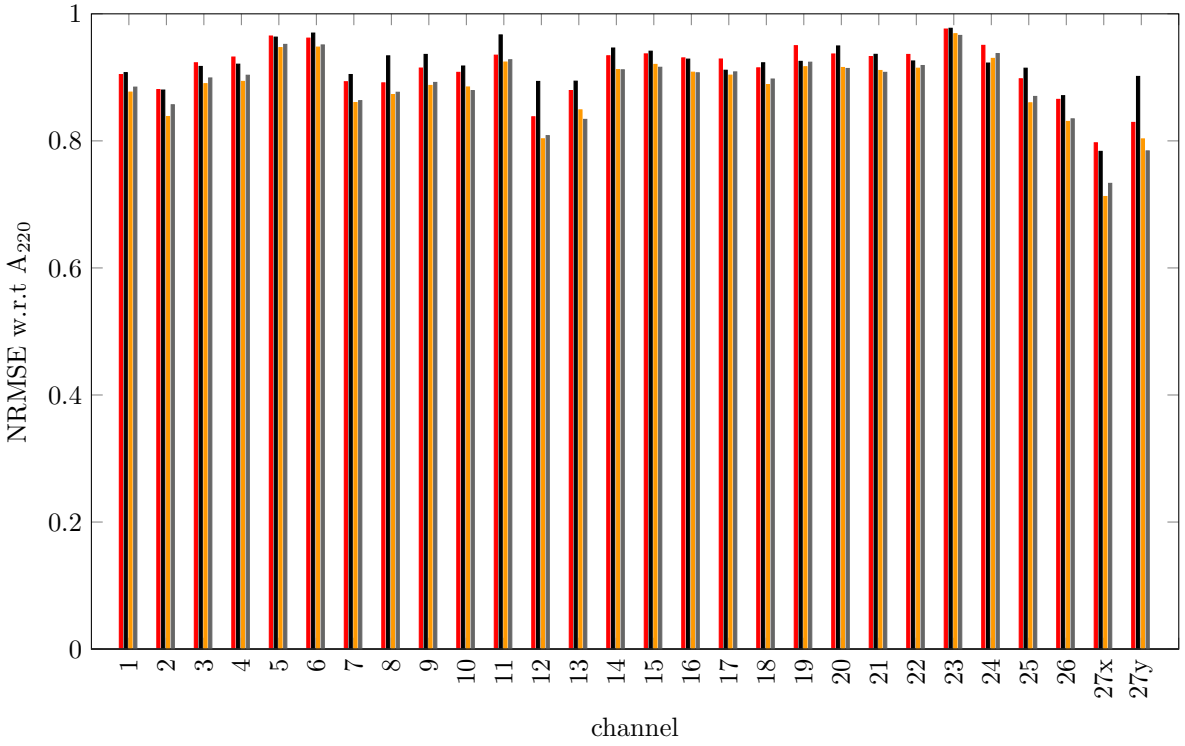

(a) *NRMSE channel 1 to 27y*

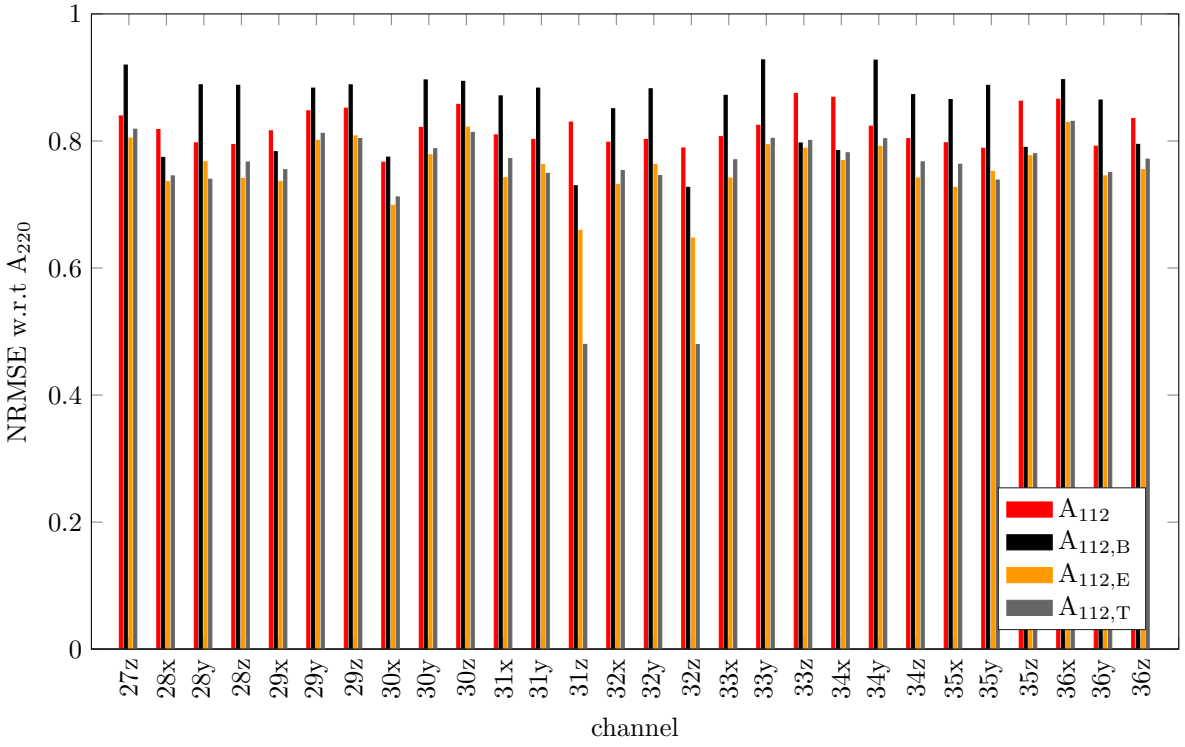

(b) *NRMSE channel 27z to 36z*

Figure 4.15: *NRMSE for all modifications of A_{112}. Red denotes the NRMSE of the original model of A_{112}. Black, yellow and gray the denote the NRMSE for $A_{112,B}$, $A_{112,E}$ and $A_{112,T}$, respectively. (a) shows the first 28 channels and (b) the last 28 channels.*

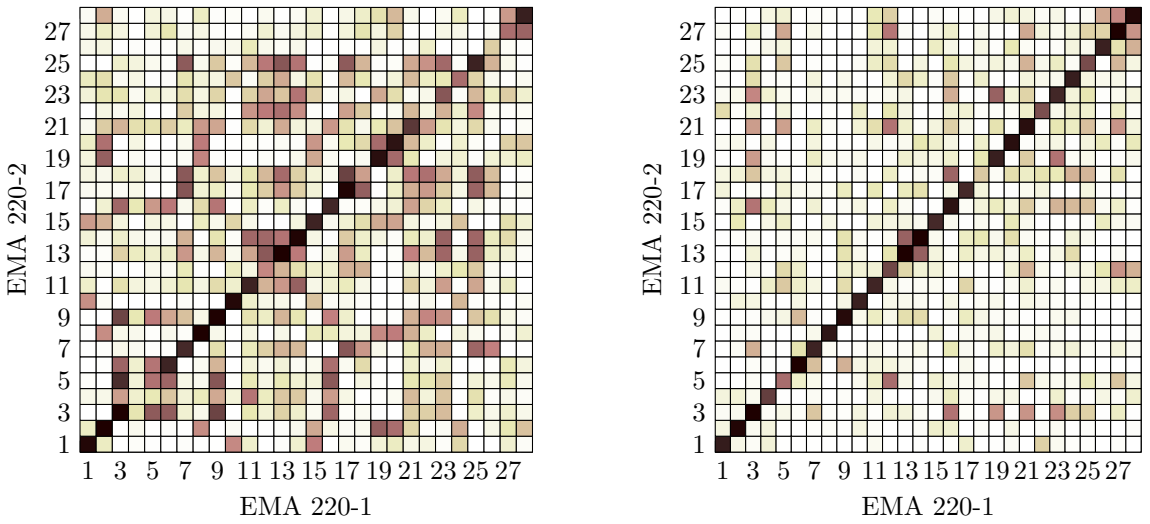

(a) *Sensors on the subframe, i.e. 27 to 56*

(b) *Sensors on the BIW, i.e. 1 to 26*

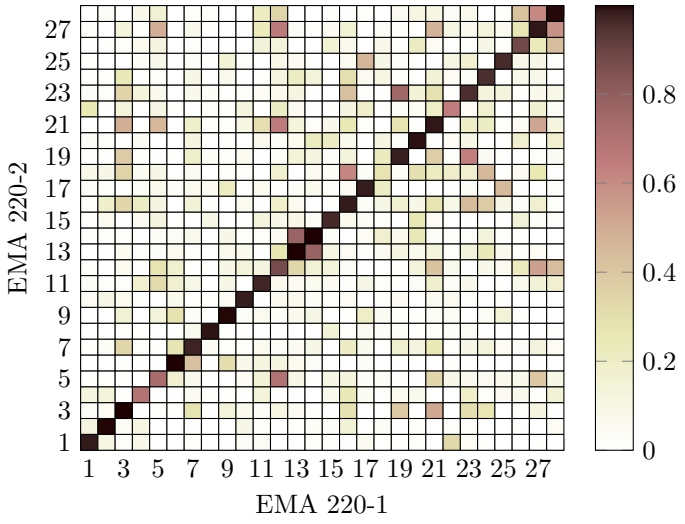

(c) *All sensors*

Figure 4.16: *MAC correlation of the two measurements of A_{220}. (a) shows the MAC for all sensors mounted on the subframe, (b) for all sensors on the BIW and (c) the MAC of the eigenvectors of all available channels.*

the measurements were done at different days, which means that small variances in room temperature, and other influences of the environment are not avoidable. The torque and temperature are in a production line usually more consistent, which guarantees reliability in these two quantities. This would probably reduce the variability in the mounting process. Figure 4.16 shows the MAC between the two measurements of A_{220} for the subframe and BIW channels separately as well as for all channels together. It can be seen, that the channels on the subframe are most uncertain to the mounting process. In total, 10 out of 28 modes below 100 Hz show a low correlation (MAC<0.9). The differences are less noticible in the assembly, indicated by the MAC of all channels and the channels on the BIW. Here, only 6 out of 28 modes are low correlated. Conclusively, the mounting of the assemblies affects the dynamic response as well. The differences in the mode shapes are lower for multiple mounting than between the two assemblies as can be seen in Table 4.8 for the first 28 modes. The fit according to the NRMSE is higher for multiple mounting as well. Thus, effects of multiple mounting may not be neclected, but are less significant than differences in the dynamic properties of nominally indentical subframes.

Table 4.11: Fixed-interface frequencies for the the assemblies A_{220} and all models of A_{112}. Further, the relative difference in % with respect to A_{220} is shown.

# mode	A_{220} f [Hz]	A_{112} f [Hz]	Δ_{112} [%]	$A_{112,B}$ f [Hz]	$\Delta_{112,B}$ [%]	$A_{112,E}$ f [Hz]	$\Delta_{112,E}$ [%]	$A_{112,T}$ f [Hz]	$\Delta_{112,T}$ [%]
1	71.49	72.73	1.74	70.88	-0.85	73.18	2.4	72.93	2.02
2	100.60	101.17	0.56	99.42	-1.18	101.87	1.3	101.66	1.06
3	113.70	114.85	1.01	112.42	-1.13	115.60	1.7	115.44	1.53
4	128.09	130.55	1.91	127.19	-0.70	131.09	2.3	130.95	2.23
5	144.23	145.94	1.18	143.07	-0.81	146.76	1.7	146.34	1.46
6	167.54	166.68	-0.51	166.09	-0.86	173.44	3.5	157.65	-5.90
7	170.19	172.10	1.12	168.48	-1.00	177.23	4.1	172.16	1.15

Influence of fixed-interface modes

Last, the eigenfrequencies of the fixed-interface modes are compared for A_{220} and all four models of A_{112}. Table 4.11 summarizes the frequencies of the fixed-interface modes and shows as well the relative difference to A_{220}. The coupling due to screws in reality is similar to a fixed support at the interface DoFs. If the interface of two parts is not much weaker then the rest of the substructures, the fixed-interface modes occur ususally on higher frequencies than the free-interface modes [AMR14]. Free-interface modes correspond to a free-free analysis such as realized for the subframes and BIW alone. In case of the assemblies of the BIW and the subframes, the coupling, i.e. the rubber is of very low stiffness, which means that the fixed-interface modes are lower than the free-interface modes. The first mode occurs already around 71 Hz and in total 6 modes occur up to 170 Hz. The free-interface modes of the two subframes up to 170 Hz result only in two modes, one around 76 Hz and one around 156 Hz (c.f. Section 4.2.2). The eigenfrequencies of the fixed-interface modes of $A_{112,B}$ results all in a bit lower frequencies than A_{220}. The other models shows for most of the modes higher fixed-interface frequencies than A_{220}. It can be seen, that especially between mode 4 and 7, large differences between A_{220} and $A_{112,E}$ and $A_{112,T}$ occur in the frequencies of the fixed-interface modes. Whereby A_{220} shows between 146 Hz and 173 Hz one mode around 167 Hz and one around 170 Hz, $A_{112,E}$ does not show any mode between 144 Hz and 173 Hz and $A_{112,T}$ a mode around 157 Hz and one around 172 Hz. As mentioned before, the range between 154 Hz and 168 Hz shows large deviations in the eigenvectors of A_{220} and $A_{112,T}$, which means that the large differences in the fixed-interface modes might be the reason for that. A similar behavior might be true for the range 166 Hz to 171 Hz of $A_{112,E}$, where the missing fixed-interface mode result in different eigenvetcors in this frequency range. The two models A_{112} and $A_{112,B}$ show fixed-interface modes at similar frequencies as A_{220}.

5 Discussions

The results presented in Chapter 4 are discussed in this section. Considered are the two types of models, i.e. FE models and experimental models, the calibration of the subframe 112 and findings from the assemblies.

5.1 Models and test setup

This thesis considered two types of models with different analysis types, namely FE and experimental models. Experimental models are mathematical models estimated from raw measurement data. In total, five experimental models were established. These consist of models for the BIW, subframe 111 and 112 as well as for the assemblies A112 and A220. The correlation between FE models and the corresponding experimental models leads to significant differences. Even for the global mode shapes of the BIW alone, the MAC correlation with the state-space model only shows good fits for three modes. For the subframe models, the FE model and experimental model lead to a proper fit up to a frequency of 265 Hz. This proper fit can only be detected after calibration. The nominal model shows a much weaker correlation. In other studies of a modal analysis of a BIW, for instance in [Sch$^+$04], a FE model update was required to adjust the model to experimental results as well. However, a model update of the BIW was not part of this thesis. Generally, a large amount of eigenmodes in the modal analysis makes it difficult to establish appropriate mathematical models. The modal analysis of a BIW shows a lot of modes below 170 Hz. The corresponding FE model detects even more modes than identified by the EMA. For frequencies below 170 Hz, approximately 2.5 times more modes are detected by the simulation model. A lot of these modes occur at almost equal frequencies, i.e. multiple local modes. This indicates a higher resolution of the numerical model compared to the experimental model. In reality, these modes lie so close together that these cannot be separated in the experiment.

Inaccuracies of the experimental models might be caused by the too few accelerometers. Nevertheless, when analyzing the correlation of the same DoF of the FE and experimental model, the result should be independent from the amount of sensors. However, the MAC is a sum over all DoFs. This results in higher deviations when considering a low amount of DoFs. Apart from the low amount of accelerometers, the support of the shaker was not optimal. Due to limitations in the available test equipment, undesired vibrations could not be completely avoided, but only suppressed to a low level. Nevertheless, this could cause small discrepancies in the EMA results. Furthermore, only a limited amount of shaker positions to introduce the excitation were tested because of the lack of appropriate test equipment. During the evaluation of the test setup, three positions were tested. These investigations did not expose large differences.

5.2 Calibration of nominally identical components

Two calibrated FE models of rear subframes are considered in this thesis. Material parameters, such as stiffnesses and thicknesses were updated in a defined frequency range. Thereby includes the FE model of subframe 112 in total seven updated stiffness parameters and subframe 220 ten updated stiffness and one thickness parameter. Important are the differences in the rubber stiffnesses between the two subframes 112 and 220. The FEA of the assembled configuration showed a huge influence of the rubber stiffnesses. Further, in comparison with the corresponding EMA results, the real rubber stiffnesses seem to be more similar between the two subframes, than the model calibration denoted.

5.3 Differences between the two assemblies

Both, the FEA an EMA show negligible differences in frequencies between the two assemblies. The FEA denotes seven succeeding modes around 166 Hz as low or not correlated, at other frequencies below 170 Hz single modes are low correlated. The EMA denotes ten succeeding modes between 156 Hz and 170 Hz as well as low or not correlated, but beyond that a couple of few correlated modes between 130 Hz and 145 Hz. Apart from that, the overall trend of the FEA and EMA shows a similar behavior. Thus, the experiment denotes more siginificant differences above 130 Hz than the FEA. As already mentioned in Section 4.3.4, the mounting of the subframe to the assembly affects the EMA as well. The effects of differences in the mounting are smaller than effects of differences in the dynamic properties, but they might be one quantity, which lead to larger

differences in the EMA than in the FEA. The FEA considers a completely reliable mounting of the assemblies. Another quantity, which could affect the EMA but not the FEA is the test environment, i.e. the temperature. As mentioned in [GA17], the rubber material is temperature dependent. The test room was not temperature controlled, which means differences in temperature during the measuremts of the two assemblies are not excluded.

Finally, to assess the significance of the found differences between the two assemblies is dependent on the field of interest. In this analysis, different mode shapes occur at similar frequencies. It depends on the scope of the investigation, if differences in frequencies or mode shapes are more critical. Such an investigation could be the analysis of noise emission inside or outside the car. The noise does virtually depend on the frequencies of the mode shapes. Another scenario is the transmission of vibrations from the car itself to the passengers. For a comfortable drive, the focus has to be on specific mode shapes rather than on the frequencies. This includes that not necessarily the mode shapes in increasing frequency order are most relevant but rather mode shapes with the largest input to output contribution.

6 Conclusions and future work

The aim of the work was to analyze the influence of variations in nominally identical components in an assembly. This was studied by conducting experiments and simulations. As test specimen two subframes in an assembly with a BIW of a Volvo XC90 (2015) were used. Similar trends as well as differences between both analyses were found.

Overall, three different sources of uncertain parameters that influence the dynamic analysis of assemblies have been found. The influence of multiple mounting, the influence of different material parameters and the influence of fixed-interface modes, which are highly dependent from the material properties at the interface.

In summary, variations in the subframes have a smaller influence on the dynamic response of the assembly with the BIW. The global mode shapes occur at similar frequencies, although differences in the frequencies of local modes were detected. In terms of the eigenvectors, the accomplished analyses show the largest influence on the interface of nominally identical subframe components. In particular, differences occurred due to differences in the rubber bushings. The influence of mounting created uncertainties in the dynamic responses as well. But in comparison to the differences in the interface of two subframes, mounting effects are quite low.

To validate the findings, a calibration of the FE model of the BIW needs to be conducted. Although similar trends were detected in the EMA and FEA, the two groups of analyses correspond to different models of the BIW. Unkown properties affect the dynamic response in one of the models and change the real model behavior. Thus, before analyzing the coupling of two components, both components should be properly validated in their individual dynamic behavior. Furthermore, the accuracy of the EMA might be improved by increasing the amount of sensors and the support of the actuator.

As mentioned before, both analyses denote the eigenmodes around 166 Hz as most differenct between the two assemblies. A detailed analysis of this frequency range, for example in terms of a higher measurement resolution (more frequency lines) or analysis of the fixed-interface mode shapes, i.e. the differences in them, might denote reasons for the large differences in this range.

Bibliography

[Abr12] T. J. S. Abrahamsson. Calibration and Validation of Structural Dynamics Models. *Lecture Notes* (2012).

[AEP13] N. Andreasson, A. Evgrafov, and M. Patriksson. An Introduction to Continuous Optimization. **11.2** (2013), 498.

[AK15] T. J. S. Abrahamsson and D. Kammer. Finite element model calibration using frequency responses with damping equalization. *Mechanical Systems and Signal Processing* **62** (2015), 218–234.

[All02] R. J. Allemang. The Modal Assurance Criterion (MAC): Twenty Years of Use and Abuse. *Conference Proceedings of the Society for Experimental Mechanics Series. 20th IMAC, A Conference on Structural Dynamics* **19.4** (2002), 397–405.

[AMR14] M. Allen, R. L. Mayes, and D. J. Rixen. *Dynamics of Coupled Structures, Volume 1.* Springer International Publishing, 2014. ISBN: 978-3-319-04501-6.

[CK06] R. R. J. Craig and A. Kurdila. *Fundamentals of Structural Dynamics. 2nd Edition.* John Wiley and Sons Inc, 2006. ISBN: 978-0-47143-044-5.

[Ewi00] D. J. Ewins. *Modal Testing: Theory, Practice and Application. 2nd Edition.* Wiley-Blackwell, 2000. ISBN: 978-0-86380-218-8.

[GA17] M. Gibanica and T. J. S. Abrahamsson. Parameter estimation and uncertainty quantification of a subframe with mass loaded bushings. *Proceedings of the 35th IMAC* (2017).

[HTJ09] T. Hastie, R. Tibshirani, and J.Friedman. The Elements of Statistical Learning - Data Mining, Inference, and Prediction. *Springer Series in Statistics* (2009).

[Kam10] D. C. Kammer. Sensor placement for on-orbit modal identification and correlation of large space structures. *Journal of Guidance, Control, and Dynamics* **14.2** (2010), 25–259.

[KRV08] D. de Klerkand, D. Rixen, and S. Voormeeren. General Framework for Dynamic Substructuring: History, Review and Classification of Techniques. *Springer Series in Statistics* **46(5)** (2008), 1169–1181.

[Lev44] K. Levenberg. A method for the solution of certain non-linear problems in least squares. *Quarterly of Applied Mathematics* **2.2** (1944), 164–168.

[MAL96] T. McKelvey, H. Akcay, and L. Ljung. Subspace-based multivariable system identification from frequency response data. *IEEE Transactions on Automatic Control* **41.7** (1996), 960–979.

[Mar63] D. W. Marquardt. An Algorithm for Least-Squares Estimation of Nonlinear Parameters. *Journal of the Society for Industrial and Applied Mathematics* **11.2** (1963), 431–441.

[Mata] Mathworks. *Matlab R2015b Documentation System Identification Toolbox.* URL: `https://ch.mathworks.com/help/pdf_doc/ident/ident_gs.pdf`.

[Matb] Mathworks. *Matlab R2017a Documentation goodnessOfFit.* URL: `https://ch.mathworks.com/help/ident/ref/goodnessoffit.html`.

[MBC00] M. D. Mckay, R. Beckman, and W. Conover. A Comparison of Three Methods for Selecting Values of Input Variables in the Analysis of Output from a Computer Code. *Technometrics* **42.1** (2000), 55–61.

[Mei97] L. Meirovitch. *Principles and techniques of vibrations.* Prentince Hall, 1997. ISBN: 0-02-380141-7.

[Sch+04] C. Schedlinski et al. Experimenatal Modal Analysis and Computational Model Updating of a Car Body in White. *Proceedings of ISMA 2004* (2004).

[Sjo07] P. Sjoevall. Identification and Synthesis of Components for Vibration Transfer Path Analysis. *PhD Thesis* (2007).

[Tec] A. Technologies. *The Fundamentals of Modal Testing. Application Note 243-3.* URL: `http://www.modalshop.com/techlibrary/Fundamentals%5C%20of%5C%20Modal%5C%20Testing.pdf`.

[Vak+17] M. K. Vakilzadeh et al. Stochastic finite element model calibration based on frequency responses and bootstrap sampling. *Mechanical systems and signal processing* **88** (2017), 180–198.

[Val10] P. L. C. van der Valk. Model Reduction & Interface Modeling in Dynamic Substructuring: Application to a multi-megawatt wind turbine. *Msc. Report* (2010).

[Voo09] S. Voormeeren. Structural dynamic modeling of a wind turbine yaw gearbox. *Technical report* (2009).

A Flexible eigenmodes 10 to 15 of the BIW

The FEA of the BIW results in 15 eigenmodes at frequencies below 65.5 Hz. Figure A.1 shows the six occuring modes between 60 Hz and 65.5 Hz. It can be seen that these flexible modes show large local contributions in their mode shapes. For better visibility of the mode shapes, a deformation factor of 20 is applied in the figure. Mode 11, shown in Figure A.1(b) is a mode shape with a high cross-correlation to mode 7.

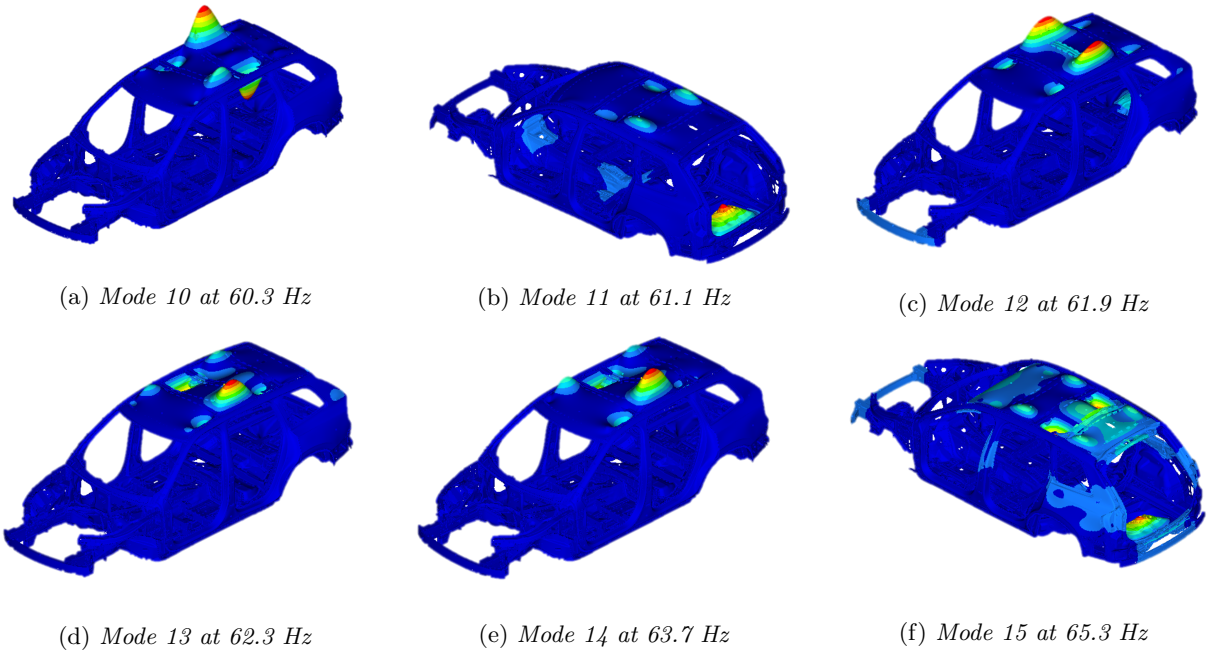

(a) *Mode 10 at 60.3 Hz* (b) *Mode 11 at 61.1 Hz* (c) *Mode 12 at 61.9 Hz*

(d) *Mode 13 at 62.3 Hz* (e) *Mode 14 at 63.7 Hz* (f) *Mode 15 at 65.3 Hz*

Figure A.1: *Flexible eigenmodes between 60 Hz and 65 Hz of the BIW.*

B Flexible eigenmodes of the rear subframe

Figure B.1 shows the first 11 flexible eigenmodes of the nominal subframe of the mass loaded configuration. Figure B.2 shows the same for the configuration without mass loading. They are obtained from [GA17].

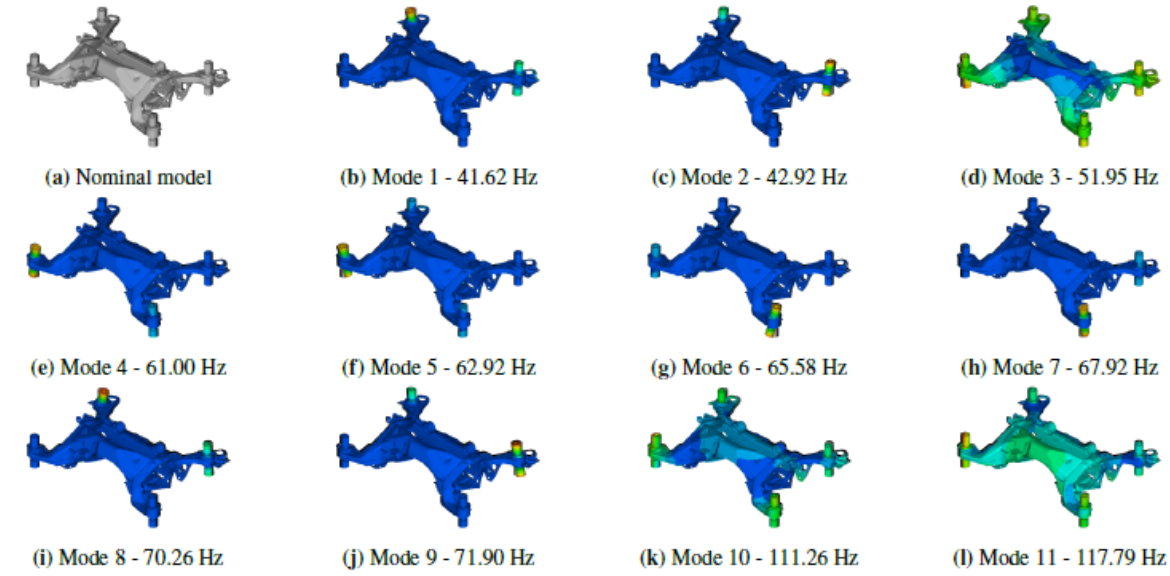

Figure B.1: *Eigenmodes of the mass loaded configuration below 350 Hz [GA17].*

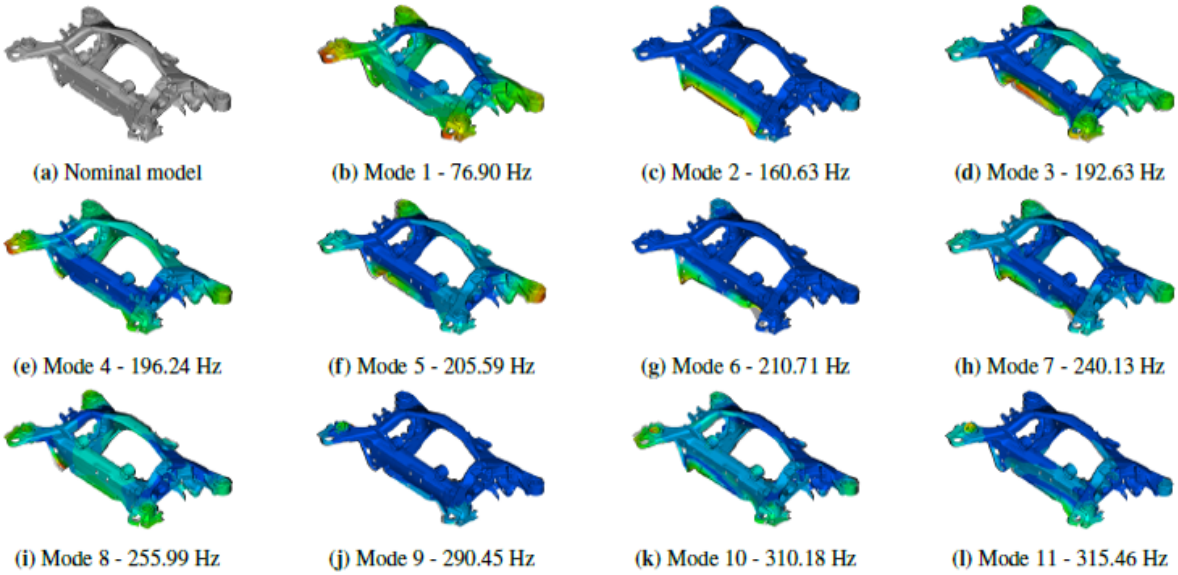

Figure B.2: *Eigenmodes of the configuration without mass loading below 350 Hz [GA17].*

C SUMAC correlation values for the modes 49 to 178 of the assemblies A_{112} and A_{220} in FE coupling

Table C.1: SUMAC correlation values for the modes 49 to 147 of the assemblies A_{112} and A_{220}

# mode	SUMAC A_{112}	SUMAC A_{220}	# mode	SUMAC A_{112}	SUMAC A_{220}	# mode	SUMAC A_{112}	SUMAC A_{220}
49	0.03	0.04	82	0.10	0.07	115	0.00	0.00
50	0.23	0.23	83	0.01	0.08	116	0.06	0.06
51	0.05	0.11	84	0.74	0.68	117	0.00	0.02
52	0.00	0.00	85	0.34	0.35	118	0.06	0.07
53	0.26	0.26	86	0.67	0.69	119	0.01	0.00
54	0.51	0.01	87	0.01	0.06	120	0.03	0.03
55	0.31	0.34	88	0.16	0.16	121	0.05	0.06
56	0.18	0.19	89	0.05	0.03	122	0.16	0.16
57	0.02	0.03	90	0.14	0.17	123	0.02	0.01
58	0.13	0.14	91	0.12	0.04	124	0.22	0.23
59	0.12	0.11	92	0.12	0.12	125	0.19	0.18
60	0.01	0.01	93	0.05	0.02	126	0.04	0.04
61	0.41	0.38	94	0.40	0.13	127	0.03	0.04
62	0.02	0.03	95	0.05	0.08	128	0.04	0.05
63	0.12	0.09	96	0.32	0.31	129	0.23	0.17
64	0.01	0.06	97	0.03	0.01	130	0.11	0.07
65	0.14	0.12	98	0.31	0.35	131	0.03	0.03
66	0.60	0.60	99	0.00	0.00	132	0.18	0.18
67	0.66	0.67	100	0.00	0.00	133	0.09	0.05
68	0.84	0.84	101	0.11	0.04	134	0.04	0.03
69	0.01	0.03	102	0.23	0.44	135	0.02	0.01
70	0.00	0.00	103	0.03	0.04	136	0.21	0.21
71	0.12	0.12	104	0.31	0.26	137	0.76	0.76
72	0.03	0.03	105	0.21	0.19	138	0.03	0.04
73	0.00	0.00	106	0.06	0.07	139	0.08	0.04
74	0.05	0.05	107	0.02	0.02	140	0.07	0.07
75	0.03	0.03	108	0.00	0.02	141	0.03	0.03
76	0.07	0.07	109	0.08	0.10	142	0.01	0.01
77	0.07	0.08	110	0.28	0.14	143	0.02	0.02
78	0.00	0.00	111	0.05	0.04	144	0.09	0.09
79	0.08	0.06	112	0.00	0.00	145	0.44	0.44
80	0.01	0.01	113	0.11	0.09	146	0.03	0.03
81	0.01	0.00	114	0.32	0.30	147	0.00	0.00

Table C.2: SUMAC correlation values for the modes 148 to 178 of the assemblies A_{112} and A_{220}

# mode	SUMAC A_{112}	SUMAC A_{220}	# mode	SUMAC A_{112}	SUMAC A_{220}	# mode	SUMAC A_{112}	SUMAC A_{220}
148	0.00	0.01	159	0.10	0.17	170	0.43	0.43
149	0.00	0.01	160	0.11	0.11	171	0.43	0.43
150	0.02	0.02	161	0.36	0.36	172	0.59	0.56
151	0.05	0.05	162	0.05	0.30	173	0.12	0.09
152	0.09	0.09	163	0.43	0.11	174	0.29	0.29
153	0.41	0.38	164	0.11	0.09	175	0.07	0.07
154	0.02	0.02	165	0.05	0.04	176	0.00	0.00
155	0.43	0.44	166	0.03	0.00	177	0.03	0.03
156	0.75	0.74	167	0.11	0.10	178	0.16	0.24
157	0.08	0.01	168	0.12	0.13			
158	0.07	0.07	169	0.05	0.02			

D Analysis data of the first 178 flexible eigenmodes of the assemblies A_{112} and A_{220} in FE coupling

Table D.1: Eigenfrequencies of the first 88 flexible modes obtained from FEA. The relative difference Δ_A is calculated between A_{112} and A_{220} in %. MAC denotes the correlation of A_{112} and A_{220}.

# mode	BIW	A_{112}	A_{220}	Δ_A	MAC	# mode	BIW	A_{112}	A_{220}	Δ_A	MAC
1	32.12	32.01	32.01	0.00	1.00	45	97.20	95.57	95.55	0.01	1.00
2	36.44	35.82	35.82	0.00	1.00	46	97.75	96.52	96.49	0.03	0.99
3	40.31	39.87	39.86	0.00	1.00	47	99.52	97.17	97.12	0.05	0.89
4	45.35	43.69	43.65	0.03	1.00	48	100.77	97.23	97.21	0.02	0.75
5	45.84	45.53	45.53	0.00	1.00	49	101.74	98.39	98.21	0.18	0.98
6	53.48	53.35	53.35	0.00	1.00	50	102.55	100.43	100.37	0.06	0.99
7	57.71	57.39	57.39	0.00	1.00	51	103.05	101.57	101.56	0.02	0.94
8	58.72	58.77	58.77	0.00	1.00	52	104.22	102.38	102.32	0.06	0.97
9	59.67	59.42	59.38	0.04	1.00	53	104.52	103.02	103.02	0.01	0.96
10	60.29	59.70	59.70	0.00	1.00	54	105.30	103.59	103.33	0.26	0.89
11	61.10	60.21	60.21	0.00	1.00	55	107.06	104.10	104.01	0.09	0.99
12	61.89	61.54	61.54	0.00	1.00	56	107.27	104.67	104.59	0.08	0.99
13	62.35	61.83	61.83	0.01	1.00	57	107.90	104.76	104.74	0.02	0.99
14	63.69	63.33	63.33	0.00	1.00	58	108.17	106.39	106.34	0.05	1.00
15	65.32	64.77	64.75	0.02	1.00	59	109.49	107.15	107.14	0.00	1.00
16	67.21	66.73	66.70	0.03	1.00	60	109.72	107.92	107.91	0.01	0.93
17	71.39	70.91	70.91	0.00	1.00	61	110.16	108.36	108.22	0.13	0.99
18	72.26	71.07	71.06	0.01	1.00	62	110.70	109.41	109.40	0.01	1.00
19	73.79	73.69	73.69	0.00	1.00	63	110.88	109.88	109.87	0.01	1.00
20	74.76	74.72	74.69	0.03	0.95	64	111.99	110.27	110.26	0.01	0.97
21	77.57	76.16	75.56	0.60	0.99	65	112.48	110.77	110.77	0.00	1.00
22	78.49	77.47	77.44	0.04	0.97	66	112.70	110.87	110.87	0.00	1.00
23	79.35	78.21	78.19	0.01	1.00	67	113.12	111.83	111.78	0.05	1.00
24	80.06	79.55	79.47	0.08	0.97	68	113.59	112.28	112.27	0.01	1.00
25	80.84	80.13	80.11	0.02	1.00	69	113.82	112.80	112.79	0.01	0.99
26	81.66	80.83	80.83	0.00	1.00	70	115.28	113.10	113.10	0.00	1.00
27	82.30	81.24	81.21	0.03	1.00	71	116.17	113.77	113.76	0.00	1.00
28	83.45	81.98	81.98	0.01	1.00	72	117.00	115.31	115.27	0.04	1.00
29	83.84	82.92	82.92	0.01	1.00	73	117.50	115.77	115.73	0.05	1.00
30	84.04	83.51	83.50	0.01	1.00	74	119.60	116.19	116.19	0.00	1.00
31	86.08	83.95	83.94	0.00	1.00	75	119.71	116.99	116.99	0.00	1.00
32	86.93	86.20	86.18	0.01	1.00	76	120.16	117.68	117.66	0.02	1.00
33	88.29	86.63	86.63	0.01	1.00	77	120.48	119.37	119.28	0.09	0.99
34	88.89	88.29	88.23	0.06	0.98	78	122.25	119.63	119.61	0.03	1.00
35	89.46	88.38	88.37	0.01	0.97	79	122.43	120.15	120.14	0.01	1.00
36	89.79	89.26	89.25	0.01	1.00	80	123.71	120.59	120.57	0.02	1.00
37	90.48	89.77	89.77	0.00	1.00	81	124.10	121.86	121.48	0.39	0.91
38	92.82	90.39	90.38	0.01	1.00	82	124.12	122.45	122.40	0.04	0.93
39	93.35	91.52	91.37	0.15	1.00	83	124.24	122.72	122.62	0.11	0.86
40	93.61	92.73	92.71	0.02	1.00	84	125.21	123.89	123.86	0.03	0.99
41	93.91	93.10	93.02	0.08	0.99	85	125.72	124.07	124.07	0.00	1.00
42	94.50	93.52	93.52	0.00	1.00	86	125.87	124.13	124.13	0.00	1.00
43	95.55	93.96	93.94	0.02	0.99	87	126.18	124.44	124.38	0.06	0.96
44	96.70	94.50	94.49	0.01	1.00	88	126.88	125.34	125.31	0.02	1.00

Table D.2: Eigenfrequencies of mode 89 to 178 obtained from FEA. The relative difference Δ_A is calculated between A_{112} and A_{220} in %. MAC denotes the correlation of A_{112} and A_{220}.

# mode	BIW	A_{112}	A_{220}	Δ_A	MAC	# mode	BIW	A_{112}	A_{220}	Δ_A	MAC
89	127.42	125.68	125.64	0.04	0.97	134	154.66	151.30	151.28	0.02	0.45
90	128.13	125.99	125.94	0.04	0.91	135	154.81	151.37	151.33	0.04	0.93
91	129.26	126.44	126.30	0.14	0.90	136	155.42	152.60	152.59	0.01	1.00
92	130.23	126.94	126.93	0.01	0.98	137	155.91	152.96	152.95	0.01	1.00
93	130.96	127.22	127.10	0.12	0.75	138	156.55	154.03	154.01	0.02	1.00
94	131.06	128.42	127.56	0.86	0.80	139	156.97	154.18	154.16	0.03	0.97
95	132.00	128.66	128.62	0.05	0.84	140	157.43	154.84	154.84	0.00	1.00
96	133.28	129.27	129.25	0.02	0.98	141	157.99	155.00	154.94	0.05	0.99
97	133.72	130.87	130.79	0.08	0.98	142	158.32	155.60	155.59	0.00	1.00
98	134.59	131.29	131.25	0.04	0.95	143	158.48	155.96	155.96	0.00	1.00
99	135.80	131.44	131.38	0.06	0.97	144	159.52	156.72	156.71	0.01	1.00
100	136.02	132.00	132.00	0.00	0.99	145	160.23	156.98	156.98	0.00	1.00
101	136.14	133.25	133.03	0.22	0.92	146	160.65	157.48	157.42	0.05	1.00
102	136.23	133.40	133.34	0.06	0.80	147	161.19	158.24	158.22	0.02	1.00
103	137.11	134.43	134.40	0.03	0.99	148	161.81	158.52	158.50	0.01	0.64
104	137.40	135.01	134.96	0.05	1.00	149	162.03	158.68	158.59	0.08	0.97
105	138.56	135.84	135.84	0.01	1.00	150	162.58	159.58	159.58	0.00	1.00
106	139.24	136.12	136.11	0.01	1.00	151	162.72	160.23	160.23	0.00	1.00
107	140.00	136.16	136.16	0.00	1.00	152	163.16	160.65	160.65	0.01	1.00
108	141.07	137.36	137.34	0.02	0.66	153	164.28	161.45	161.42	0.03	1.00
109	141.36	137.49	137.43	0.05	0.94	154	164.48	161.79	161.79	0.00	1.00
110	141.65	137.75	137.63	0.11	0.93	155	165.01	162.05	162.05	0.00	1.00
111	141.75	139.12	139.11	0.01	0.99	156	165.45	162.61	162.61	0.01	1.00
112	142.72	139.51	139.47	0.04	1.00	157	166.00	162.70	162.70	0.00	0.93
113	142.94	140.86	140.82	0.05	0.99	158	166.14	163.22	163.20	0.01	1.00
114	143.22	141.36	141.36	0.00	1.00	159	166.57	164.33	164.35	-0.02	0.93
115	143.57	141.58	141.58	0.01	1.00	160	166.78	164.50	164.50	-0.01	0.99
116	145.37	141.73	141.73	0.00	1.00	161	167.62	165.03	165.05	-0.02	0.83
117	145.98	142.65	142.58	0.08	0.94	162	168.21	165.26	165.47	-0.21	0.17
118	146.73	142.74	142.73	0.01	0.98	163	168.72	165.62	166.01	-0.39	0.02
119	147.04	143.04	143.04	0.00	0.99	164	168.92	166.03	166.16	-0.13	0.02
120	147.79	143.23	143.23	0.00	1.00	165	169.18	166.16	166.49	-0.33	0.04
121	148.12	144.37	144.35	0.03	1.00	166	169.53	166.59	166.63	-0.04	0.39
122	148.58	145.39	145.39	0.00	1.00	167	170.27	167.19	167.30	-0.12	0.74
123	148.77	146.52	146.50	0.02	1.00	168	170.65	168.02	167.99	0.03	0.99
124	149.08	146.85	146.84	0.01	1.00	169	170.70	168.15	168.13	0.02	0.77
125	149.20	147.52	147.51	0.01	1.00	170	170.98	168.73	168.72	0.01	0.97
126	149.76	148.05	148.05	0.00	1.00	171	171.40	169.00	169.00	0.00	1.00
127	150.22	148.67	148.65	0.02	1.00	172	171.80	169.57	169.54	0.04	1.00
128	151.03	148.72	148.70	0.02	0.99	173	172.39	169.63	169.63	0.00	0.94
129	151.25	149.13	149.09	0.03	0.60	174	172.56	170.29	170.29	0.00	0.99
130	152.35	149.14	149.13	0.01	0.06	175	172.77	170.69	170.69	0.00	0.99
131	152.81	149.62	149.55	0.07	0.99	176	173.59	170.74	170.74	0.00	0.99
132	153.37	150.40	150.39	0.01	1.00	177	174.16	171.14	171.14	0.00	1.00
133	153.96	151.14	150.99	0.16	0.94	178	174.66	171.65	171.62	0.03	0.93

E Sum over FRFs of BIW and subframe sensors in FE coupling

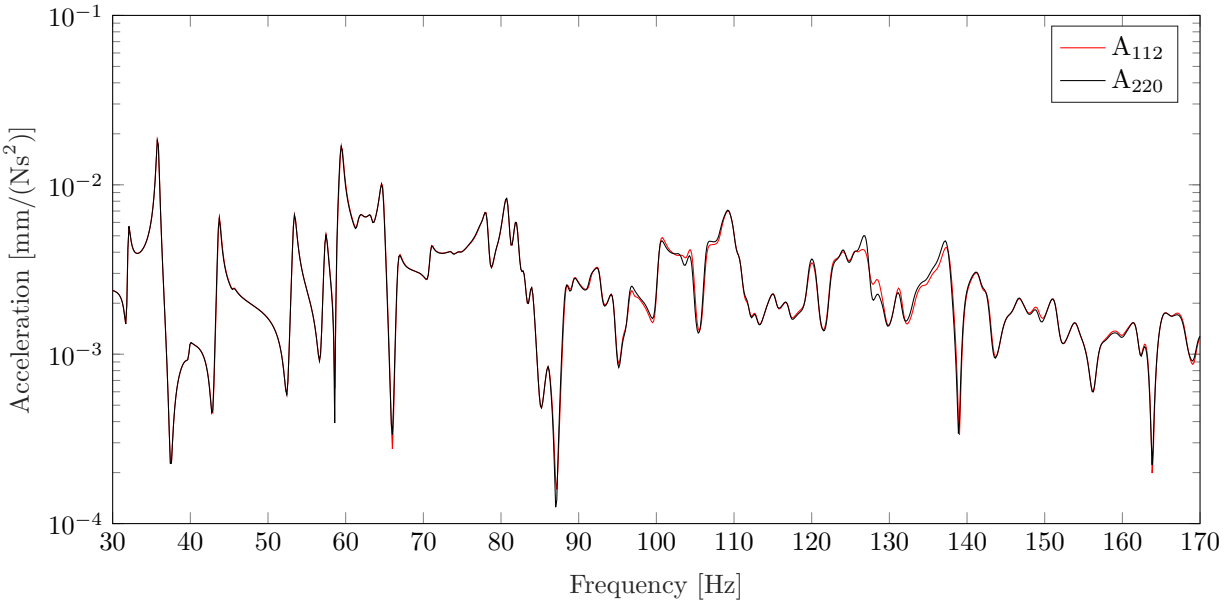

(a) *FRFs on the BIW*

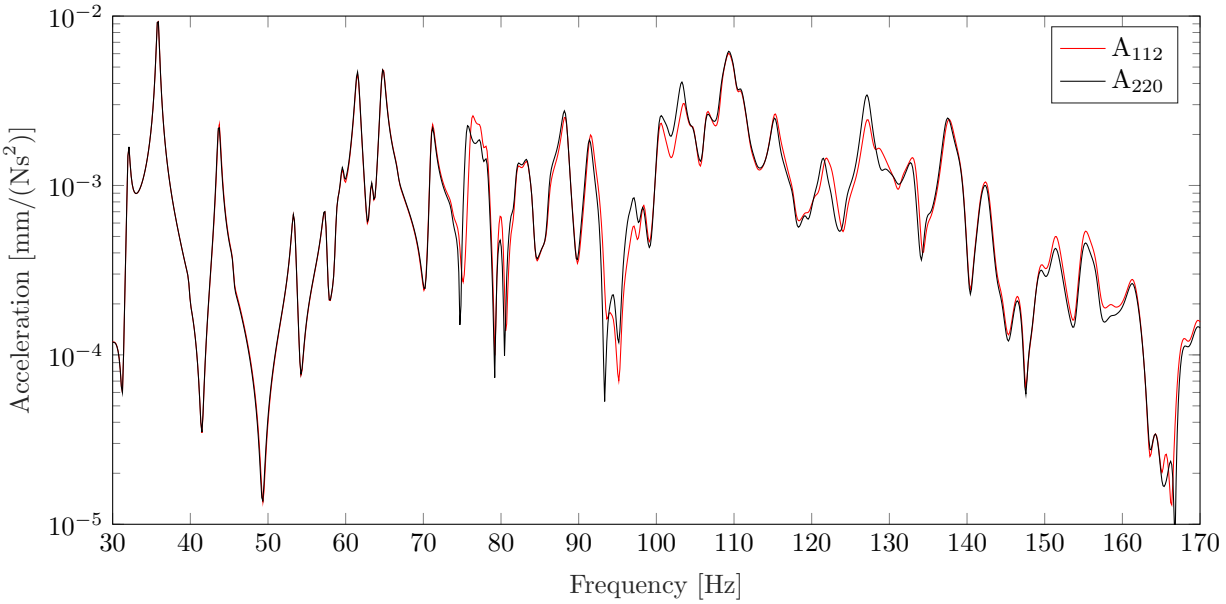

(b) *FRFs on the subframe*

Figure E.1: *Sum over FRFs between 30 Hz and 170 Hz. (a) channels that are placed on the BIW. (b) channels that are placed on the subframe.*

F SUMAC correlation values for the modes 30 to 67 of the assemblies A_{112} and A_{220} in EMA coupling

Table F.1: SUMAC correlation values for the modes 30 to 67 of the assemblies A_{112} and A_{220}

# mode	SUMAC A_{112}	SUMAC A_{220}	# mode	SUMAC A_{112}	SUMAC A_{220}	# mode	SUMAC A_{112}	SUMAC A_{220}
30(31)	0.09	0.11	43(44)	0.02	0.27	56(57)	0.09	0.15
31(32)	0.08	0.05	44(45)	0.04	0.00	57(58)	0.03	0.02
32(33)	0.14	0.03	45(46)	0.00	0.05	58(59)	0.00	0.02
33(34)	0.61	0.75	46(47)	0.30	0.44	59(60)	0.09	0.07
34(35)	0.14	0.33	47(48)	0.03	0.01	60(61)	0.01	0.34
35(36)	0.04	0.01	48(49)	0.02	0.06	61(62)	0.04	0.18
36(37)	0.05	0.20	49(50)	0.04	0.02	62(63)	0.02	0.01
37(38)	0.16	0.24	50(51)	0.44	0.01	63(64)	0.04	0.00
38(39)	0.16	0.17	51(52)	0.00	0.00	64(65)	0.15	0.43
39(40)	0.01	0.46	52(53)	0.04	0.09	65(66)	0.11	0.02
40(41)	0.00	0.01	53(54)	0.60	0.45	66(67)	0.33	0.51
41(42)	0.50	0.51	54(55)	0.31	0.32	67(68)	0.07	0.02
42(43)	0.00	0.05	55(56)	0.21	0.25			

G Sum over FRFs of BIW and subframe sensors in EMA coupling

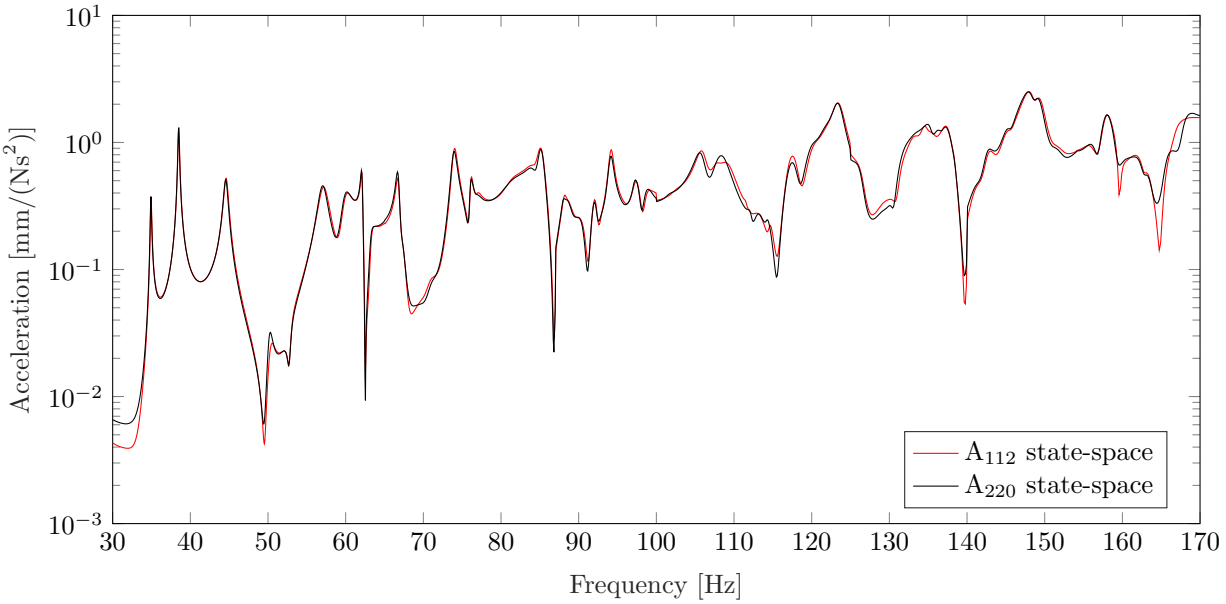

(a) *FRFs on the BIW*

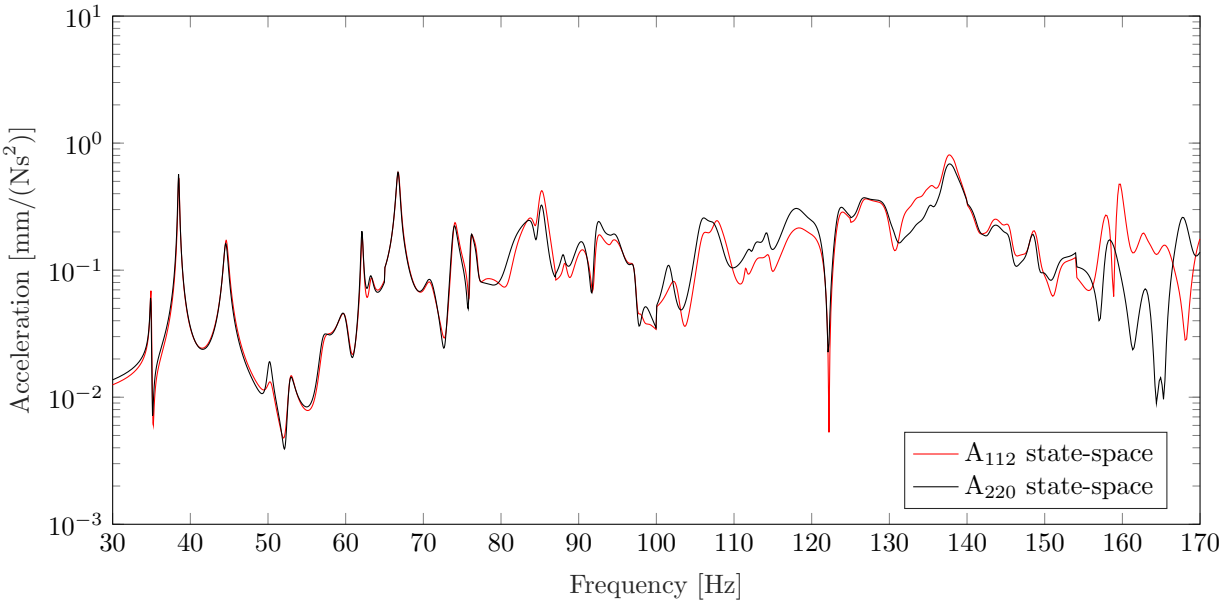

(b) *FRFs on the subframe*

Figure G.1: *Sum over FRFs between 30 Hz and 170 Hz. (a) channels that are placed on the BIW. (b) channels that are placed on the subframe.*

H Analysis data of the first 178 flexible eigenmodes of A_{220} and the modifications of A_{112}, i.e. $A_{112,B}$, $A_{112,E}$ and $A_{112,T}$ in FE coupling

Table H.1: Eigenfrequencies, MAC correlation values and relative differences Δ in frequency between A_{220} and the modifications of A_{112}, i.e. $A_{112,B}$, $A_{112,E}$ and $A_{112,T}$.

# mode	A_{220}	$A_{112,B}$			$A_{112,E}$			$A_{112,T}$		
	f [Hz]	f [Hz]	$\Delta_{112,B}$	MAC	f [Hz]	$\Delta_{112,E}$	MAC	f [Hz]	$\Delta_{112,T}$	MAC
1	32.01	32.01	0.00	1.00	32.01	0.00	1.00	32.01	0.00	1.00
2	35.82	35.82	0.00	1.00	35.82	0.00	1.00	35.83	0.00	1.00
3	39.86	39.86	-0.01	1.00	39.87	0.01	1.00	39.87	0.01	1.00
4	43.65	43.62	-0.04	1.00	43.71	0.05	1.00	43.70	0.05	1.00
5	45.53	45.53	0.00	1.00	45.53	0.00	1.00	45.53	0.00	1.00
6	53.35	53.34	0.00	1.00	53.35	0.00	1.00	53.35	0.00	1.00
7	57.39	57.37	-0.01	1.00	57.39	0.01	1.00	57.40	0.01	1.00
8	58.77	58.77	0.00	1.00	58.77	0.00	1.00	58.77	0.00	1.00
9	59.38	59.35	-0.04	1.00	59.44	0.06	1.00	59.44	0.05	1.00
10	59.70	59.69	0.00	1.00	59.70	0.00	1.00	59.70	0.00	1.00
11	60.21	60.21	0.00	1.00	60.21	0.00	1.00	60.22	0.00	1.00
12	61.54	61.53	-0.01	1.00	61.54	0.01	1.00	61.55	0.01	1.00
13	61.83	61.82	0.00	1.00	61.84	0.01	1.00	61.83	0.01	1.00
14	63.33	63.33	0.00	1.00	63.33	0.00	1.00	63.33	0.00	1.00
15	64.75	64.71	-0.04	1.00	64.79	0.04	1.00	64.79	0.03	1.00
16	66.70	66.68	-0.02	1.00	66.74	0.05	1.00	66.73	0.04	1.00
17	70.91	70.90	-0.02	1.00	70.92	0.01	1.00	70.92	0.01	1.00
18	71.06	71.04	-0.02	1.00	71.08	0.02	1.00	71.08	0.02	1.00
19	73.69	73.69	0.00	1.00	73.69	0.00	1.00	73.69	0.00	1.00
20	74.69	74.65	-0.04	0.95	74.72	0.04	0.93	74.72	0.03	0.95
21	75.56	75.24	-0.32	0.99	76.39	0.83	0.98	76.26	0.70	0.99
22	77.44	77.41	-0.03	0.97	77.51	0.07	0.93	77.48	0.05	0.96
23	78.19	78.17	-0.02	1.00	78.23	0.03	0.99	78.22	0.02	1.00
24	79.47	79.44	-0.04	0.97	79.60	0.12	0.94	79.57	0.10	0.96
25	80.11	80.10	-0.01	1.00	80.15	0.04	0.99	80.13	0.03	0.99
26	80.83	80.82	0.00	1.00	80.83	0.00	1.00	80.83	0.00	1.00
27	81.21	81.20	-0.01	1.00	81.24	0.04	1.00	81.24	0.03	1.00
28	81.98	81.97	0.00	1.00	81.99	0.01	1.00	81.99	0.01	1.00
29	82.92	82.89	-0.03	1.00	82.93	0.02	1.00	82.93	0.02	1.00
30	83.50	83.49	-0.02	1.00	83.52	0.01	1.00	83.52	0.01	1.00
31	83.94	83.94	0.00	1.00	83.95	0.00	1.00	83.95	0.00	1.00
32	86.18	86.18	-0.01	1.00	86.20	0.02	1.00	86.20	0.02	1.00
33	86.63	86.63	0.00	1.00	86.64	0.01	1.00	86.64	0.01	1.00
34	88.23	87.96	-0.28	0.98	88.36	0.13	0.46	88.35	0.12	0.61
35	88.37	88.37	0.00	0.97	88.43	0.06	0.09	88.41	0.04	0.22
36	89.25	89.24	-0.01	1.00	89.26	0.01	1.00	89.26	0.01	1.00
37	89.77	89.75	-0.02	1.00	89.78	0.01	0.98	89.78	0.01	0.98
38	90.38	90.32	-0.06	1.00	90.41	0.03	0.99	90.41	0.03	0.99
39	91.37	91.09	-0.28	1.00	91.69	0.33	0.99	91.69	0.32	0.99
40	92.71	92.70	-0.01	1.00	92.73	0.02	1.00	92.74	0.03	1.00

Table H.2: Eigenfrequencies, MAC correlation values and relative differences Δ in frequency between A_{220} and the modifications of A_{112}, i.e. $A_{112,B}$, $A_{112,E}$ and $A_{112,T}$.

# mode	A_{220}	$A_{112,B}$			$A_{112,E}$			$A_{112,T}$		
	f [Hz]	f [Hz]	$\Delta_{112,B}$	MAC	f [Hz]	$\Delta_{112,E}$	MAC	f [Hz]	$\Delta_{112,T}$	MAC
41	93.02	92.93	-0.08	0.99	93.16	0.15	0.98	93.14	0.12	0.98
42	93.52	93.51	0.00	1.00	93.52	0.00	0.99	93.52	0.00	1.00
43	93.94	93.92	-0.02	0.99	93.98	0.04	0.97	93.98	0.03	0.97
44	94.49	94.49	0.00	1.00	94.50	0.01	1.00	94.50	0.01	1.00
45	95.55	95.55	0.00	1.00	95.57	0.02	1.00	95.57	0.01	1.00
46	96.49	96.47	-0.02	0.99	96.53	0.04	0.99	96.52	0.03	0.99
47	97.12	97.08	-0.03	0.89	97.18	0.06	0.82	97.18	0.06	0.85
48	97.21	97.21	-0.01	0.75	97.25	0.03	0.59	97.24	0.03	0.64
49	98.21	98.10	-0.11	0.98	98.44	0.23	0.97	98.42	0.21	0.98
50	100.37	100.28	-0.09	0.99	100.46	0.09	0.98	100.46	0.09	0.98
51	101.56	101.54	-0.01	0.94	101.57	0.02	0.92	101.58	0.02	0.93
52	102.32	102.22	-0.11	0.97	102.40	0.08	0.93	102.40	0.08	0.93
53	103.02	102.96	-0.05	0.96	103.03	0.01	0.93	103.03	0.01	0.93
54	103.33	103.11	-0.22	0.89	103.70	0.37	0.68	103.70	0.37	0.65
55	104.01	103.96	-0.04	0.99	104.15	0.14	0.97	104.15	0.14	0.97
56	104.59	104.55	-0.04	0.99	104.70	0.11	0.99	104.71	0.12	0.99
57	104.74	104.69	-0.05	0.99	104.80	0.06	0.93	104.82	0.08	0.95
58	106.34	106.28	-0.06	1.00	106.40	0.07	1.00	106.43	0.09	0.99
59	107.14	107.14	0.00	1.00	107.15	0.00	1.00	107.15	0.00	1.00
60	107.91	107.91	-0.01	0.93	107.92	0.01	0.92	107.92	0.01	0.91
61	108.22	108.17	-0.05	0.99	108.38	0.16	0.99	108.40	0.17	0.98
62	109.40	109.37	-0.03	1.00	109.42	0.02	1.00	109.42	0.02	0.99
63	109.87	109.85	-0.02	1.00	109.89	0.02	1.00	109.89	0.02	0.99
64	110.26	110.25	-0.01	0.97	110.28	0.02	0.95	110.28	0.02	0.94
65	110.77	110.76	-0.01	1.00	110.78	0.01	0.98	110.78	0.01	0.98
66	110.87	110.85	-0.02	1.00	110.89	0.02	0.99	110.89	0.02	0.99
67	111.78	111.76	-0.02	1.00	111.83	0.06	1.00	111.84	0.06	1.00
68	112.27	112.26	-0.01	1.00	112.29	0.02	1.00	112.28	0.01	1.00
69	112.79	112.78	-0.01	0.99	112.81	0.02	0.99	112.80	0.02	0.99
70	113.10	113.09	-0.01	1.00	113.10	0.01	1.00	113.10	0.01	1.00
71	113.76	113.75	-0.01	1.00	113.77	0.01	1.00	113.77	0.01	1.00
72	115.27	115.17	-0.10	1.00	115.35	0.08	0.98	115.34	0.07	0.98
73	115.73	115.63	-0.09	1.00	115.85	0.12	0.98	115.85	0.12	0.98
74	116.19	116.18	-0.01	1.00	116.19	0.01	0.99	116.19	0.01	0.99
75	116.99	116.99	0.00	1.00	116.99	0.00	1.00	116.99	0.00	1.00
76	117.66	117.64	-0.01	1.00	117.68	0.03	0.99	117.68	0.02	0.99
77	119.28	119.22	-0.07	0.99	119.38	0.10	0.99	119.40	0.12	0.99
78	119.61	119.60	-0.01	1.00	119.64	0.03	1.00	119.64	0.03	1.00
79	120.14	120.14	0.00	1.00	120.15	0.01	0.99	120.15	0.01	0.99
80	120.57	120.56	-0.01	1.00	120.60	0.03	1.00	120.59	0.02	1.00
81	121.48	121.22	-0.26	0.91	121.91	0.43	0.88	122.00	0.52	0.75
82	122.40	122.37	-0.03	0.93	122.46	0.06	0.92	122.48	0.08	0.83
83	122.62	122.60	-0.02	0.86	122.74	0.12	0.82	122.81	0.19	0.67
84	123.86	123.84	-0.02	0.99	123.90	0.04	0.99	123.90	0.04	0.98
85	124.07	124.06	0.00	1.00	124.07	0.00	1.00	124.07	0.00	1.00

Table H.3: Eigenfrequencies, MAC correlation values and relative differences Δ in frequency between A_{220} and the modifications of A_{112}, i.e. $A_{112,B}$, $A_{112,E}$ and $A_{112,T}$.

# mode	A_{220}	$A_{112,B}$			$A_{112,E}$			$A_{112,T}$		
	f [Hz]	f [Hz]	$\Delta_{112,B}$	MAC	f [Hz]	$\Delta_{112,E}$	MAC	f [Hz]	$\Delta_{112,T}$	MAC
86	124.13	124.13	0.00	1.00	124.13	0.00	1.00	124.13	0.00	0.99
87	124.38	124.34	-0.03	0.96	124.45	0.08	0.95	124.45	0.08	0.94
88	125.31	125.30	-0.02	1.00	125.34	0.03	1.00	125.36	0.05	1.00
89	125.64	125.59	-0.05	0.97	125.69	0.05	0.96	125.69	0.05	0.96
90	125.94	125.91	-0.03	0.91	125.99	0.05	0.88	125.99	0.05	0.88
91	126.30	126.23	-0.07	0.90	126.46	0.16	0.88	126.45	0.15	0.89
92	126.93	126.90	-0.03	0.98	126.95	0.01	0.97	126.94	0.01	0.98
93	127.10	126.97	-0.13	0.75	127.25	0.15	0.74	127.23	0.13	0.74
94	127.56	127.36	-0.20	0.80	128.58	1.01	0.47	128.50	0.94	0.75
95	128.62	128.60	-0.02	0.84	128.79	0.17	0.44	128.69	0.08	0.70
96	129.25	129.23	-0.02	0.98	129.29	0.03	0.93	129.27	0.02	0.98
97	130.79	130.76	-0.03	0.98	130.90	0.11	0.95	130.88	0.09	0.97
98	131.25	131.22	-0.03	0.95	131.30	0.06	0.88	131.29	0.05	0.91
99	131.38	131.34	-0.05	0.97	131.48	0.10	0.94	131.46	0.08	0.95
100	132.00	132.00	0.00	0.99	132.01	0.00	0.97	132.01	0.00	0.98
101	133.03	132.64	-0.39	0.92	133.30	0.27	0.31	133.29	0.26	0.69
102	133.34	133.32	-0.01	0.80	133.64	0.31	0.65	133.48	0.15	0.69
103	134.40	134.37	-0.03	0.99	134.44	0.05	0.98	134.43	0.04	0.99
104	134.96	134.92	-0.04	1.00	135.04	0.09	0.99	135.03	0.07	0.99
105	135.84	135.84	0.00	1.00	135.85	0.01	0.99	135.84	0.01	0.99
106	136.11	136.10	0.00	1.00	136.12	0.02	1.00	136.12	0.01	1.00
107	136.16	136.16	0.00	1.00	136.16	0.00	1.00	136.16	0.00	1.00
108	137.34	137.26	-0.08	0.66	137.38	0.04	0.27	137.37	0.03	0.42
109	137.43	137.39	-0.04	0.94	137.51	0.08	0.83	137.50	0.07	0.90
110	137.63	137.59	-0.05	0.93	137.85	0.21	0.88	137.79	0.16	0.91
111	139.11	139.10	-0.01	0.99	139.13	0.02	0.98	139.12	0.01	0.99
112	139.47	139.45	-0.02	1.00	139.53	0.06	0.99	139.51	0.04	1.00
113	140.82	140.80	-0.02	0.99	140.89	0.07	0.99	140.87	0.05	0.99
114	141.36	141.36	0.00	1.00	141.36	0.00	1.00	141.36	0.00	1.00
115	141.58	141.56	-0.02	1.00	141.59	0.02	1.00	141.59	0.02	1.00
116	141.73	141.72	0.00	1.00	141.73	0.00	1.00	141.73	0.00	0.99
117	142.58	142.52	-0.06	0.94	142.68	0.10	0.74	142.67	0.09	0.77
118	142.73	142.72	-0.01	0.98	142.75	0.02	0.90	142.75	0.02	0.90
119	143.04	143.03	-0.01	0.99	143.05	0.01	0.98	143.05	0.01	0.96
120	143.23	143.23	0.00	1.00	143.23	0.00	1.00	143.23	0.00	1.00
121	144.35	144.29	-0.06	1.00	144.42	0.08	0.99	144.39	0.04	0.99
122	145.39	145.39	0.00	1.00	145.39	0.00	1.00	145.39	0.00	1.00
123	146.50	146.49	-0.01	1.00	146.53	0.03	1.00	146.51	0.01	0.97
124	146.84	146.84	0.00	1.00	146.85	0.01	1.00	146.85	0.01	1.00
125	147.51	147.48	-0.03	1.00	147.55	0.04	1.00	147.49	-0.02	0.95
126	148.05	148.04	-0.01	1.00	148.06	0.01	1.00	148.05	0.00	1.00
127	148.65	148.64	-0.02	1.00	148.69	0.03	1.00	148.66	0.01	0.98
128	148.70	148.70	0.00	0.99	148.73	0.02	0.99	148.72	0.02	1.00
129	149.09	149.07	-0.03	0.60	149.13	0.04	0.08	149.12	0.02	0.81
130	149.13	149.12	0.00	0.06	149.15	0.03	0.03	149.13	0.01	0.29
131	149.55	149.53	-0.02	0.99	149.65	0.10	0.98	149.61	0.06	0.96

Table H.4: Eigenfrequencies, MAC correlation values and relative differences Δ in frequency between A_{220} and the modifications of A_{112}, i.e. $A_{112,B}$, $A_{112,E}$ and $A_{112,T}$.

# mode	A_{220}	$A_{112,B}$			$A_{112,E}$			$A_{112,T}$		
	f [Hz]	f [Hz]	$\Delta_{112,B}$	MAC	f [Hz]	$\Delta_{112,E}$	MAC	f [Hz]	$\Delta_{112,T}$	MAC
132	150.39	150.38	-0.01	1.00	150.41	0.02	0.99	150.38	-0.01	0.91
133	150.99	150.93	-0.06	0.94	151.18	0.19	0.82	151.15	0.16	0.92
134	151.28	151.26	-0.02	0.45	151.32	0.04	0.15	151.30	0.02	0.28
135	151.33	151.32	-0.02	0.93	151.42	0.09	0.81	151.38	0.05	0.88
136	152.59	152.59	-0.01	1.00	152.61	0.02	0.99	152.59	0.00	0.92
137	152.95	152.94	0.00	1.00	152.96	0.01	1.00	152.95	0.00	0.98
138	154.01	153.99	-0.03	1.00	154.04	0.03	0.99	154.04	0.03	0.96
139	154.16	154.14	-0.02	0.97	154.20	0.04	0.95	154.18	0.02	0.74
140	154.84	154.84	0.00	1.00	154.84	0.00	1.00	154.84	0.00	0.98
141	154.94	154.93	-0.02	0.99	155.02	0.07	0.99	154.98	0.04	0.75
142	155.59	155.59	-0.01	1.00	155.61	0.01	1.00	155.57	-0.02	0.51
143	155.96	155.95	0.00	1.00	155.96	0.01	1.00	155.95	-0.01	0.81
144	156.71	156.70	-0.02	1.00	156.74	0.02	1.00	156.52	-0.20	0.07
145	156.98	156.97	0.00	1.00	156.98	0.00	1.00	156.87	-0.11	0.05
146	157.42	157.40	-0.03	1.00	157.49	0.06	1.00	156.98	-0.45	0.57
147	158.22	158.21	-0.01	1.00	158.24	0.02	1.00	157.50	-0.72	0.72
148	158.50	158.49	-0.01	0.64	158.52	0.02	0.61	158.24	-0.26	0.22
149	158.59	158.55	-0.04	0.97	158.69	0.10	0.97	158.52	-0.08	0.02
150	159.58	159.57	-0.01	1.00	159.58	0.00	1.00	158.73	-0.85	0.02
151	160.23	160.23	0.00	1.00	160.23	0.00	1.00	159.59	-0.65	0.00
152	160.65	160.65	0.00	1.00	160.65	0.01	1.00	160.23	-0.41	0.20
153	161.42	161.41	-0.02	1.00	161.48	0.06	0.99	160.65	-0.77	0.05
154	161.79	161.78	0.00	1.00	161.79	0.00	1.00	161.49	-0.30	0.00
155	162.05	162.05	0.00	1.00	162.05	0.00	1.00	161.79	-0.26	0.48
156	162.61	162.60	-0.01	1.00	162.62	0.01	1.00	162.05	-0.55	0.40
157	162.70	162.70	0.00	0.93	162.71	0.01	0.83	162.62	-0.08	0.05
158	163.20	163.19	-0.01	1.00	163.23	0.03	1.00	162.71	-0.50	0.09
159	164.35	164.32	-0.03	0.93	164.36	0.01	0.94	163.23	-1.11	0.57
160	164.50	164.50	-0.01	0.99	164.51	0.01	1.00	164.37	-0.14	0.38
161	165.05	165.01	-0.04	0.83	165.06	0.01	0.99	164.51	-0.54	0.89
162	165.47	165.17	-0.30	0.17	165.50	0.03	0.92	165.06	-0.41	0.58
163	166.01	165.56	-0.45	0.02	166.02	0.01	0.83	165.51	-0.50	0.54
164	166.16	166.02	-0.14	0.02	166.16	0.00	0.94	166.02	-0.14	0.00
165	166.49	166.16	-0.33	0.04	166.59	0.09	0.03	166.16	-0.33	0.00
166	166.63	166.59	-0.04	0.39	167.08	0.45	0.20	166.59	-0.04	0.08
167	167.30	167.14	-0.16	0.74	168.02	0.71	0.01	167.11	-0.19	0.21
168	167.99	167.96	-0.02	0.99	168.13	0.14	0.82	168.03	0.04	0.97
169	168.13	168.12	-0.01	0.77	168.73	0.59	0.11	168.14	0.00	0.50
170	168.72	168.72	0.00	0.97	169.00	0.28	0.16	168.73	0.01	0.83
171	169.00	169.00	0.00	1.00	169.58	0.58	0.00	169.00	0.00	0.99
172	169.54	169.53	-0.01	1.00	169.61	0.08	0.31	169.57	0.04	0.99
173	169.63	169.62	-0.01	0.94	170.28	0.65	0.04	169.62	-0.01	0.71
174	170.29	170.29	0.00	0.99	170.66	0.37	0.13	170.29	0.00	0.95
175	170.69	170.68	0.00	0.99	170.73	0.04	0.27	170.68	-0.01	0.86
176	170.74	170.73	0.00	0.99	171.14	0.41	0.00	170.73	0.00	0.93
177	171.14	171.14	-0.01	1.00	171.65	0.50	0.08	171.15	0.00	0.99
178	171.62	171.61	-0.01	0.93	171.81	0.19	0.04	171.65	0.02	0.92